Università degli Studi di Cagliari

DOTTORATO DI RICERCA

FISICA

Ciclo XXVIII

Magnetoelectric, multiferroic, wide-gap, and polar oxides for advanced applications: first-principles theoretical studies

Settore scientifico disciplinare di afferenza:

FIS/03 Fisica della Materia

Presentata da:	Maria Barbara Maccioni
Coordinatore Dottorato:	Prof. Alessandro De Falco
Tutor:	Prof. Vincenzo Fiorentini

Esame finale anno accademico 2014 – 2015

La presente tesi è stata prodotta durante la frequenza del corso di dottorato in Fisica dell'Università degli Studi di Cagliari, a.a. 2012/2015 - XXVIII ciclo, con il supporto di una borsa di studio finanziata con le risorse del P.O.R. SARDEGNA F.S.E. 2007-2013 - Obiettivo competitività regionale e occupazione, Asse IV Capitale umano, Linea di Attività l.3.1 "Finanziamento di corsi di dottorato finalizzati alla formazione di capitale umano altamente specializzato, in particolare per i settori dell'ICT, delle nanotecnologie e delle biotecnologie, dell'energia e dello sviluppo sostenibile, dell'agroalimentare e dei materiali tradizionali"

University of Cagliari

DEPARTMENT OF PHYSICS
Ph.D. degree in Physics

Magnetoelectric, multiferroic, wide-gap, and polar oxides for advanced applications: first-principles theoretical studies

Ph. D. Thesis

Ph. D. Candidate:
Maria Barbara Maccioni

Tutor:
Prof. Vincenzo Fiorentini

Coordinator:
Prof. Alessandro De Falco

XXVIII Cycle - Academic Year 2014/2015

Contents

INTRODUCTION **1**

1 Density Functional Theory **4**
1.1 Many-Body System 4
1.2 Hartree and Hartree-Fock Theories 7
1.3 Hoehenberg-Kohn Theorem 9
1.4 Kohn-Sham equations 11
1.5 Exchange and correlation energy 13
1.5.1 Local (Spin) Density Approximation 13
1.5.2 Generalized Gradient Approximation 14
1.6 Kohn-Sham equations for crystalline solids 14
1.7 Pseudopotentials 18
1.7.1 Projector-Augmented Waves 19
1.8 Spin-polarized DFT, collinear and non collinear magnetic ordering 20

2 Ferroelectricity **25**
2.1 Polarization as Berry phase 28

I Multiferroicity and magnetoelectricity in a doped topological ferroelectric **33**

3 Ferroelectricity in a layered perovskite **37**

4 Multiferroic material: $La_2Mn_2O_7$ **41**
4.1 Magnetic properties 43

4.1.1 Results and discussions 47
4.2 Spontaneous Polarization 51
4.2.1 Results and discussions 51

5 Magnetoelectric effect **54**
5.1 Lattice-Mediated Magnetoelectric effect 54
5.1.1 Results and discussions 55
5.2 Dzyaloshinskii-Moriya coupling 59
5.2.1 Results and discussions 60

II Properties of $(Ga_{1-x}In_x)_2O_3$ solid solutions **63**

INTRODUCTION **64**

6 Gallium and Indium Oxides **66**
6.1 Gallium Oxide 66
6.2 Indium Oxide 71
6.3 $(Ga_{1-x}In_x)_2O_3$ alloys 73
6.3.1 Low-x $(Ga_{1-x}In_x)_2O_3$ alloys 74
6.3.2 Structure and gap over the whole x range of $(Ga_{1-x}In_x)_2O_3$ alloys 78
6.4 $(Ga_{1-x}In_x)_2O_3$ alloys at $x \sim 0.5$: $InGaO_3$ 83
6.4.1 Structure optimization 83
6.4.2 Revised phase diagram 85
6.5 Conclusion 87

7 Band offset at interfaces **88**
7.1 Ga_2O_3 / $(Ga_{1-x}In_x)_2O_3$ 89
7.2 In_2O_3 / $(Ga_{1-x}In_x)_2O_3$ 91
7.3 Conclusion 91

8 Epsilon-Ga_2O_3 **93**
8.1 Structure optimization 93
8.2 Pyroelectricity and piezoelectricity 95
8.3 Conclusion 97

CONCLUSIONS **98**

A $La_2Mn_2O_7$ cell parameters **101**

B Brillouin Zone **103**

C Cr_2O_3 **109**

D Types of heterostructures **110**

E Piezoelectric tensor **112**

List of Figures

1.1 Approximation of the effective potential with a pseudo-potential. The all-electron potential V=Z/r and orbital ψ_v are altered to the pseudopotential V_{pseudo} and pseudo-orbital ψ_{pseudo} inside the core radius r_c. 19

1.2 Schematic of the distinction between collinear ferromagnetic (left) and anti-ferromagnetic (center) and non-collinear (right) moment configuration. 21

2.1 Typical behaviour of the order parameter η at a phase transition. Above T_c η is vanishing and below T_c η has some finite value. . . 26

2.2 $F(\eta)$ as a function of order parameter, for different values of temperature. The minimum of the free energy below T_c should occur at $\eta \neq 0$ and above T_c at $\eta = 0$. 27

2.3 Calculated polarization as a function of percentage distortion from the high symmetry non-polar structure (0% distortion) to the ground state *R3c* structure for perovskite $BiFeO_3$. 32

2.4 Representation of the relationship between multiferroic and magnetoelectric materials. 34

2.5 Perovskite oxides, of general formula ABO_3 with a pseudocubic structure, where A and B are two different cations, furnish many interesting ferroelectrics. The B-type cation is octahedrally coordinated with oxygen. The left panel shown the relative symmetry breaking displacement of the B-cation with respect to the O atoms which is responsible for the spontaneous polarization. 35

3.1 Sketch of the idealized (i.e. non-distorted) crystal structure of the n=2, 3 and 4 members of the perovskite-related layered homologous series $A_nB_nO_{3n+2}$ projected along the a-axis. Circles represent the A-cations. 38
3.2 Tipical anti-ferrodistortive mode occurring in a layered peroskite oxide on (a) panel. It is shown one layer with $n = 4$ perovskite-like planes. (b) oxygen-octahedra rotations existing in an ideal (non-layered) perovskite structure. Arrows on the site of both sketches represent the electric dipole associated to distortion. 39
3.3 The structure of the $La_2Ti_2O_7$ layered perovskite in the non-distorted phase in x, y, z views. 40
3.4 The structures involved in the $La_2Ti_2O_7$ phase transition, PE phase on the left and FE phase on the right. Ti ions (blue) are surrounded by oxygen octahedra (O red), with La ions (violet) interspersed. . 40

4.1 Structures involved in PE→FE phase transition of $La_2Mn_2O_7$. *Cmcm* is the centrosymmetric and *Cmc2₁* is the distorted structures, both have 44-atom conventional cell. Coordinate axes are labeled referring to crystallographic axes. 42
4.2 Strong antiferromagnetic exchange interaction in cuprates, two Cu^{2+} ions mediated by an oxygen ion O^{2-}. 44
4.3 In the crystal of MnO, each ion of Mn^{2+} has a orbital $3d$ partially occupied, they are separated by the presence of an ion of O^{2-} and form a bond angle 180°, in agreement with the Goodenough-Kanamori rule, the exchange interaction is antiferromagnetic. In fact, the configuration (a) has a greater energy cost compared to the configuration (b) that, consequently, is favored. 45
4.4 Left panel. Strong antiferromagnetic exchange interaction if the half-filled orbitals of two cations overlap with the same empty or filled orbital of the intervening anion. Right panel. Weaker ferromagnetic exchange interaction if the half-filled orbitals of two cations overlap with orthogonal orbitals of the same intervening anion. 45
4.5 Energetically (a) favourite , (b) unfavourite alignment 46
4.6 Typical magnetic structures for the perovskites. 47
4.7 Types of magnetic ordering examined. 48
4.8 Total Energy as a function of the distortion in ferromagnetic, FM, and antiferromagnetic, AFM-C, configurations. 49

4.9 Differences in energy between the ferromagnetic state and the antiferromagnetic AFM-c, as a function of the distortion 49
4.10 Computed distortion dependence of the polarization. 52
4.11 Computed distortion dependence of the polarization (blue) the total energy in the AF configuration (red) in $Cmcm \rightarrow Cmc2_1$ transition 53

5.1 (a) Spin canting due to the spin-orbit interaction. (b) Polarization and magnetization induced by the total distortion mode. 57
5.2 (a) Primitive cell of the Cr_2O_3. The arrows represent the antiferromagnetic spin alignment, while the dotted arrows show the effect of the spin-orbit. (b) Variation of polarization and magnetization induced by IR modes, A_{2u} (dotted line) and E_u (line) as a function of the amplitude of the modes. 58
5.3 Canting of magnetic moments and a resulting net magnetization M≠0 in an otherwise collinear antiferromagnet. The Dzyaloshinskii-Moriya (DM) interaction is an antisymmetric, anisotropic exchange coupling $H_{DM} = \mathbf{D}_{12} \cdot \mathbf{S}_1 \times \mathbf{S}_2$ between two spins S_1 and S_2 separated by a lattice bond r_{12} with no inversion center, i.e. $\mathbf{D}_{12} \sim \lambda \mathbf{a} \times \mathbf{r}_{12}$. The Dzyaloshinskii-Moriya vector $\mathbf{D}$ is proportional to a spin-orbit coupling constant λ, and depends on the position of the oxygen ion between two magnetic transition metal ions. 59
5.4 The cluster model with two transition metal ions M_1, M_2 with the oxigen atom, O, between them. With the noncollinear spin directions $\bar{e}_1$ and $\bar{e}_2$, there arise the spin current $\bar{j}_s \propto \bar{e}_1 \times \bar{e}_2$ between M_1 and M_2. Here the direction of the vector $\bar{j}_s$ (denoted by the short arrow near the middle of the diagram) is that of the spin polarization carried by the spin current. The direction of the electric polarization $\bar{P}$ is given by $\bar{P} \propto \bar{e}_{12} \times \bar{j}_s$ where $\bar{e}_{12}$ is the unit vector connecting M_1 and M_2. 60

6.1 Different views of the monoclinic phase of Ga_2O_3. The structure of β-Ga_2O_3 can be seen as a collection of zigzag double chains of edge-sharing GaO_6 units (violet and green Ga-octahedra) linked by single chains of vertex-sharing GaO_4 (blue Ga-tetrahedra). . . 67
6.2 Band structure and projected density of states of β-Ga_2O_3 68

6.3 Absorption spectra of β-Ga_2O_3 at normal incidence on the (010) surface with polarizations $\mathbf{E}\|\mathbf{c}$ and $\mathbf{E}\|\mathbf{a}$. Absorption spectra of a (-201) wafer orientation. 69
6.4 Tauc plot of the absorption coefficient, showing the polarization dependent onsets. 70
6.5 Gap vs volume as obtained from hybrid and self-interaction corrected functionals, as well as from GW_0 many-body perturbation theory. The line EXP marks the cell volume obtained from experimental lattice parameters. 71
6.6 The bixbyite structure (group T_h) has six-fold coordinated cations occupying 8*b* high-symmetry and 24*d* Wyckoff sites. The 8*b* sites are highlighted by the local oxygen octahedra in the left panel, the 24*d* in the right one. 72
6.7 Band structure ob bixbyite In_2O_3. The **k**-points are: $\Gamma = (0\,0\,0)$; H= $(\frac{1}{2}\ -\frac{1}{2}\ \frac{1}{2})$; N= $(0\,0\,\frac{1}{2})$; $\Gamma = (0\,0\,0)$; P= $(\frac{1}{4}\ \frac{1}{4}\ \frac{1}{4})$; H= $(\frac{1}{2}\ -\frac{1}{2}\ \frac{1}{2})$. 73
6.8 XRD patterns of $(Ga_xIn_{1-x})_2O_3$ films with different indium contents (x) deposited on (0001) sapphire substrates at substrate temperature of 500°C. Peaks marked by triangle belong to monoclinic structure while that marked by circle belong to cubic structure. Peaks not assigned belong to the sapphire substrate. 74
6.9 Different pairings patterns of 6% In-content in β-Ga_2O_3. 75
6.10 Sketch of different configurations of In on the Ga_2O_3 simulation supercell. Occupied octahedra in the β structure double-rows are darkened. 76
6.11 Left: direct gap at zone center as function of In concentration. Right: normalized volume of In-doped Ga_2O_3 as function of concentration. 78
6.12 Mixing free energy as a function of In concentration at 810 K and 2000 K for β-phase vs epitaxial bixbyite (left panel), and β-phase vs free-standing bixbyite (right panel). The phase separation region extends between the vertical dashed and dash-dotted lines. 80
6.13 Left panel: volume vs mole fraction for the free-standing β and bixbyite phases. Right panel: fundamental gap in the same phases and interpolations vs x (quadratic for bixbyite; linear at low x for β). A correction for the gap error has been introduced. The gap show a sizeable bowing in bixbyite at large x. 82

6.14 Supercell of $Ga_{1-x}In_x)_2O_3$ with 50% In-concentration. In this structure In is six-fold coordinated occupying 2a Wyckoff sites while Ga is five-fold coordinated occupying 2c Wyckoff sites. . . . 84
6.15 Revised phase diagram for $(Ga_{1-x}In_x)_2O_3$ for T=800 K. 86

7.1 Macroscopic averages of the electron density (full line) and the corresponding electrostatic potential (broken line) at a GaAs/AlAs heterojunction. 89
7.2 Upper panel: simulation cell for the (100) superlattice (for definiteness I display the epitaxial geometry). Lower panel: the electrostatic potential of the superlattice, showing small but definite bulk regions on either side of the interface. The potential is aligned with the lower side of the cell. 90
7.3 Schematic of the staggered and straddling offset for, respectively, the epitaxial and free-standing superlattice configurations. 91
7.4 Valence (VBO, top) and conduction (CBO, bottom) interface band offsets between In_2O_3 and $(Ga_{1-x}In_x)_2O_3$ in the bixbyite phase, both epitaxially constrained on In_2O_3, or with compliant substrate. The offset between Ga_2O_3 and low x $(Ga_{1-x}In_x)_2O_3$ at x $\simeq$ 0.1 in the β phase for the same conditions are also reported. 92

8.1 Different views of the orthorhombic phase of Ga_2O_3. Ga occupies octahedral (Ga1, Ga2, Ga4) and tetrahedral (Ga3) sites which form zigzag ribbons of edge-sharing octahedra and corner-sharing tetrahedra. 94
8.2 Polarization calculated along a path connecting the centrosymmetric parent phase (0) to non-centrosymmetric ε-Ga_2O_3 (1). 96

B.1 Brillouin Zone of space group *Cmcm* (63) 104
B.2 Brillouin Zone of space group $Cmc2_1$ (36) 104
B.3 Brillouin Zone of space group *C2/m* (12) 105
B.4 The k-vector types of space group *C2/m* (12) 106
B.5 Brillouin Zone of space group $Ia\bar{3}$ (206) 107
B.6 The k-vector types of space group $Ia\bar{3}$ (206) 108

D.1 Various heterostructure band alignments 110

List of Tables

5.1 Total energy and the density of the magnetization for the structure $Cmc2_1$ with the AFM-c configuration. 56
5.2 Parameters of the eq.(5.3) and ME tensor coefficient for the non-zero component α_{zy} in LMO compared with the range of value obtained by Iniguez for Cr_2O_3 for the individual IR modes. 58

6.1 Different polymorphs of Ga_2O_3. The type and the space group of these structures are specified. 66
6.2 Structure parameters of β-Ga_2O_3 in the monoclinic phase, it has Z=4 formula units per crystallographic cell. 67
6.3 Computed structure parameters of In_2O_3 in the $Ia\bar{3}$ phase. . . . 72
6.4 The energy of structure with 6% In-content in different configurations, in β-Ga_2O_3 phase. Every In occupies octahedral site 75
6.5 Calculated structure parameters of $InGaO_3$. The unit cell contains ten atoms, i.e. Z=2 formula units per unit cell. 84

8.1 Structure parameters of ε-Ga_2O_3 in the orthorhombic phase, $Pna2_1$, with Z=8 formula units per crystallographic cell. 94
8.2 Structure parameters of Ga_2O_3 in the orthorhombic phase, $Pnma$. The structure has been predicted by PSEUDO. 96

A.1 Computed equilibrium structure of the paraelectric $Cmcm$ phase of $La_2Mn_2O_7$. 101
A.2 Computed equilibrium structure of the ferroelectric $Cmc2_1$ phase of $La_2Mn_2O_7$. 102

C.1 Cr_2O_3: Technical parameters. 109

INTRODUCTION

This Ph.D. thesis reports a theoretical study of electronic and structural properties of different materials for electronic and optical tecnological applications. Over the past few years, in fact, the renaissance of several physical effects has evolved rapidly, firstly due of their implementation in numerous innovative devices.

Among them, the magnetoelectric (ME) effect, or, more in general, the multiferroicity, was studied the first time at the end of the 1800. Then, the interest in magnetoelectric coupling phenomena declined for several decades until a revival in the 1990s. A coupling between electric and magnetic fields in solid state materials was supposed as early as 1894 by Pierre Curie, but it was only in 1959 that magnetoelectric coupling in a ferroelectric, Cr_2O_3, was predicted by Dzyaloshinskii and observed by Astrov a year later. Nevertheless, the operating margin regarding the investigation about these materials is still huge, as demonstrated by the increasing of the number of publications in the last ten years. Theoretical and experimental approaches are applied to devices for amplitude modulation, polarization and phase control of optical waves, magnetoelectric data storage and switching, optical diodes, spin-wave generation as much as amplification and frequency conversion.

Another example is represented by the gallium oxide, Ga_2O_3. It has been determined since the 1950s, but only during the 2000s it has been widely used for the preparation of gas sensors, optoelectronic devices, luminescent materials and catalysts in diverse gas and liquid phase chemical reactions. Nowadays, bulk $\beta - Ga_2O_3$ is well known as a transparent conducting oxide (TCO) because of its wide bandgap.

This thesis is fitted with this context and, for the sake of clarity, it is basically divided into two different main topics.

The former one, discussed in the I part, is related to the analysis of magnetic properties in a layered perovskite, $La_2Mn_2O_7$, LMO. In this framework, I have explored an unconventional type of multiferroicity obtained via magnetic doping of a wide-gap layered-perovskite ferroelectric belonging to the family $A_nTi_nO_{3n+2}$. Using the n = 4 member $La_2Ti_2O_7$ as home base, I have substituted $3d$ atoms for Ti. This isovalent substitution of Mn for Ti produces multiferroicity with weak ferromagnetic (FM), order due to canting of antiferromagnetic Mn spins, and larger than usual linear magnetoelectric coupling [1].

Operationally, I have optimized the structures involved in the paraelectric (PE) ferroelectric (FE) transition. Then, I have determined that $La_2Mn_2O_7$ is a multiferroic materials since ferroelectric (FE) and magnetic order coexist in the same phase, in fact it is approximately a G-type antiferromagnet and exhibits a spontaneous polarization, comparable to displacive ferroelectrics. Finally, I have demonstrated that $La_2Mn_2O_7$ is also a magnetoelectric materials having a non-zero lattice-mediated magnetoelectric tensor, α. Moreover, magnetic noncollinear spin-orbit calculations reveal that spins point along the c direction but manifests a spin canting in the bc plane generating a weak ferromagnetism interpretable by Dzyaloshinsky-Moriya (DM) interaction.

The latter one is described in the II part and concerns the miscibility between Gallium, Ga_2O_3, and Indium, In_2O_3, oxides, $(Ga_{1-x}In_x)_2O_3$. Due to its large band gap between approximately 3.5 eV and 5 eV, the $(Ga_{1-x}In_x)_2O_3$ alloy system can be promising for use in applications like high-power devices, transparent electronics, and solar-blind ultraviolet (UV) photo-detectors.

Operationally, I have studied the electronic and local structural properties of pure Ga_2O_3 and In_2O_3. Then, I have explored alloyed oxide based on the monoclinic, β, equilibrium structures of Ga_2O_3 in different In concentrations. The structural energetics of In in Ga_2O_3 causes most sites to be essentially inaccessible to In substitution, thus limiting the maximum In content to somewhere between 12 and 25 % in this phase [**?**]. As function of x, the gap, volume and band offsets to the parent compound also exhibit anomalies as function of x [3]. Furthermore, I have explored alloyed oxide based on the bixbyite equilibrium structures of In_2O_3 in all x range [4]. The main result is that the alloy could phase-separate in a large composition range, exhibiting a large and temperature-

independent miscibility gap. On the low-x side, the favoured phase is isostructural with $\beta - Ga_2O_3$, and on the high-x side it is isostructural with bixbyite In_2O_3. In addition, in accord with experimental results, intermediate alloying shows an additional crystallographic phase, in competition with the bulk Ga_2O_3 and In_2O_3 phases. Finally, I have investigated the ε-phase of Ga_2O_3, that results to be the second most stable structure beside β-Ga_2O_3. Moreover, ε-Ga_2O_3 exhibits a large spontaneous polarization and a sizeable diagonal piezoelectric coefficient, comparable with typical polar semiconductors.

Methods and technical issues

This theoretical study is based on ab initio calculation that have been performed within the Density Functional Theory (DFT) using the Generalized Gradient Approximation (GGA) for the exchange and correlation energy and the Projector Augmented Wave approach, PAW method, for describing the electron-ion interaction, as implemented in the Vienna Ab Initio Simulation package, VASP [5].

In every section, however, I will describe the appropriate calculations technical details, whereas the theoretical approaches will be introduced in the first Chapter. Since in both parts a multiferroic material has been described, in Chapter 2 I will briefly explain the mechanisms that cause multiferroicity.

CHAPTER 1

Density Functional Theory

This section gives an overview of the theoretical approaches and approximations used in first principle calculations and, in particular, in my research. I have performed my calculations within the Density Functional Theory (DFT), developed by Hohenberg, Kohn, and, subsequently, Sham in the mid fifties [6,7]. This theory, is widely used for electronic structure calculation of the ground-state properties in numerous systems like atoms, molecules and solids. The DFT approach is based on the works of Thomas and Fermi [8,9] but replaces the computation of the many-body wave-function by using single-particle wave-functions including exchange and correlation terms.

In the following, I will summarize the most important features of the DFT: the Born-Oppenheimer approximation [10], the Kohn-Sham equations and, in the end, some theories for the exchange and correlation energy. Then, I will explain the Bloch theorem to describe the motion of electrons in a crystal. Finally, I will take magnetic effects into account introducing the non-collinear magnetism for spin-polarized systems.

1.1 Many-Body System

The physical properties of a solid or, more generally, of a macroscopic many-body system, result from their atomic-scale properties, explained by quantum mechanics. Mathematically, a physics system is described by the solutions of the Schrödinger equation for the stationary states, therefore time independent, that

is expressed as:

$$\hat{H}|\mathbf{\Psi}\rangle = E|\mathbf{\Psi}\rangle \tag{1.1}$$

where the wave-function $\mathbf{\Psi}$ depends on the position of the electrons, $\mathbf{r}$, and the nuclei, $\mathbf{R}$, $\mathbf{\Psi} = \mathbf{\Psi}(\mathbf{r}, \mathbf{R})$. Considering only Coulomb forces, without relativistic corrections, the Hamiltonian can be expressed as the contribution of the kinetic operator for electrons and nuclei, and additional operators that represent the electron-electron, nucleus-nucleus and electron-nucleus interactions:

$$\hat{H} = \hat{T}_{\text{el}}(\mathbf{r}) + \hat{T}_{\text{nucl}}(\mathbf{R}) + \hat{V}_{\text{el,el}}(\mathbf{r}) + \hat{V}_{\text{nucl,nucl}}(\mathbf{R}) + \hat{V}_{\text{el,nucl}}(\mathbf{r}, \mathbf{R}) \tag{1.2}$$

$$\begin{aligned} \hat{H} = &- \sum_i \frac{\hbar^2}{2m}\nabla_i^2 - \sum_I \frac{\hbar^2}{2M}\nabla_I^2 + \\ &+ \frac{1}{2}\sum_{i,j} \frac{e^2}{|r_i - r_j|} + \frac{1}{2}\sum_{I,J} \frac{Z_I Z_J e^2}{|R_I - R_J|} - \frac{1}{2}\sum_{i,I} \frac{Z_I e^2}{|r_i - R_I|} \end{aligned} \tag{1.3}$$

where the indices *i, j* refer to electrons and the indices *I, J* refer to nuclei. Nevertheless, this equation is impossible to be solved exactly but the problem can be simplified by introducing suitable approximations. In this content, the first approximation was proposed in 1927 by Born and Oppenheimer [10], which treats separately the motion of atomic nuclei and electrons. This approximation allows us to uncouple of the electronic and nuclear motion, and the result are two equations: one for the electronic states, where the nuclei are considered in fixed positions, and the other for the vibrational states of the nuclei, where the total energy of the electrons is added to their potential energy.

In this framework, the electronic Schrödinger equation is solved, considering only the wave-function Ψ_{el} that depends on electron positions, while the nuclei are fixed, "frozen", in a certain configuration, very often the equilibrium one.

$$\Psi(\mathbf{r}, \mathbf{R}) = \Psi_{\text{el}}(\mathbf{r}, \mathbf{R})\Phi_{\text{nucl}}(\mathbf{R}) \tag{1.4}$$

The Hamiltonian of the electron motion is written as follows:

$$\left[- \sum_i \frac{\hbar^2}{2m}\nabla_i^2 + \frac{1}{2}\sum_{i,j} \frac{e^2}{|r_i - r_j|} - \frac{1}{2}\sum_{i,I} \frac{Z_I e^2}{|r_i - R_J|} \right] \Psi_{\text{el}}(\mathbf{r}, \mathbf{R}) = E_{\text{el}}(\mathbf{R})\Psi_{\text{el}}(\mathbf{r}, \mathbf{R}) \tag{1.5}$$

and for each electronic energy eigenstate, the energy eigenstates of nuclear motions are:

$$\left[-\sum_I \frac{\hbar^2}{2M}\nabla_I^2 + \frac{1}{2}\sum_{I,J}\frac{Z_I Z_J e^2}{|R_I - R_I|} + E_{\text{el}}(\mathbf{R})\right]\Phi_{\text{nucl}}(\mathbf{R}) = E\Phi_{\text{nucl}}(\mathbf{R}) \tag{1.6}$$

therefore, the total energy of the many-body system will be:

$$E = E_{\text{el}}(\mathbf{R}) + V_{\text{nucl,nucl}}(\mathbf{R}) \tag{1.7}$$

The many-electron equation is reduced to two separate equations, for the electronic and the nuclear motion, although, the eq.(1.5) is still impossible to resolve. This many-electron equation can be approximate to a one-particle equation for one single electron moving in an average potential generated by all the other electrons. This approximation is called the *mean field approximation* (also known as *self-consistent field theory*). It consist in replacing, in eq.(1.2), the operators, that represent the electron-electron interactions, $V_{\text{el,el}}(\mathbf{r}) = \sum_i \sum_{j;j\neq i} \frac{e^2}{|r_i - r_j|}$, by a effective potential $V^{\text{eff}}(\mathbf{r})$ given by the average:

$$V^{\text{eff}} = \left\langle \sum_{\substack{j \\ j\neq i}} \frac{e^2}{|r_i - r_j|} \right\rangle \tag{1.8}$$

$V^{\text{eff}}(\mathbf{r})$ is chosen in such a way that the electronic Hamiltonian is the sum of single particle Hamiltonians and the electronic wave-function $\Psi_{\text{el}}(\mathbf{r})$, in the (1.57), can be expressed as the product of wave-functions of single particle:

$$\Psi_{\text{el}}(\mathbf{r}) = \psi_1(\mathbf{r_1})\psi_2(\mathbf{r_2})...\psi_n(\mathbf{r_n}) \tag{1.9}$$

the Schrödinger equation (1.5) is reduced to a system of separate single-particle equations:

$$\left[-\frac{\hbar^2}{2m}\nabla_i^2 + V^{\text{eff}}(\mathbf{r}) - \sum_I \frac{Z_I e^2}{|\mathbf{r} - \mathbf{R_I}|}\right]\psi_i(\mathbf{r}) = \varepsilon_i\psi_i(\mathbf{r}) \tag{1.10}$$

with $E_{\text{el}}(\mathbf{R}) = \sum \varepsilon_i$, the i run from 1 to n. In order to determine the form of the effective potential, it is possible to use empirical methods, based on functions or parameters obtained experimentally, or methods from first principles, based on theoretical self-consistent developments. In particular, I will describe the Hartree, Hartree-Fock and Density Functional theories.

1.2 Hartree and Hartree-Fock Theories

In the Hartree method, for the electron i-th located at $\mathbf{r_i}$, the effective potential, eq.(1.8), generated by all the other electrons, can be derived applying the variational principle. The many-electron wave-function can be considered as the product of the one-electron wave-functions (1.9) to find the expectation value of $\hat{H}$

$$E\left[\Psi\right] = \frac{\langle\Psi|\hat{H}|\Psi\rangle}{\langle\Psi|\Psi\rangle} \tag{1.11}$$

obtaining

$$\begin{aligned} E = \langle\Psi|\hat{H}|\Psi\rangle = & \sum_i \int d\mathbf{r}\psi_i^*\left(\mathbf{r}\right)\left(-\frac{\hbar^2}{2m}\nabla_i^2 - \sum_I \frac{Z_I e^2}{|\mathbf{r}-\mathbf{R_I}|}\right)\psi_i\left(\mathbf{r}\right) + \\ & + \frac{e^2}{2}\sum_{\substack{i,j \\ j\neq i}} \int d\mathbf{r}d\mathbf{r}'\psi_i^*\left(\mathbf{r}\right)\psi_j^*\left(\mathbf{r}'\right)\frac{1}{|\mathbf{r}-\mathbf{r}'|}\psi_i\left(\mathbf{r}\right)\psi_j\left(\mathbf{r}'\right) \end{aligned} \tag{1.12}$$

Introducing, now, a Lagrange multiplier, λ_i, to take the normalization of the one-electron wave-functions into account, it is possible to minimize the previous equation, so that

$$\delta\left(\langle\Psi|\hat{H}|\Psi\rangle - \sum_i \lambda_i\langle\psi_i|\psi_i\rangle\right) = 0 \tag{1.13}$$

where $i = 1, ..., n$ giving the **Hartree equations**:

$$\left(-\frac{\hbar^2}{2m}\nabla_i^2 - \sum_I \frac{Z_I e^2}{|\mathbf{r}-\mathbf{R_I}|} + \frac{e^2}{2}\sum_{\substack{j \\ j\neq i}} \int d\mathbf{r}'\psi_j^*(\mathbf{r}')\frac{1}{|\mathbf{r}-\mathbf{r}'|}\psi_j(\mathbf{r}')\right)\psi_i\left(\mathbf{r}\right) = \lambda_i\psi_i\left(\mathbf{r}\right) \tag{1.14}$$

The third term, is the *Hartree potential*

$$\frac{e^2}{2}\sum_{\substack{j \\ j\neq i}} \int d\mathbf{r}'\psi_j^*(\mathbf{r}')\frac{1}{|\mathbf{r}-\mathbf{r}'|}\psi_j(\mathbf{r}') \tag{1.15}$$

that depends on the (electronic) charge density $n_i(\mathbf{r_i}) = \sum \psi_i^*(\mathbf{r})\psi_i^*(\mathbf{r})$ and on the eigenfunctions, which are solutions of the same equation. These equations are calculated using an *iterative method*: once the charge density are calculated, it can be calculate the Hartree potential generated by this density and, then, resolve the Schrödinger equation getting new eigenfunctions. The cycle is repeated a number of times up to the convergence that ensicure the difference between the

initial and final value of the eigenvalues will be lower than a fixed one. The Lagrange multiplier, λ_i, coincides with the energy eigenvalue of a single electron ε_i.

However, the wave-function considered in the Hartree theory is not antisymmetric for the exchange of two electrons, and, being electrons fermions, the many-particle wave-function needs to be antisymmetric by exchange of couple of electrons. This constraint can be added by hand, resorting to the Slater determinantal form:

$$\Psi(\mathbf{r_1},...,\mathbf{r_n}) = \frac{1}{\sqrt{n!}} \begin{vmatrix} \psi_1(\mathbf{r_1}) & \psi_2(\mathbf{r_1}) & ... & \psi_n(\mathbf{r_1}) \\ . & . & . & . \\ . & . & . & . \\ \psi_1(\mathbf{r_n}) & \psi_2(\mathbf{r_n}) & ... & \psi_n(\mathbf{r_n}) \end{vmatrix} \tag{1.16}$$

In addition, it needs take the spin states, so that the electron wave-function will be given by the product of the spatial and spin contributions:

$$\psi(\zeta) = \phi(\mathbf{r})\chi(\sigma) \tag{1.17}$$

$$\Psi(\zeta_\mathbf{1},...,\zeta_\mathbf{n}) = \Phi(\mathbf{r_1},...,\mathbf{r_n})\Gamma(\sigma_\mathbf{1},...,\sigma_\mathbf{n}) \tag{1.18}$$

The follow equation, called **Hartree-Fock equation**, is obtained by applying the variational principle:

$$\begin{aligned} &\left(-\frac{\hbar^2}{2m}\nabla_i^2 - \sum_I \frac{Z_I e^2}{|\mathbf{r}-\mathbf{R_I}|} + \frac{e^2}{2}\sum_{\substack{j \\ j\neq i}} \int d\mathbf{r}' \psi_j^*(\mathbf{r}') \frac{1}{|\mathbf{r}-\mathbf{r}'|} \psi_j(\mathbf{r}') \right) \psi_i(\mathbf{r}) \\ &- \left(\frac{e^2}{2}\sum_{\substack{j \\ j\neq i}} \int d\mathbf{r}' \psi_j^*(\mathbf{r}') \frac{1}{|\mathbf{r}-\mathbf{r}'|} \psi_i(\mathbf{r}') \right) \psi_j(\mathbf{r})\, \delta_{\sigma_i\sigma_j} = \varepsilon_i \psi_i(\mathbf{r}) \end{aligned} \tag{1.19}$$

where the first term includes the electronic kinetic energy, electron-nucleus and the Hartree potential, while the second one is the **exchange energy**. It can be seen that the Hartree potential is a local potential, since it depends on the mutual electron position. To be more precise, it is the Coulomb interaction acting on the i-th electron due to the all the others. Moreover, the Hartree-Fock potential is non-local since depends on an average contribution. Furthermore, the Hartree-Fock potential takes into account the correlation of the spin, that is different from zero only for interaction between electrons with the same spin, and is null, consequently, for all pairs of opposite spin contributions.

1.3 Hoehenberg-Kohn Theorem

The Hartree-Fock approach, assuming independent electrons in an effective potential, is an approximation to the true many-body problem. Due to the huge number of electron-electron interactions in a real system, this method is not able to give a reasonable result. Realistic calculations, however, can be performed with the *Density Functional Theory*, (DFT). This method, proposed by Kohn in the early 60s, has been widely used in the field of condensed matter physics. It is mainly based on the **Hoehenberg-Kohn Theorem**, which supposes all the physical properties of a system could only be determined by the knowledge of the charge density of the ground state [6]. Considering now a system of N electrons moving under the influence of an external potential, $V(\mathbf{r_i})$ and the mutual Coulomb repulsion, $W(\mathbf{r_i}, \mathbf{r_j})$, the Hamiltonian can be written as:

$$\hat{H} = \hat{T} + \hat{V}_{\text{ext}} + \hat{W} = \sum_i \left(-\frac{\hbar^2}{2m} \nabla^2_{\mathbf{r_i}} + V(\mathbf{r_i}) \right) + \frac{e^2}{2} \sum_{\substack{i,j \\ j \neq i}} W(\mathbf{r_i}, \mathbf{r_j}) \tag{1.20}$$

The charge density in the ground state can be expressed as:

$$n(\mathbf{r}) = \sum_i |\psi_i(\mathbf{r})|^2 \tag{1.21}$$

Theorem 1 *The external potential V_{ext}, and hence the total energy, is uniquely determined by the density of the ground state of a system of interacting charges, except for an additive constant.*

Theorem 2 *The ground state energy can be obtained variationally: the charge density that minimises the total energy is the exact ground state density. Since the charge density of the ground state uniquely determines the potential V_{ext}, and this potential uniquely determines the wave-function of the ground state, $\mathbf{\Psi}$, then the full many- body ground state is a unique functional of $n(\mathbf{r})$.*

Consequently, for every multi-body wave-function $\mathbf{\Psi}$, representing the electronic ground state, there is a correspondence with the charge density of the ground state:

$$n(\mathbf{r}) = \langle \Psi | \sum_i \delta(\mathbf{r} - \mathbf{r_i}) | \Psi \rangle \tag{1.22}$$

And, in addition, for each external potential, V_{ext}, exists a bijective correspondence with the wave-function of the ground state, $\mathbf{\Psi}$

$$V_{\text{ext}} \Longleftrightarrow \Psi \Longleftrightarrow n(\mathbf{r}) \tag{1.23}$$

Subsequently, from the Hohenberg-Kohn theorem, the wave-function of the ground state and the external potential are functionals of the charge density of the ground state

$$n(\mathbf{r}) \Rightarrow |\Psi\left[n\right]\rangle \Rightarrow V_{\text{ext}}\left[n\right] \tag{1.24}$$

The energy of the ground state related to an external potential V_0 (external potential of a system with a charge density of ground state $n_0(\mathbf{r})$ and energy E_{V_0}) can be written as functional of of the charge density of the ground state:

$$E_{V_0}\left[\Psi_0\right] \Rightarrow E_{V_0}\left[n_0\right] \tag{1.25}$$

$$E_{V_0}\left[n\right] \equiv \langle\Psi_0\left[n\right]|\hat{T} + \hat{V}_{\text{ext}} + \hat{W}|\Psi_0\left[n\right]\rangle. \tag{1.26}$$

For the Rayleigh-Ritz principle, the exat ground state must be determined by minimizing this energy functional: $E_0 < E_{V_0}\left[n\right]$ per $n \neq n_0$, then

$$E_0 = E_{V_0}\left[n_0\right] = \min_{n\in\mathcal{N}} E_{V_0}\left[n\right] \tag{1.27}$$

where $\mathcal{N}$ is the set of all the charge densities.
The eq (1.26) can be rewritten as:

$$E\left[n\right] = F_{HK}\left[n\right] + \int V_{\text{ext}}(\mathbf{r})n(\mathbf{r})d\mathbf{r} \tag{1.28}$$

which $F_{HK}\left[n\right] = \langle\Psi_0\left[n\right]|\hat{T} + \hat{W}|\Psi_0\left[n\right]\rangle$. Since such a functional is not dependent on any external potential, it is the same for all the systems with N interacting electrons.

By applying the variational principle that preserve the number of electrons,

$$\frac{\delta}{\delta n(\mathbf{r})} = \left(E_0\left[n\right] - \mu\int d(\mathbf{r})n(\mathbf{r})\right) = 0 \tag{1.29}$$

the Euler Lagrange equation is obtained as:

$$\frac{\delta E_0\left[n\right]}{\delta n(\mathbf{r})} = \frac{\delta F_{HK}\left[n\right]}{\delta n(\mathbf{r})} + V_{\text{ext}}(\mathbf{r}) = \lambda \tag{1.30}$$

where λ is the Lagrange multiplier with respect to the constraint of the conservation of the number of electrons, which coincides with energy eigenvalue.

The determination of the functional $F_{HK}[n]$ is, however, still difficult to be solved because it takes into account all the interactions between electrons. Nevertheless, this problem is simplified in the formalism of Kohn- Sham [7], where a system of non-interacting electrons is considered. In such as a system, the ground state density is obtained, in practice, by solving the N one-electron Schrödinger equations. This method is still exact since it yields the same ground state density as the real system, but greatly facilitates the calculation.

1.4 Kohn-Sham equations

Kohn and Sham considered a system of non-interacting electrons subjected to a generic potential V_s, the resulting Hamiltonian can be express as:

$$\hat{H} = \hat{T} + \hat{V}_s \tag{1.31}$$

According to the Hohenberg-Kohn theorem, in the non-interacting electrons system, a unique functional energy will exist that is given by:

$$E_s[n] = T_s[n] + \int d(\mathbf{r}) V_s(\mathbf{r}) n(\mathbf{r}) \tag{1.32}$$

where $T_s[n]$ is the kinetic energy functional, and n is the charge density. This equation differs from eq (1.28), by considering $T_s[n]$ instead of $F_{HK}[n]$. The exact density of the ground state of a non-interacting electrons system is produced by applying the variational principle, $\delta E_s[n] = 0$,

$$n_s(\mathbf{r}) = \sum_i |\phi_i(\mathbf{r})|^2 \tag{1.33}$$

where the $\phi_i(\mathbf{r})$ are the eigenfunctions satisfying the Scrödinger equation

$$\left(\frac{\hbar^2}{2m} \nabla^2 + V_s(\mathbf{r}) \right) \phi_i(\mathbf{r}) = \varepsilon_i \phi_i(\mathbf{r}) \tag{1.34}$$

according to the Hohenberg-Kohn theorem. These eigenfunctions are uniquely determined by the potential V_s. Assuming the density of the ground state of the non-interacting electrons system equal to the density of the interacting electrons

system, $n_s(\mathbf{r}) = n(\mathbf{r})$, the expression of the energy functional can be written as:

$$\begin{aligned} E[n] &= T_s[n] + \left\{ T[n] - T_s[n] + W[n] - \frac{e^2}{2} \iint \frac{n(\mathbf{r})n(\mathbf{r}')}{|\mathbf{r}-\mathbf{r}'|} d(\mathbf{r}) d\mathbf{r}' \right\} \\ &+ \frac{e^2}{2} \iint \frac{n(\mathbf{r})n(\mathbf{r}')}{|\mathbf{r}-\mathbf{r}'|} d(\mathbf{r}) d\mathbf{r}' + \int n(\mathbf{r}) V_{\text{ext}}(\mathbf{r}) d(\mathbf{r}) \\ &\equiv T_s + \frac{e^2}{2} \iint \frac{n(\mathbf{r})n(\mathbf{r}')}{|\mathbf{r}-\mathbf{r}'|} d(\mathbf{r}) d\mathbf{r}' + \int n(\mathbf{r}) V_{\text{ext}}(\mathbf{r}) d(\mathbf{r}) + E_{xc}[n] \end{aligned} \tag{1.35}$$

The functional $E_{xc}[n]$ can be defined as:

$$E_{xc}[n] \equiv F_{HK}[n] - \frac{e^2}{2} \iint \frac{n(\mathbf{r})n(\mathbf{r}')}{|\mathbf{r}-\mathbf{r}'|} d(\mathbf{r}) d\mathbf{r}' - T_s[n] \tag{1.36}$$

This functional, called **exchange and correlation energy**, contains the electron-electron interaction contribution (not the Coulomb interaction) and the difference between the kinetic energy of the interacting electrons system and the kinetic energy of non-interacting electrons system corresponding to the same charge density.

Applying the variational principle to the energy functional of the interacting electrons system it can be written:

$$\frac{\delta E[n]}{\delta n(\mathbf{r})} = \frac{\delta T_s[n]}{\delta n(\mathbf{r})} + e^2 \int \frac{n(\mathbf{r}')}{|\mathbf{r}-\mathbf{r}'|} d(\mathbf{r}') + V_{\text{ext}}(\mathbf{r}) + v_{xc}[n] = 0 \tag{1.37}$$

where $v_{xc}[n]$ is the **exchange and correlation potential** defined as:

$$v_{xc}[n] \equiv \frac{\delta E_{xc}[n]}{\delta n(\mathbf{r})}. \tag{1.38}$$

As previously done in the case of the non-interacting electrons system:

$$\frac{\delta T_s[n]}{\delta n(\mathbf{r})} + V_s(\mathbf{r}) = 0, \tag{1.39}$$

where the potential $V_s(\mathbf{r})$ will be defined as:

$$V_s(\mathbf{r}) = V_{\text{ext}}(\mathbf{r}) + e^2 \int \frac{n(\mathbf{r}')}{|\mathbf{r}-\mathbf{r}'|} d\mathbf{r}' + v_{xc}[n](\mathbf{r}) \tag{1.40}$$

Although exact in principle, Kohn-Sham theory is approximate in practice because of the unknown exchange-correlation functional. This functional is not possible to be determined exactly, but approximations are required.

1.5 Exchange and correlation energy

Two simple physical ways to approximate the exchange-correlation energy are the Local (Spin) Density Approximation, L(S)DA, and Generalized Gradient Approximation, GGA.

1.5.1 Local (Spin) Density Approximation

In the local density approximation, the exchange and correlation energy of an electronic system, is a purely local functional. It is assumed that the energy of the exchange-correlation $\varepsilon_{xc}(\mathbf{r})$ for an electron in the position $\mathbf{r}$ in an inhomogeneous electron gas, is equal to the energy of the exchange-correlation, E_{xc}, for a uniform gas of electron density $n(\mathbf{r})$ at the position $\mathbf{r}$,

$$E_{xc}\left[n(\mathbf{r})\right] = \int \varepsilon_{xc}(\mathbf{r}) n(\mathbf{r}) d(\mathbf{r}) \tag{1.41}$$

then, the exchange and correlation potential is:

$$V_{xc}(\mathbf{r}) = \frac{\delta E_{xc}\left[n(\mathbf{r})\right]}{\delta n(\mathbf{r})} = \frac{\partial\left[n(\mathbf{r})\varepsilon_{xc}(\mathbf{r})\right]}{\partial n(\mathbf{r})} \tag{1.42}$$

with

$$\varepsilon_{xc}(\mathbf{r}) = \varepsilon_{xc}^{\text{unif}}\left[n(\mathbf{r})\right] \tag{1.43}$$

The exchange and correlation energy, $\varepsilon_{xc}^{\text{unif}}\left[n(\mathbf{r})\right]$, consists of separately contributions of exchange and correlation. The first one is determined analytically in the limits of low and high charge density, precisely $r_s \to \infty, \quad r_s \to 0$, with $r_s = \left(\frac{4\pi n}{3}\right)^{-1/3} u.a.$ Wigner-Seitz radius [1]. In fact,

$$\varepsilon_x\left[n(\mathbf{r})\right] = -\frac{3}{4}\left(\frac{3}{\pi}\right)^{1/3} = -\frac{3}{4}\left(\frac{9}{4\pi^2}\right)^{1/3}\frac{1}{r_s} = -\frac{0.458}{r_s} u.a. \tag{1.44}$$

Analytic expressions for the correlation energy are proposed by Ceperley and Alder [11] and Perdew and Wang [12] using quantum Monte-Carlo simulations of the homogeneous electron gas.

Including the spins, the exchange and correlation energy can be rewritten as:

$$\varepsilon_{xc}\left[n_+, n_-\right] = \varepsilon_x\left[n_+, n_-\right] + \varepsilon_c\left[n_+, n_-\right] \tag{1.45}$$

[1] Radius of the sphere that can be associated to each electron in atomic units, so that the volume of all spheres 'add up' to the total volume of the system. In the other word, the Wigner-Seitz radius, is the radius of a sphere whose volume is equal to the mean volume per atom in a solid

and the exchange contribution can be expressed as:

$$\varepsilon_x [n_+, n_-] = \frac{1}{2}\varepsilon_x [2n_+] + \frac{1}{2}[2n_-] \tag{1.46}$$

Considering the same method in LDA, can be set $C_x = \frac{3}{4}\left(\frac{3}{\pi}\right)^{1/3}$

$$\varepsilon_x [n_+, n_-] = 2^{1/3} C_x \int \left[n_+^{4/3}(\mathbf{r}) + n_-^{4/3}(\mathbf{r})\right] d(\mathbf{r}) \tag{1.47}$$

1.5.2 Generalized Gradient Approximation

In the Generalized Gradient Approximation (GGA), the exchange-correlation energy is defined as in the LDA plus the second-order gradient of the charge density, $\nabla n(\mathbf{r})$. Expanding in series with respect to the exchange-correlation energy for an electron gas with uniform density:

$$\begin{aligned} \varepsilon_{xc}[n] = \int [&g_{00}(n) + g_{22}(n)(\nabla n)^2 + g_{42}(n)(\nabla^2 n)^2 \\ &+ g_{43}(n)(\nabla^2 n)(\nabla n)^2 + g_{44}(n)(\nabla n)^4 + ...] d\mathbf{r} \end{aligned} \tag{1.48}$$

and including spin contributions, the exchange and correlation contribution is:

$$\varepsilon_{xc}^{\mathrm{GGA}} = \int f(n_+, n_-, \nabla n_+, \nabla n_-) d\mathbf{r}. \tag{1.49}$$

In comparison with LSD, GGA tends to improve the total energies. GGA expands and soften bonds, an effect that sometimes corrects and sometimes overcorrects the LSD prediction. Typically, GGA favors density inhomogeneity more than LSD does. GGA produces the corrected fundamental state for magnetic transition metals, better than LSDA. While in the case of spin unpolarized, using LSDA more satisfactory results are obtained than the GGA [13].

1.6 Kohn-Sham equations for crystalline solids

An ideal crystal is constituted by a repetition of ordered spatial structural units, which can be described through a single periodic lattice. Each lattice point is associated with a structural unit, which can contain only one atom or group of atoms, called base. The grid is defined by a set of data points with the relation:

$$\mathbf{R} = n_1\mathbf{a}_1 + n_2\mathbf{a}_2 + n_3\mathbf{a}_3 \tag{1.50}$$

where the $\mathbf{a}_i$ are the fundamental translation vectors that define a primitive cell which contains a single lattice point. Generally, these vectors are given with the crystallographic axes, and n are integers. There are 14 distinct translational lattices, called *Bravais lattices*, grouped into seven crystal systems according to the seven types of conventional unit cell. The three base vectors define, in addition, the periodicity of the lattice, and for any vector $\mathbf{R}$ lattice, the external potential $V_{\text{ext}}(\mathbf{r})$ has the same frequency as the Bravais lattice associated to the solid:

$$V_{\text{ext}}(\mathbf{r}+\mathbf{R}) = V_{\text{ext}}(\mathbf{r}) \tag{1.51}$$

Moreover, the density in a point (r) and the correspondent energy are invariant under translations of vectors $\mathbf{R}$ belonging to the lattice, or rather both the potential of Kohn-Sham and the total Hamiltonian have the periodicity of the lattice. This is a consequence of the Bloch theorem:

Theorem 3 (Bloch) *Any solution of the Schrödinger equation with a periodic potential can be represented as a plane wave modulated by a function having the same periodicity of the lattice.*

In accord with Bloch's theorem, the eigenstates of a one-particle Hamiltonian can be written as the product of a plane wave and a lattice-periodic function

$$\psi_{n,\mathbf{k}}(\mathbf{r}) = e^{i\mathbf{k}\cdot\mathbf{r}} u_{n,\mathbf{k}}(\mathbf{r}) \tag{1.52}$$

where $u_{n,\mathbf{k}}(\mathbf{r})$ is the lattice-periodic function

$$u_{n,\mathbf{k}}(\mathbf{r}+\mathbf{R}) = u_{n,\mathbf{k}}(\mathbf{r}), \tag{1.53}$$

and the indices $\mathbf{k}$ and n are the wave-vector labelling the wave-function and the band index which labels the different solutions for a given k, respectively. If the wavefuntions are shifted by a lattice vector, they became:

$$\psi_{n,\mathbf{k}}(\mathbf{r}+\mathbf{R}) = e^{i\mathbf{k}\cdot\mathbf{R}} \psi_{n,\mathbf{k}}(\mathbf{r}). \tag{1.54}$$

Thanks to their periodicity, the functions $u_{n,\mathbf{k}}(\mathbf{r})$, can be developed in series of plane waves, whose wave vectors are the vectors of the reciprocal lattice of the crystal:

$$u_{\mathbf{k}}(\mathbf{r}) = \sum_{\mathbf{G}} e^{i\mathbf{G}\cdot\mathbf{r}} c_{\mathbf{G}} \tag{1.55}$$

where $\mathbf{G}$ is the vector of the reciprocal lattice, and satisfies the relation:

$$\mathbf{R} \cdot \mathbf{G} = 2\pi m \qquad m \in \mathcal{N}, \tag{1.56}$$

Therefore, the wave-function can be expressed as:

$$\psi_{n,\mathbf{k}}(\mathbf{r}) = \sum_{\mathbf{G}} e^{i(\mathbf{k}+\mathbf{G})\cdot\mathbf{r}} c_{n,\mathbf{k}+\mathbf{G}} \tag{1.57}$$

The allowed electronic states, and thus the set of discrete points k, are determined by the periodic boundary conditions of Born-Von Karman[2]. The k-wavevector, labeling the wave-function, can be chosen in the first Brillouin zone due to the translational symmetry. Computationally, a complete expansion in terms of infinitely many plane waves is not possible, for this reason the plane wave expansion must be truncated. A cutoff energy value, $E_{\mathrm{cut-off}}$ determines the number of plane waves in the expansion, satisfying:

$$\frac{\hbar^2}{2m}|\mathbf{k}+\mathbf{G}|^2 \leq E_{\mathrm{cut-off}}. \tag{1.58}$$

Basis set size depends only on the computational cell size and the cutoff energy value. For a periodic system, integrals in real space over the (infinitely extended) system are replaced by integrals over the (finite) first Brillouin Zone in reciprocal space, according to the Bloch's theorem. For example, the charge density are defined as:

$$n(\mathbf{r}) = \sum_i \int_{BZ} d\mathbf{k} |\psi_{i\mathbf{k}(\mathbf{r})|^2} \tag{1.59}$$

In this equation, such integrals are performed by summing the function values of the integrand at a finite number of points in the Brillouin Zone, called the *k-point mesh*. Choosing a sufficiently dense mesh of integration points is crucial for the convergence of the results, and is therefore one of the major objectives when performing convergence tests.

K-points sampling and method for smearing

The widely used sets of special points, are the *Monkhorst and Pack* [14] and *the linear tetrahedron method* ones. The first k-point mesh consist of an equispaced grid of k-points, while, in the second one, reciprocal space is divided into tetrahedra. In other word, partial occupancies are used to decrease the number

[2] $\psi(\mathbf{r} + N_i\mathbf{a_i}) = \psi(\mathbf{r})$

of k-points necessary to calculate an accurate band-structure energy. That error, introduced in this approximation, is greater in the metals. In metallic systems Brillouin-zone integrals over functions that are discontinuous at the Fermi-level require a greater number of points k to accurately calculate the Fermi surface. In order to solve this problem the step function[3] is replaced by a smooter function, called *smearing*, σ. Several methods have been proposed to solve the problem of a much faster convergence speed without destroying the accuracy of the sum, for example:

Fermi-Dirac smearing, in this case the step function is simply replaced by the Fermi-Dirac functions [15]

$$f\left(\frac{\varepsilon_k v - E_F}{\sigma}\right) = \frac{1}{exp\left(\frac{\varepsilon_k v - E_F}{\sigma}\right) + 1} \tag{1.60}$$

Gaussian smearing, in the Gaussian smearing the step function is replaced by function [16]:

$$f\left(\frac{\varepsilon_k v - E_F}{\sigma}\right) = \frac{1}{2}\left(1 - erf\left[\frac{\varepsilon_k v - E_F}{\sigma}\right]\right) \tag{1.61}$$

This method serves as an mathematical tool to obtain faster convergence with respect to the number of k-points.

The linear tetrahedron method, in this case reciprocal space is divided into tetrahedra with matrix elements and band energies linearized in k. The linear approximation allows the integration to be performed analytically, taking into account the often complicated shape of the Fermi surface [17].

Methfessel-Paxton method, which approximates the step-function by starting with the delta-function using expansion in a set of orthogonal Hermite polynomials [18].

[3]The function of occupancy of states, at $T = 0$ is the step function, equal to one if the eigenvalue $\varepsilon_k v < E_F$ and zero for $\varepsilon_k v > E_F$, where E_F is the Fermi energy.

1.7 Pseudopotentials

The Kohn-Sham equations, obtained by developing single electron orbitals in a series of plane waves, are described by the secular equation:

$$\sum_{G'}\left[\frac{\hbar^2}{2m}|\mathbf{k}+\mathbf{G}|^2+V_H(\mathbf{G}-\mathbf{G}')+V_{sc}(\mathbf{G}-\mathbf{G}')+V_{\text{ext}}(\mathbf{G},\mathbf{G}')\right]c_{n,\mathbf{k}+\mathbf{G}'}= \\ =\varepsilon_{n,\mathbf{k}}c_{n,\mathbf{k}+\mathbf{G}} \tag{1.62}$$

The expansion of the wave-functions in plane waves uses the same resolution in all regions of space, so, if we want to accurately describe all the electrons of the system, including those belonging to the inner shells (core electrons), we would need a very large number of plane waves. This problem can be overcame by using the *method of the pseudo-potential.*

Pseudopotentials were suggested by Phillips and Kleinman [19] and enlarged by Heine, Cohen [20]. This method allows us to achieve a resonable convergence considering appropriate basis set. The pseudo-potentials are constructed to replace the atomic all-electron potential with a weaker potential. The core states are neglected and the valence electrons are described by pseudowave-function. The pseudopotential formalism grew out of the Orthogonalized Plane Wave (OPW) method [21], in which valence wave-functions were expanded in a set of plane waves (PW) which are orthogonalized to all of the core wave-functions ψ_c. The valence states are smoothed in the core region by subtracting out the core orthogonality wiggles, leading to pseudostates ψ_{pseudo}.

Figure 1.1 shows the ionic potential, solid line, the pseudo-potential, dotted line, and the corresponding wave-functions. With r_c is indicated the radius of the core. The pseudopotential approximation replaces the strong ionic potential $V = Z/r$ in the core region, by a weaker pseudopotential V_{pseudo}. The corresponding set of pseudo-wave-functions ψ_{pseudo} and the all-electron wave-functions ψ^{AE} are identical outside a chosen cutoff radius r_c and so exhibit the same scattering properties, but ψ_{pseudo} does not possess the nodal structure that cause the oscillations inside r_c, which means they can now be described with a reasonable number of plane-waves. The conditions of a good pseudopotential are that it reproduces the logarithmic derivative of the wave-function (and thus the phase-shifts) correctly for the isolated atom, and also that the variation of this quantity with respect to energy is the same to first order for pseudopotential and full po-

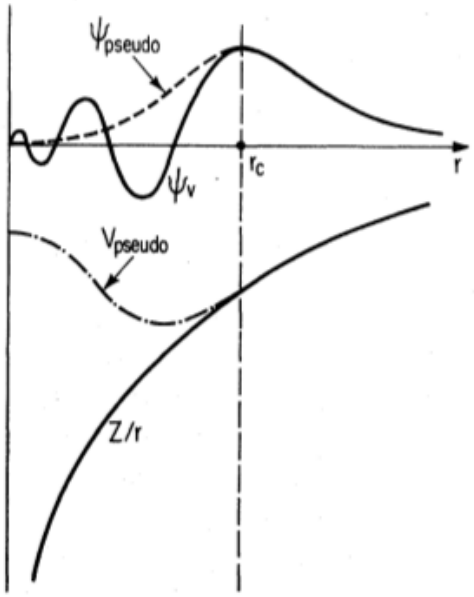

Figure 1.1: Approximation of the effective potential with a pseudo-potential. The all-electron potential V=Z/r and orbital ψ_v are altered to the pseudopotential V_{pseudo} and pseudo-orbital ψ_{pseudo} inside the core radius r_c. Ref. [22].

tential, *norm-conservation* criterion. In the region outside the core, in fact, the pseudo-wave-functions and effective functions (AE, *all*-electrons), must have the same dependence on the spatial coordinate, and the same norm, so that they can generate the same charge density, guaranteeing the principle of conservation of charge [22].

1.7.1 Projector-Augmented Waves

In the projector-augmented waves (PAW) method [23], the all-electron valence wave-functions, (AE), are built starting from the pseudo-wave-functions, (PS), via a linear transformation as:

$$|\psi_n^{\mathrm{AE}}\rangle = |\psi_n^{\mathrm{PS}}\rangle + \sum \left(|\phi_n^{\mathrm{AE}}\rangle - |\phi_n^{\mathrm{PS}}\rangle\right) \langle p_i^{\mathrm{PS}}|\psi_n^{\mathrm{PS}}\rangle \tag{1.63}$$

Because of that, this method consists in separating the total wave-function in a wave-function within the partial spherical region of the core, centered on the core, while the outside in a function expressed as a series of plane waves or other functions of an appropriate base. Obviously, on the surface of the sphere the two functions should have the same value and the same first derivative.

In the previous equation (1.63), the funtions ϕ_n^{AE} are the solutions of the Schrödinger equation for an atom not spin-polarized with energy ε_i in the regime

of valence; the partial wave-functions ϕ_n^{PS} are identical to the actual wave-functions outside the core region; the p_i^{PS}, are functions projected that satisfy the relation:

$$\langle p_i^{\mathrm{PS}}|\phi_n^{\mathrm{PS}}\rangle = \delta_{ij}\langle r|p_i^{\mathrm{PS}}\rangle = 0, \qquad r > r_c \tag{1.64}$$

The charge density corresponding to an effective eigenstate, ψ_n^{AE}, given by $n(\mathbf{r}) = \langle\psi_n^{\mathrm{AE}}|\mathbf{r}\rangle\langle\mathbf{r}|\psi_n^{\mathrm{AE}}\rangle$ is composed by:

$$n(\mathbf{r}) = n^{\mathrm{PS}}(\mathbf{r}) - n^{\mathrm{PS},1}(\mathbf{r}) + n^{\mathrm{AE},1}(\mathbf{r}) \tag{1.65}$$

where $n^{\mathrm{PS}}(\mathbf{r})$ is the pseudo-charge density, while the other two terms represent the pseudo-density and the actual density of a particular site, defined respectively as:

$$\begin{aligned} n^{\mathrm{PS}}(\mathbf{r}) &= \langle\psi_n^{\mathrm{PS}}|r\rangle\langle r|\psi_n^{\mathrm{PS}}\rangle \\ n^{\mathrm{PS1}}(\mathbf{r}) &= \sum_{i,j}\langle\phi_i^{\mathrm{PS}}|r\rangle\langle r|\phi_i^{\mathrm{PS}}\rangle\langle\psi_n^{\mathrm{PS}}|p_i^{\mathrm{PS}}\rangle\langle p_j^{\mathrm{PS}}|\psi_n^{\mathrm{PS}}\rangle \\ n^{\mathrm{AE1}}(\mathbf{r}) &= \sum_{i,j}\langle\phi_i^{\mathrm{AE}}|r\rangle\langle r|\phi_i^{\mathrm{AE}}\rangle\langle\psi_n^{\mathrm{PS}}|p_i^{\mathrm{PS}}\rangle\langle p_j^{\mathrm{PS}}|\psi_n^{\mathrm{PS}}\rangle \end{aligned} \tag{1.66}$$

The PAW method allows us to describe the wave-functions of the valence orbitals, properly orthogonalized at the core wave-functions, even in core frozen approximation, i.e. it was assumed they do not satisfy the different chemical configurations in which the atom can be considered [24].

1.8 Spin-polarized DFT, collinear and non collinear magnetic ordering

The Kohn-Sham theory can also be extended to spin-polarized systems [25]. In this case, the electron density is constituted by two spin independent densities n_+ and n_-. Each of these densities is built through Kohn-Sham orbitals, and satisfies the equation:

$$\left\{-\frac{\hbar}{2m}\nabla^2 + V_s^s(\mathbf{r})\right\}\phi_i^s(\mathbf{r}) = \varepsilon_i^s\phi_i^s(\mathbf{r}) \tag{1.67}$$

where s indicates the spin component $+$ or $-$. In this case, the potential in (1.40), is defined as:

$$V_s^s(\mathbf{r}) = V_{\text{ext}}(\mathbf{r}) + e^2 \int \frac{n(\mathbf{r}')}{|\mathbf{r} - \mathbf{r}'|} d\mathbf{r}' + v_{xc}^s \left[n_+, n_-\right](\mathbf{r}) \tag{1.68}$$

and the potential for exchange and correlation:

$$v_{xc}^s \left[n_+, n_-\right] \equiv \frac{\delta E_{xc}\left[n_+, n_-\right]}{\delta n^s(\mathbf{r})}. \tag{1.69}$$

The spin density, built with the Kohn-Sham orbitals, is expressed as:

$$n^s(\mathbf{r}) = \sum_i^{N^s} |\phi_i^s(\mathbf{r})|^2 \tag{1.70}$$

with N^s number of occupied orbital.

In general, for a spin-polarized system, the density of the spins is considered having a single direction (collinear), coincident with z-axes by convention. In more complex structures, otherwise, the density of the spins or, better, the density of the magnetization, varies in all directions of space (non-collinear). Figure 1.2 displays the different types of collinear and non-collinear magnetic ordering. Noncollinear magnetic ordering may arise from a topological frustration of exchange interactions, the competition between spin- and orbital magnetism, from competing ferromagnetic and antiferromagnetic interactions in disordered alloys [24].

A generalization of LSDA functional, for non-collinear magnetism, was proposed by Kübler *et al.* [26]. In this case, the magnetization associated with different atoms in a unit cell, is allowed to point along different, non collinear, directions and provides the spin quantization axes. Only the GGA leads reliable and accurate results [27] while the LSDA predicts often the wrong ground state. The success of GGA's derives from their ability to correct many of the limitations of the LSD without increasing the computational cost significantly.

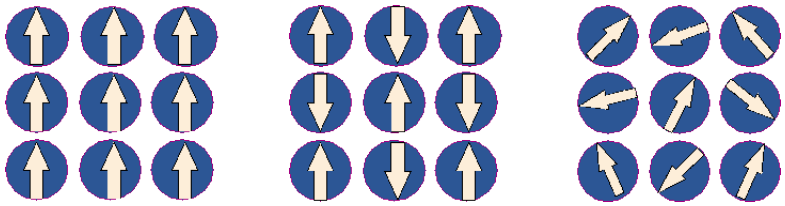

Figure 1.2: Schematic of the distinction between collinear ferromagnetic (left) and antiferromagnetic (center) and non-collinear (right) moment configuration. Ref. [28].

For a system of interacting electrons, immersed in a magnetic potential the potential can be written

$$\hat{U} = \sum_i V(\mathbf{r}_i) + 2\mu_B \sum_i B(\mathbf{r}_i) \cdot \hat{\mathbf{S}}_i \tag{1.71}$$

where $B(\mathbf{r}_i)$ is the magnetic field, $\mu_B = \frac{e\hbar}{2m_e}$ is the Bohr magneton and $\hat{\mathbf{S}}_i$ is the i-th electron spin operator. The energy will be a function of the density matrix $n_{\alpha\beta}$ in which α and β are the spins along a defined direction. The total density matrix may then be defined as

$$\mathrm{Tr}\left[n_{\alpha\beta}(\mathbf{r})\right] \equiv n_{Tr}(\mathbf{r}) = \sum_{\alpha\beta} n_{\alpha\alpha}(\mathbf{r})\delta_{\beta\alpha} = n_+(\mathbf{r}) + n_-(\mathbf{r}) \tag{1.72}$$

In a magnetic system non-collinear the off-diagonal elements are nonzero, and the density matrix is expressed as:

$$n_{\alpha\beta} = \frac{1}{2} n_{Tr}(\mathbf{r})\delta_{\beta\alpha} + \mathbf{m} \cdot \boldsymbol{\sigma}_{\alpha\beta} \tag{1.73}$$

where

$$m(\mathbf{r}) = -\mu_B \sum_{\alpha\beta} n_{\beta\alpha}(\mathbf{r})\boldsymbol{\sigma}_{\beta\alpha} = -\mu_B[n_+(\mathbf{r}) - n_-(\mathbf{r})] \tag{1.74}$$

is the density of magnetic momentum or magnetization, and $\boldsymbol{\sigma} = (\sigma_x, \sigma_y, \sigma_z)$ is the vector of the Pauli spin matrices.

Exchange and correlation energy. In this formalism, the exchange and correlation energy is not known in general, but only for a spin-polarized homogeneous electron gas with charge density $n_{\alpha\beta}$ defined in (1.72), and magnetization density $m(\mathbf{r})$, defined in (1.74):

$$E_{xc}\left[n_{\alpha\beta}\right] = \int n_{Tr}(\mathbf{r})\varepsilon_{xc}\left[n_{\alpha\beta}(\mathbf{r})\right] d\mathbf{r} = \int n_{Tr}(\mathbf{r})\varepsilon_{xc}\left[n_{Tr}(\mathbf{r}), |\mathbf{m}(\mathbf{r})|\right] d\mathbf{r} \tag{1.75}$$

The Kohn-Sham potential is:

$$V_s(\mathbf{r}) = V_0(\mathbf{r}) + \int \frac{n(\mathbf{r}')}{|\mathbf{r} - \mathbf{r}'|} d\mathbf{r}' + V_{xc}(\mathbf{r}) \tag{1.76}$$

$$\mathbf{B}_s(\mathbf{r}) = \mathbf{B}_0(\mathbf{r}) + \mathbf{B}_{xc}(\mathbf{r}) \tag{1.77}$$

where the exchange and correlation potential consisting of a scalar contribution, is defined as:

$$V_{xc}\left[n_{\alpha\beta}\right](\mathbf{r}) = \frac{\delta E_{xc}\left[n_{\alpha\beta}\right]}{\delta n_{Tr}(\mathbf{r})} = \varepsilon_{xc}\left[n_{\alpha\beta}\right](\mathbf{r}) + n_{Tr}(\mathbf{r})\frac{\partial E_{xc}\left[n_{\alpha\beta}(\mathbf{r})\right]}{\partial n_{Tr}(\mathbf{r})} \tag{1.78}$$

and the magnetic exchange and correlation field is:

$$\mathbf{B}_{xc}\left[n_{\alpha\beta}\right](\mathbf{r}) = -\frac{\delta E_{xc}\left[n_{\alpha\beta}\right]}{\delta \mathbf{m}(\mathbf{r})} = \mathbf{e}(\mathbf{r})n_{Tr}(\mathbf{r})\frac{\partial \varepsilon_{xc}\left[n_{\alpha\beta}(\mathbf{r})\right]}{\partial |\mathbf{m}(\mathbf{r})|} \tag{1.79}$$

where $\mathbf{e}(\mathbf{r}) = \dfrac{\partial \varepsilon_{xc}\left[n_{\alpha\beta}\right]}{\partial |\mathbf{m}(\mathbf{r})|}$ is the local direction of the magnetization at the point $\mathbf{r}$.

Pseudopotentials. The noncollinear PAW formalism differs from that described in Section 1.7.1. The major difference in non-collinear formalism is that the spin indices are included. In the PAW approach, charge and spin densities are decomposed into pseudodensities and compensation densities accounting for the difference between the pseudodensities and all-electron densities. In this contest, the density matrix $n_{\alpha\beta}(\mathbf{r})$ is composed of a soft pseudodensity and augmentation and compensation contributions in complete analogy to the scalar case. The generalization is straightforward it is sufficient to add spin indices to the pseudo-wave-function $|\Psi_m\rangle$. The AE wave function Ψ_m^α is derived from the pseudo-wave function $\tilde{\Psi}_m^\alpha$ by means of a linear transformation:

$$|\Psi_m^\alpha\rangle = |\tilde{\Psi}_m^\alpha\rangle + \sum_i \left(|\phi_i\rangle - |\tilde{\phi}_i\rangle\right)\langle \tilde{p}_i|\tilde{\Psi}_m^\alpha\rangle \tag{1.80}$$

where the index i is referred to the atomic site, the index m stands for the band-index and the $\mathbf{k}$ points within the first Brillouin zone. The ψ_i is the AE partial waves, obtained for a nonmagnetic reference atom by radially integrating the Schrödinger equation for a set of energies ε_k and are orthogonalized to the core states, the pseudo partial waves $\tilde{\phi}_i$ are equivalent to the AE partial waves outside a core radius r_c and match continuously onto ψ_i inside the core radius. The core radius r_c is usually chosen approximately around half the nearest neighbor distance. The projector functions $\tilde{p}_i$ are dual to the partial waves:

$$\langle \tilde{p}_i|\tilde{\phi}_i\rangle = \delta_{ij} \tag{1.81}$$

Startin from eq. (1.80) the AE total density matrix is given by:

$$n_{\alpha\beta}(\mathbf{r}) = \tilde{n}_{\alpha\beta}(\mathbf{r}) + n^1_{\alpha\beta}(\mathbf{r}) - \tilde{n}^1_{\alpha\beta}(\mathbf{r}) \tag{1.82}$$

where $\tilde{n}$ is the the soft pseudodensity matrix calculated directly from the pseudo-wave functions on a plane-wave grid:

$$\tilde{n}_{\alpha\beta}(\mathbf{r}) = \sum_m f_m \langle \tilde{\Psi}^\beta_m | \mathbf{r} \rangle \langle \mathbf{r} | \tilde{\Psi}^\alpha_m \rangle \tag{1.83}$$

where f_m is the Fermi-Dirac occupation function.
The on-site charge-densities are defined as:

$$n^1_{\alpha\beta}(\mathbf{r}) = \sum_{m,(i,j)} f_m \langle \tilde{\Psi}^\beta_m | \tilde{p}_i \rangle \langle \phi_i | \mathbf{r} \rangle \langle \mathbf{r} | \phi_j \rangle \langle \tilde{p}_j | \tilde{\Psi}^\alpha_m \rangle \tag{1.84}$$

$$\tilde{n}^1_{\alpha\beta}(\mathbf{r}) = \sum_{m,(i,j)} f_m \langle \tilde{\Psi}^\beta_m | \tilde{p}_i \rangle \langle \tilde{\phi}_i | \mathbf{r} \rangle \langle \mathbf{r} | \tilde{\phi}_j \rangle \langle \tilde{p}_j | \tilde{\Psi}^\alpha_m \rangle. \tag{1.85}$$

In summary, for magnetic calculations, orbitals and charge densities must be calculated separately for spin-up and spin-down electrons. A total charge-density and a spin-density may be calculated by taking the sum and the difference of the spin-up and spin-down densities, respectively. As long as only collinear magnetic structures with a fixed spin-quantization axis are considered, charge and spin densities are scalar quantities and the step from nonspin-polarized to spin-polarized calculations is trivial [29].

CHAPTER 2

Ferroelectricity and structural phase transitions

Ferroelectricity is a property of certain nonconducting crystals, or dielectrics, that exhibit spontaneous electric polarization[1], that can be reversed in direction by the application of an appropriate electric field. Ferroelectric materials are subjected to a structural phase transition. Below a transition temperature called the Curie temperature, $T_c = T_{Curie}$, this materials are polar and possess a spontaneous polarization or electric dipole moment. Above T_c, the materials have a centrosymmetric structure and no electric dipole moment is present. The nonpolar phase encountered above the Curie temperature is known as the paraelectric phase.

The direction of the spontaneous polarization conforms to the crystal symmetry of the material. While the reorientation of the spontaneous polarization is a result of atomic displacements. Summarizing, the characteristic properties of ferroelectrics include spontaneous electric polarization, polarization reversal, where the polarity can be reoriented, or reversed fully or in part, through the application of an electric field, (switching), and disappearance of the polarization above a ferroelectric phase transition temperature T_{Curie}.

In this framework, the simplest theory of structural phase transitions is Landau's (1937) phenomenological theory.

[1]Electric polarization consists in a separation of the centre of positive and negative electric charge, making one side of the crystal positive and the opposite side negative

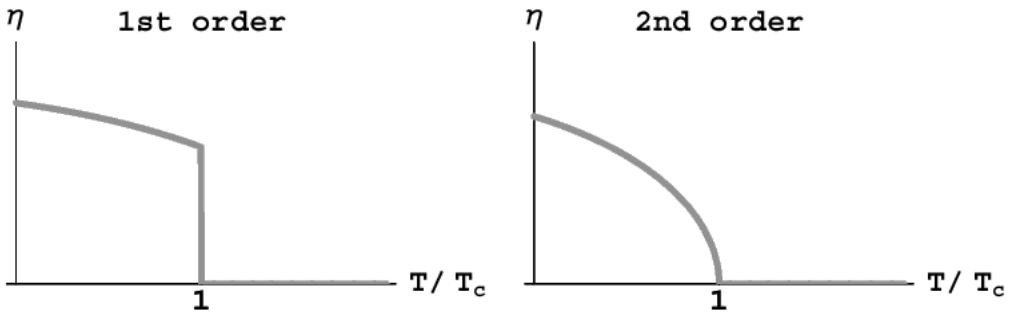

Figure 2.1: Typical behaviour of the order parameter η at a phase transition. Above T_c η is vanishing and below T_c η has some finite value.

Landau's Theory. Based exclusively on symmetry considerations, Landau's theory can provide a reliable description of a system's equilibrium behaviour near a phase transition. Landau's theory characterizes the transition in terms of an order parameter, η, a physical entity that is zero in the high-symmetry (disordered) phase, and changes continuously to a finite value once the symmetry is lowered: the paraelectric-ferroelectric transition.
Landau's theory assumes that the free energy of one unit cell of the crystal may be expanded in a power series in this order parameter;

$$F(\eta) = F_0 + \alpha\eta^2 + \beta\eta^3 + \gamma\eta^4 ... \tag{2.1}$$

where the coefficients F_0, α, β and γ may be functions of temperature. The phase stability is obtained minimizing the energy, it means that:

$$\left.\frac{\partial F(\eta)}{\partial \eta}\right|_{\eta_0} = 0 \qquad \left.\frac{\partial^2 F(\eta)}{\partial \eta^2}\right|_{\eta_0} > 0 \tag{2.2}$$

The high-symmetry phase $\langle\eta\rangle = \eta_0 = 0$ is then stable only if the linear term in η in eq. (2.1) is absent and if α is positive. The system is distorted if α is negative. Furthermore, at a continuous phase transition $F(\eta)$ must increase with $|\eta|$ at T_c, $\alpha = 0$, so that $\beta = 0$ and $\gamma > 0$. So, the energy must be invariant with respect to symmetry operation $\eta \to -\eta$

During the temperature changes, the crystal changes its symmetry continuously, when $T=T_c$ it takes a sudden change. Above the temperature T_c, the crystal is in the phase 1, for $T<T_c$ the crystal is in the phase 2.

Landau's theory is then completed by the further assumption that since α changes sign at T_c, it can be written as an analytic function of T near T_c:

$$\alpha = a(T - T_c), \qquad \gamma = u > 0 \tag{2.3}$$

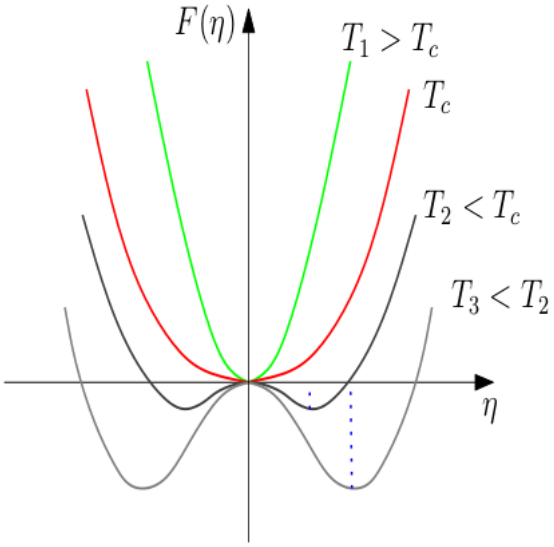

Figure 2.2: $F(\eta)$ as a function of order parameter, for different values of temperature. The minimum of the free energy below T_c should occur at $\eta \neq 0$ and above T_c at $\eta = 0$.

where u is assumed to be independent of temperatures close to T_c.

$$F(\eta) = F_0 + a(T - T_c)\eta^2 + u\eta^4 ... \tag{2.4}$$

The stability conditions for the low-temperature phase is obtained applying the condition in eq. (2.2):

$$2\eta \left[a(T - T_c) + 2u\eta^2\right] = 0 \tag{2.5}$$

whose solutions are:

$$\eta = 0 \qquad \eta = \pm\sqrt{\left[\frac{a(T_c - T)}{2u}\right]} \tag{2.6}$$

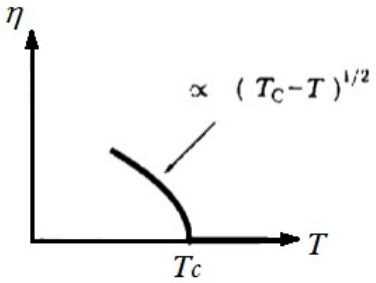

The first solution is true at any temperature, although for $T < T_c$ there are metastable positions, which can be determined by studying the second derivative of the free energy. The second solution is only valid for $T < T_c$.

Follow this theory, considering the polarization as the order parameter, it is possible to obtain the value of the spontaneous polarization in the ferroelectric phase, where

$$P_s = \pm\sqrt{\frac{1}{2u}}\left[(T_c - T)\right]^{\frac{1}{2}}, \qquad T < T_c \tag{2.7}$$

The equilibrium temperature of transition from paraelectric to ferroelectric phase is $T_c = T_{Curie}$; all the properties are dependent on the difference between the crystal temperature T and the phase transition temperature T_c. The $\pm$ signs indicate that the polarization can point in either direction along the symmetry axis (recall that this is the uniaxial case), and correspond to the two energetically equivalent states of the ferroelectric crystal at zero electric field.

Ab initio theory of the ferroelectric phase transition is based on density functional theory, developed be Kohn, Hohenberg and Sham, described in the previous chapter, using the Kohn-Sham formalism. In the next section, I will briefly explain the applications of the first principles calculations to ferroelectric crystals, resorting to the VASP code. The method used in this code is based on works of R. Resta, R. D. King-Smith and D. Vanderbilt.

2.1 Polarization as Berry phase

The macroscopic electric polarization of a crystal is defined as the dipole moment per unit volume:

$$\mathbf{P} = \frac{1}{V}\left[-e\sum_j Z_j\mathbf{R}_j + \int \mathbf{r}n(\mathbf{r})d\mathbf{r}\right] \tag{2.8}$$

where e is the electron charge, V the crystal volume, $\mathbf{R}_j$ is the jth lattice vector, $-eZ_j$ is the ionic charges and $n(\mathbf{r})$ is the electronic charge density.

Furthermore, the measured quantity is not P (P is not a bulk property) but the difference in polarization between two different states of the same crystal,

$$\Delta\mathbf{P} = \int_0^1 d\lambda \frac{d\mathbf{P}}{d\lambda} \tag{2.9}$$

where the parameter λ varies continuously between the two configurations.
A variation of the polarization is related to perturbations of the crystal, for example, by applying a strain (piezoelectric crystal), a temperature change (pyroelectric crystal), or a spontaneous polarization generated by an external electric field (ferroelectric crystal) [30]. As an instance, in a piezoelectric crystal, the macroscopic polarization difference is calculated between the strained and unstrained structures of the crystal.

From the theoretical point of view the macroscopic electronic polarization of

an insulating crystal is defined by the "Modern Theory of Polarization" proposed by R. Resta, R. D. King-Smith and D. Vanderbilt [31–35]. This theory assumes polarization can be computate in electronic structure codes through the Berry phase of the electronic Bloch wave-functions. This theory applies to the case of zero temperature and zero electric field. The last condition is necessary to consider the Hamiltonian, describing the crystal periodic, with eigenfunctions in Bloch form. The potential is no longer a periodic function in presence of a macroscopic field.

The electronic contribution to the difference in the polarization has been identified by King-Smith and Vanderbilt as a geometric phase of the valence wave functions, **Berry Phase**, due to a change in the Hamiltonian of the adiabatic system [31]:

$$\Delta \mathbf{P}_e = \int_{\lambda_1}^{\lambda_2} \frac{\partial \mathbf{P}_e}{\partial \lambda} d\lambda \tag{2.10}$$

with:

$$\frac{\partial \mathbf{P}_e}{\partial \lambda} = \frac{i|e|\hbar}{NVm_e} \sum_{\mathbf{k}} \sum_{n=1}^{M} \sum_{m=M+1}^{\infty} \frac{\langle \Psi_{n\mathbf{k}}^{(\lambda)} | \hat{\mathbf{p}} | \Psi_{m\mathbf{k}}^{(\lambda)} \rangle \langle \Psi_{m\mathbf{k}}^{(\lambda)} | \frac{\partial V^{\lambda}}{\partial \lambda} | \Psi_{n\mathbf{k}}^{(\lambda)} \rangle}{\left(\epsilon_{n\mathbf{k}}^{(\lambda)} - \epsilon_{m\mathbf{k}}^{(\lambda)} \right)^2} + c.c. \tag{2.11}$$

where m_e is the electronic mass, e is the electronic charge, N is the number of unit cells in the crystal, M is the number of occupied bands, $\hat{\mathbf{p}}$ is the momentum operator, and the $\Psi_{n\mathbf{k}}^{(\lambda)}$ are the Bloch functions[2], solutions to the crystalline Hamiltonian. In addition, the potential V^{λ}, is the Kohn-Sham potential [33].

Now $\Delta \mathbf{P}_e = \mathbf{P}_e^{\lambda_2} - \mathbf{P}_e^{\lambda_1}$, where:

$$\mathbf{P}_e^{\lambda} = -\frac{if|e|}{8\pi^3} \sum_{n=1}^{M} \int_{BZ} d\mathbf{k} \langle u_{n\mathbf{k}}^{\lambda} | \nabla_{\mathbf{k}} | u_{n\mathbf{k}}^{\lambda} \rangle \tag{2.12}$$

where f is the occupation number of states in the valence band, $u_{n\mathbf{k}}^{\lambda}$ is the periodic eigenstate of the Bloch function. The sum n runs over all M occupied bands. The previous expression (eq. (2.12)) can be written in terms of *Wannier functions* as:

$$\mathbf{P}_e^{\lambda} = -\frac{f|e|}{V} \sum_{n=1}^{M} \langle W_n^{\lambda} | \mathbf{r} | W_n^{\lambda} \rangle \tag{2.13}$$

with W_n is the Wannier function associated with valence band n. Unlike the Bloch functions which are delocalized in space, the Wannier functions are localized. In

[2] $\Psi_{n\mathbf{k}}(\mathbf{r}) = e^{i\mathbf{k}\cdot\mathbf{r}} u_{n\mathbf{k}}(\mathbf{r})$

eq. (2.13) the change in polarization of a solid is proportional to the displacement of the charge centers

$$\mathbf{r}_n \langle W_n^\lambda | \mathbf{r} | W_n^\lambda \rangle \tag{2.14}$$

of the Wannier functions corresponding to valence bands. Rewriting this expression in terms of the periodic cell functions:

$$\mathbf{r}_n = -\frac{if|e|}{8\pi^3} \sum_{n=1}^{M} \int_{BZ} d\mathbf{k} e^{i\varphi_n(\mathbf{k})} \langle u_{n\mathbf{k}}^\lambda | \nabla_\mathbf{k} | u_{n\mathbf{k}}^\lambda \rangle \tag{2.15}$$

Compare eq. (2.12) with eq. (2.15) results that the change in polarization ΔP is only well-defined modulo $\frac{f|e|\mathbf{R}}{V}$, where $\mathbf{R}$ is a lattice vector. Wannier functions is invariant modulo $\mathbf{R}$, with respect to the choice of phase of the Bloch functions. Multiplying each $|\Psi_{n\mathbf{k}}\rangle$ for one phase $e^{i\varphi_n(\mathbf{k})}$, where $\varphi_n(\mathbf{k})$ is a real function of k, you get a set of functions that are still eigenstates of the Hamiltonian. The phase factor, however, is not canceled out in the calculation of Wannier functions, which therefore are not invariant under gauge transformations.

Computational method. In the eq. (2.12) is not specified the relationship between the phase of the eigenvectors $u_{n\mathbf{k}}^\lambda$ generated by a numerical diagonalization routine. The problem can be result dividing the eq. (2.12) into three equations, one for each component of $\mathbf{P}_e^\lambda$ in the three directions of the vectors of the reciprocal lattice $\mathbf{G}_i$, so that, for example:

$$\mathbf{G}_i \cdot \mathbf{P}_e^\lambda = -\frac{if|e|}{8\pi^3} \int_A dk_2 dk_3 \sum_{n=1}^{M} \int_0^{|\mathbf{G}_1|} dk_1 \langle u_{n\mathbf{k}}^\lambda | \frac{\partial}{\partial k_1} | u_{n\mathbf{k}}^\lambda \rangle \tag{2.16}$$

Consequently,

$$\sum_{i=1}^{3} (\mathbf{P}_e^\lambda)_i = \sum_{i=1}^{3} (\mathbf{G}_i \cdot \mathbf{P}_e^\lambda) \frac{\mathbf{R}_i}{2\pi} \tag{2.17}$$

with $\mathbf{R}_i \cdot \mathbf{G}_i = 2\pi$. In addition, the surface integral in eq. (2.16) can be represented in two dimensions, by a k-points Monkhorst-Pack grid [14], defined as $\mathbf{k}_\perp$. To remove the influence of the arbitrary phase of the functions $u_{n\mathbf{k}}^\lambda$, introduced by the diagonalization routine, King-Smith e Vanderbilt proposed to replace the integral with:

$$\phi_J^{(\lambda)}(\mathbf{k}_\perp) = \mathrm{Im} \left\{ \ln \prod_{j=0}^{J-1} \det \left(\langle u_{m\mathbf{k}_j}^{(\lambda)} | u_{n\mathbf{k}_{j+1}}^{(\lambda)} \rangle \right) \right\} \tag{2.18}$$

which it is determined by calculating the periodic part of the wave function from a string of points k, $\mathbf{k}_j = \mathbf{k}_\perp + j\mathbf{G}_\parallel/J$, with $j = 0, ..., J-1$ So, for J large enough, you have:

$$\phi_J^{(\lambda)}(\mathbf{k}_\perp) = -i\sum_{n=1}^{M}\int_0^{|G_\parallel|} dk_\parallel \langle u_{n\mathbf{k}}^{(\lambda)}|\frac{\partial}{\partial k_\parallel}|u_{n\mathbf{k}}^{(\lambda)}\rangle \tag{2.19}$$

the functions $u_{n\mathbf{k}_J}^{(\lambda)}$, now, will be determined by:

$$u_{n\mathbf{k}_J}^{(\lambda)}(\mathbf{r}) = e^{-i\mathbf{G}_\parallel\cdot\mathbf{r}}u_{n\mathbf{k}_0}^{(\lambda)}(\mathbf{r}) \tag{2.20}$$

In practice the eq. (2.16) is evaluated by:

$$\left(\mathbf{P}_e^{(\lambda)}\right)_i = \frac{f|e|\mathbf{R}_i}{2\pi V N_{k_\perp}}\sum_{k_\perp}\phi_J^{(\lambda)}(\mathbf{k}_\perp) \tag{2.21}$$

where $N_{k_\perp}$ is the number of points in the perpendicular grid. Changes of the phase of $u_{n\mathbf{k}_J}^{(\lambda)}$ can change the value of the sum in eq. (2.21) by an integer multiple of 2π. Correspondingly the arbitrary constant in the definition of $\phi_J^{(\lambda)}(\mathbf{k}_\perp)$, in the eq. (2.18), arises from the fact that the imaginary part of the log of a complex number is only defined up to a constant multiple of 2π. Therefore $\left(\mathbf{P}_e^{(\lambda)}\right)_i$ will be equal in magnitude to $\frac{f|e|\mathbf{R}_i}{2\pi V N_{k_\perp}}$ instead of $\frac{f|e|\mathbf{R}}{2\pi V}$. The phase, introduced in this way, can be removed if we consider the difference between $\phi_J^{(\lambda_1)}(\mathbf{k}_\perp)$ and $\phi_J^{(\lambda_2)}(\mathbf{k}_\perp)$.

In conclusion, since this geometric phase is defined up to a multiple of 2π, the polarization will be defined up to a *polarization quanta*, given by $\Delta\mathbf{P}_0^{(i)} = \frac{f|e|}{V}\mathbf{R}_i$, where f can be considered as a spin degeneration factor, which assumes the values $f = 2$ systems for non-spin-polarized, while $f = 1$ for spin-polarized systems [36].

In a particular case of a ferroelectric material, the spontaneous polarization can be defined as half of the difference between two states polarized in an opposite manner, or as the difference in polarization between the structure in the ferroelectric phase and the structure center-symmetrical, in the paraelectric phase. In practice, it must calculate the polarization for a number of different configurations between the ferroelectric structure and the reference center-symmetrical and the change of polarization between two of these configurations must be smaller than the polarization quantum [36].

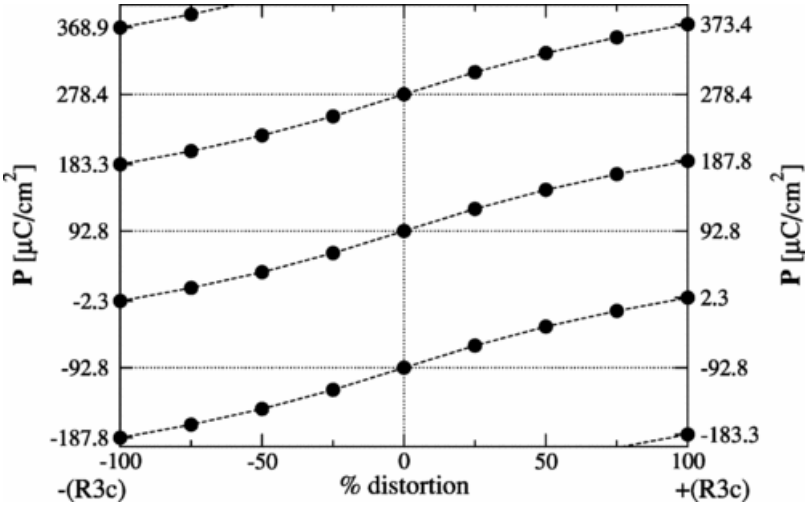

Figure 2.3: Calculated polarization as a function of percentage distortion from the high symmetry non-polar structure (0% distortion) to the ground state *R3c* structure for perovskite $BiFeO_3$ [37].

Figure 2.3 gives an example of the change in polarization P calculated in this way. P is calculated along a path from the original *R3c* structure through the centrosymmetric cubic structure to the inverted $-(R3c)$ structure [37].

Part I

Multiferroicity and magnetoelectricity in a doped topological ferroelectric

This part reports my research on multiferroic materials. Multiferroics, i.e. materials where ferroelectric (FE) and magnetic order coexist in the same phase, have been the focus of much recent interest, due to their basic conceptual interest [36] as well as their potential for practical applications, such as the ability to switch magnetic memories electrically [38]. Unfortunately, materials for which magnetic and electrical order parameters either arise independently, or are coupled (so called multiferroic magnetolectrics) in a single phase are very rare [39]. Evidence of this is schetched in Figure 2.4 which describes the relationship between this type of materials. In particular, the intersection, red hatching, represents materials that are multiferroic, and blue hatching represents materials that exhibit magnetoelectric coupling. The last one is an independent phenomenon that can, but need not, arise in any of the materials that are both magnetically and electrically polarizable [38].

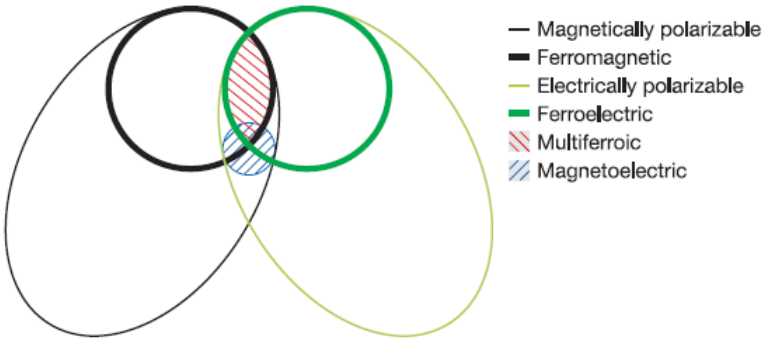

Figure 2.4: Representation of the relationship between multiferroic and magnetoelectric materials. Ref. [38].

The fact that multiferroic magnetoelectric materials are rare is related to the microscopic origin of magnetism and ferroelecticity. An empirical rule states that ferroelectric materials are usually nonmagnetic, while spin-ordered systems seem not to allow ferroelectric distortions. In conventional ferroelectric materials, for example in ABO_3 cubic perovskite structure, the polarization arises when non magnetic cation, B, shift away from the center of the octahedron, as positive and negative charges gives rise to electric dipole moment. In magnetic materials, the magnetic cation remains in the centrosymmetric position, so, no dipole moment is rised.

In other word, this mechanism is related to the competition in covalent band formation. The magnetic properties of atoms, in fact, are determined by ions with partially occupied d-orbital, whereas the electric dipole moment in ferroelectrics arise from stereochemical activity of ions unpaired s-electrons [40].

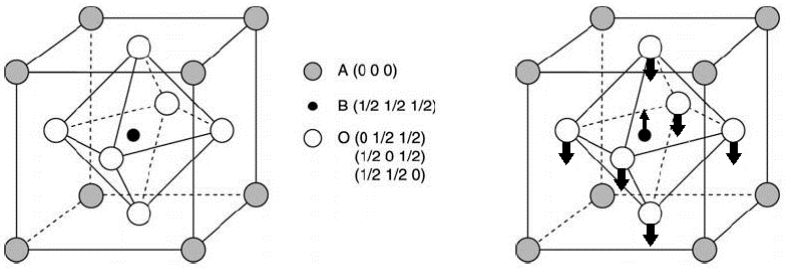

Figure 2.5: Perovskite oxides, of general formula ABO_3 with a pseudocubic structure, where A and B are two different cations, furnish many interesting ferroelectrics. The B-type cation is octahedrally coordinated with oxygen. The left panel shown the relative symmetry breaking displacement of the B-cation with respect to the O atoms which is responsible for the spontaneous polarization.

Formally, the potential energy, in terms of small displacement, Q, is given by the 1^{st} and 2^{nd} Jahn-Teller effect (J-T):

$$E = E_0 + Q\,\langle 0|H_1|0\rangle + \frac{Q^2}{2}\,\langle 0|H_2|0\rangle + \\ -Q^2 \sum_n \frac{|\,\langle 0|H_1|n\rangle\,|^2}{E_n - E_0} + ... \tag{2.22}$$

where $H_1 = \delta H/\delta Q$ and $H_2 = \delta^2 H/\delta Q^2$. The first term is non zero for orbitally degenerate states. The second term, always positive, concerns the nuclei motion with fixed electrons. The last one, always negative, is related to relaxation of electron distribution. The first-order J-T effect arises from incomplete shells of degenerate orbitals whereas, the second, arises from filled and empty molecular orbitals that are close in energy [41].

In other words, conventional ferromagnetism requires d electrons but conventional ferroelectricity requires *"$d^{\,0}$-ness"*. Consequently, the multiferroicity seems to be chemically prohibited.

In the particular case of ABO_3 cubic perovskite structure, sketched in Figure (2.5), J-T effect keeps centrosymmetry of octahedron, but second order J-T effect breaks centrosymmetry of octahedron, and it becomes difficult to design a B site driven multiferroic.

The purpose of this work is to explore an unconventional type of multiferroicity obtained in a particular crystal, belonging to layered-perovskite ferroelectrics of the family $A_nB_nO_{3n+2}$. This study is focus on structural, electronic, ferroelectric and magnetoelectric properties of $La_2Mn_2O_7$, through first-principles based on density functional theory calculations. In particular, this part is organized as follows:

In the Chapter 3, I introduce a mechanism to obtain ferroelectric order compatible with the magnetic order in layered-perovskite oxides. In addition, I explain how ferroelectricity occurs in this particular materials.

Chapter 4 concerns the investigation on magnetic properties of a doped topological ferroelectric oxide. I report the results of the spontaneous polarization, that is calculated using the "*Modern Theory of Polarization*" based on the Berry phase.

Finally, in Chapter 5, I quantify the coupling between electric and magnetic fields trough the determination of the magnetoelectric tensor. I also explain a weak ferromagnetic effect due to Dzyaloshinskii-Moriya interaction.

In conclusion, this work was presented at several international conferences[3] and summarized in a section of the article "Topological multiferroics" published in the journal *Phase Transitions* (Vol. **88**, Iss. 10, 2015).

[3]1) "MAMA-Trend: Trends, challenges and emergent new phenomena in multi-functional materials" May 2013 Sorrento, Italy; 2) "Electronic structure at the cutting edge with Elk" July 2013 Lausanne, Switzerland; 3) School on "Density Functional Theory and Beyond: Computational Materials Science for Real Materials " August 2013 Trieste, Italy; 4) FISMAT2013 "Italian National Conference on Condensed Matter Physics (Including Optics, Photonics, Liquids, Soft Matter) " September 2013 Milano, Italy

CHAPTER 3

Ferroelectricity in a layered perovskite

Recently, it has been suggested [42,43] that a possible way around the mutual incompatibility of magnetism and displacive ferroelectricity can be move away from the ideal ABO_3 cubic perovskite structure and explore alternative mechanisms for ferroelectricity.
As an instance, ferroelectricity in *layered-perovskite oxides* is not displacive, but rather results from dipoles generated by *anti-ferrodistortive*, AFD, oxygen- octahedra rotations, BO_6, which do not compensate and give rise to a net macroscopic polarization due to the layered structure. The rotation of oxygen octahedra is a common AFD instability in perovskite oxides, but not all contribute to polarization, octahedral rotations suppress ferroelectricity in a number of these materials. The layered-perovskite oxides, considered in this work, are structure with general formula $A_nB_nO_{3n+2}$, where n is the number of perovskite-like planes within a layer (Figure 3.1). The stoichiometries are also given as ABO_x with its corresponding ideal oxygen content x=(3+2)/n. Within the layers the corner-shared BO_6 octahedra extend zig-zag-like along the b-axis and chain-like along the a-axis. The layers are n octahedra thick, thus the thickness of the layers rises with increasing n [44].

Figure 3.2 explains the behavior of these distortions comparing bulk and layered perovskite. It shows the electric dipoles that appear as a consequence of the displacement of the oxygen atoms for a layered, on the left, and a non-layered, on the right, perovskite structures. In particular, in left panel are sketched a layer with four of perovskite-like planes. Referring to Figure 3.2 the total dipole

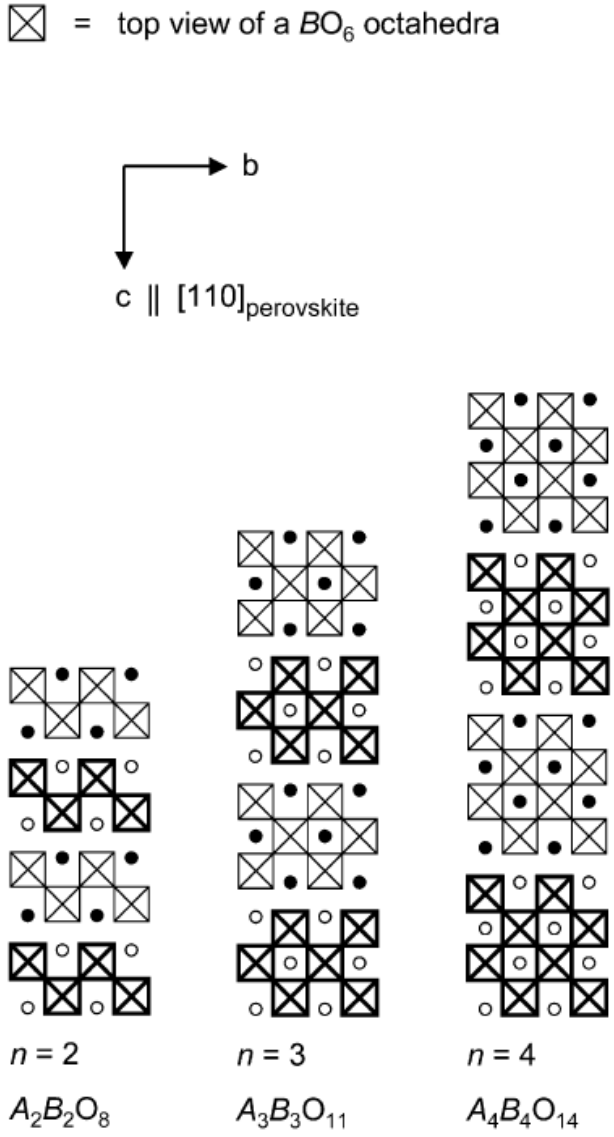

Figure 3.1: Sketch of the idealized (i.e. non-distorted) crystal structure of the n=2, 3 and 4 members of the perovskite-related layered homologous series $A_nB_nO_{3n+2}$ projected along the a-axis. Circles represent the A-cations. Ref. [44].

associated to one layer is $p^{\text{layer}} = 2p_1 + p_2 + p_3 + p_4 \neq 0$ for a layered structure, while $p^{\text{layer}} = 0$ for the bulk structure. The AFD instability in the former causes a spontaneous polarization, while in the latter do not. Since ferroelectricity is due entirely to the layered structure justifies the label "topological" attached to these ferroelectrics [43].

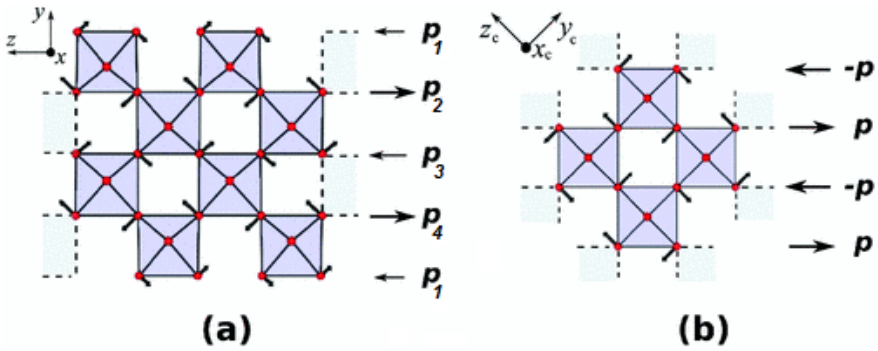

Figure 3.2: Tipical anti-ferrodistortive mode occuring in a layered peroskite oxide on (a) panel. It is shown one layer with $n = 4$ perovskite-like planes. (b) oxygen-octahedra rotations existing in an ideal (non-layered) perovskite structure. Arrows on the site of both sketches represent the electric dipole associated to distortion. Ref. [43].

Among the layered-perovskite oxides I have considered the Lanthanumtitanate, $La_2Ti_2O_7$, (hereafter denoted as LTO). LTO is a n=4 member of the family of layered compounds, sketched in Figure 3.1. In particular, LTO consists of blocks of four perovskite units, TiO_6 stacked along a [011] direction, with each block separated by an additional layer, as shown in Figure 3.3.
López-Pérez and Íñiguez [43] have studied the origin of ferroelectricity in this type of layered perovskites. They have determined that LTO is one of the materials with the highest ferroelectric Curie temperature known (1770 K), a sizeable spontaneous polarization P_s =29μC/cm^2 and high permittivity $\varepsilon \sim 50$. These properties make LTO a potential candidate for multiple applications, in particular, in the field of information storage, in fact ferroelectric properties are essentially used to manufacture of ferroelectric random access memory elements [45].

At 1770K LTO transforms its orthorhombic structure, which corresponds to the ferroelectric (FE) phase, with the space group $Cmc2_1$ ($N_0 = 36$), into the paraelectric (PE) phase, $Cmcm$ ($N_0 = 63$). This structure are sketched in Figure 3.4. This transformation occurs through the combination of a rotation distortion of the oxygen octahedra.

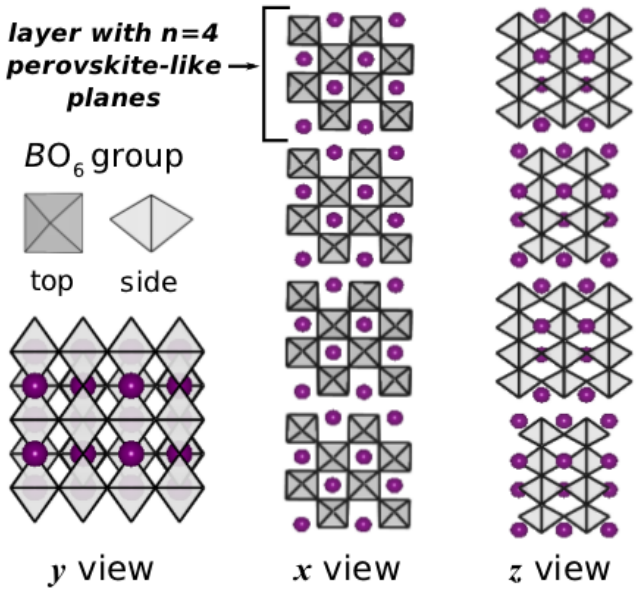

Figure 3.3: The structure of the $La_2Ti_2O_7$ layered perovskite in the non-distorted phase in x, y, z views. Ref. [43].

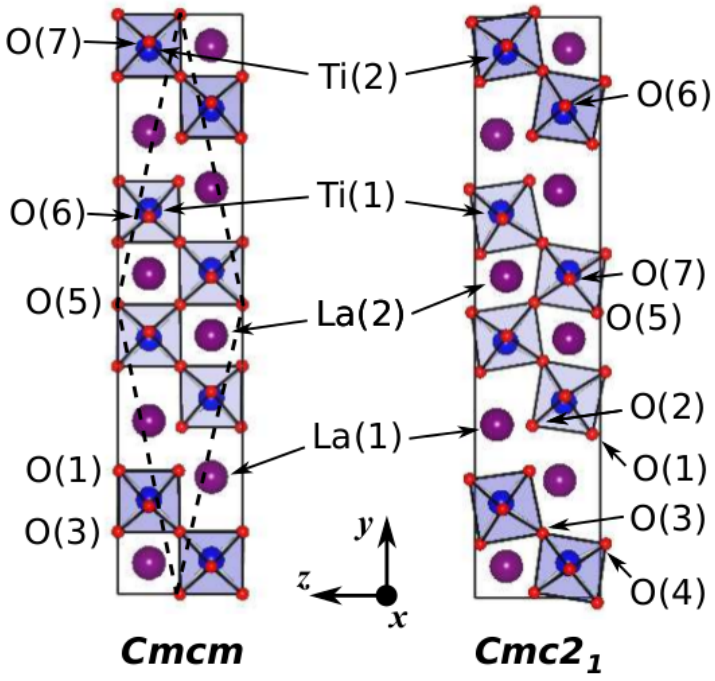

Figure 3.4: The structures involved in the $La_2Ti_2O_7$ phase transition, PE phase on the left and FE phase on the right. Ti ions (blue) are surrounded by oxygen octahedra (O red), with La ions (violet) interspersed. Ref. [43].

CHAPTER 4

Multiferroic material: $La_2Mn_2O_7$

In order to achieve multiferroicity in a topological ferroelectric layered perovskite could be consider a doping or a full substitution of the B-cation, non magnetic, by a magnetic cation. Following this idea, $La_2Mn_2O_7$ (LMO) has been built from full substitution of Ti by Mn in LTO. This compound, since Mn is a magnetic cation having valence 4+ with $3d^3$ configuration, presupposes magnetic properties in addition to ferroelectricity.

As a result of the isovalent substitution, LMO adopts orthorhombic structures, with space groups *Cmcm* and $Cmc2_1$ for paraelectric (PE) and ferroelectric (FE) phases, as in Ref. [43] for LTO. (Indeed, it is not known whether the synthesis of LMO is possible and which structure will result, given the competition with other phases such as $LaMnO_3$.)

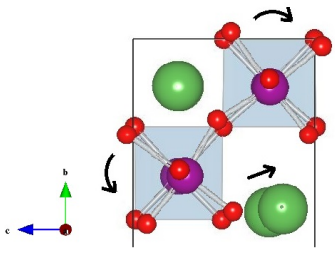

The distorsion has involved only the plane *bc*, in fact the components along the *a*-axis are unchanged. As shown in the figure on the left, it is evident that the structural instability is predominantly due to oxygen octahedra rotations around the *a*-axis, though there is a negligible La and Mn displacement.

Both orthorhombic structures have been optimized in volume and ionic configurations. First-principles calculations have been performed using the Generalized Gradient Approximation (GGA) of the theory of Density Functional (DFT), as implemented in the Vienna Ab Initio Simulation Package (VASP) [5], for the determination of energy exchange and correlation. This approximation contains

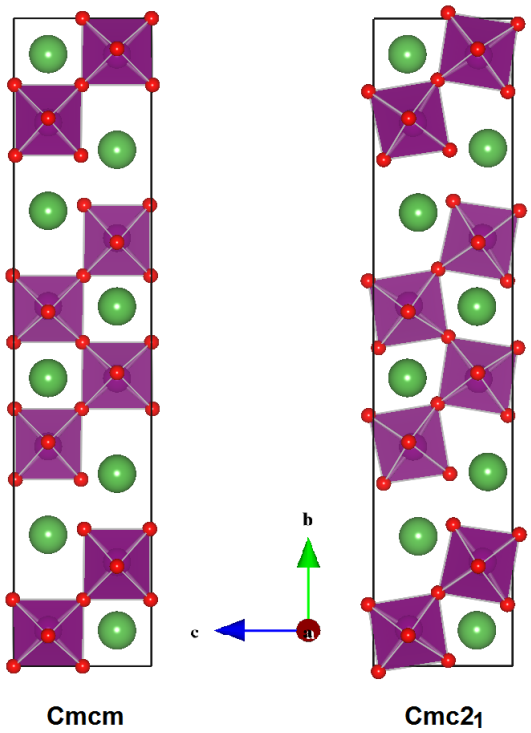

Figure 4.1: Structures involved in PE→FE phase transition of $La_2Mn_2O_7$. *Cmcm* is the centrosymmetric and *Cmc2₁* is the distorted structures, both have 44-atom conventional cell. Coordinate axes are labeled referring to crystallographic axes.

non-local corrections which depend, in absolute value, on the gradient of the charge density and the spin density that lead to a more accurate description of the structural and magnetic properties. The electron-ion interaction has been described by the method of the projector-augmented plane waves, PAW [23, 46], in particular, the ionic core is for La $5s$, $5p$, $5d$, $6s$, Mn $3d$, $4s$, while for the O, the states are $2s$, $2p$. A 350 eV plane wave energy cutoff and a 6×1×5 Monkhorst-Pack **k**-points mesh for Brillouin zone integrations [14] have been used.

The lattice parameters calculated for the *Cmcm*, PE phase, and *Cmc2₁*, FE phase, are listed in the Table A.1 and A.2 in Appendix A. The energy of the ground state to the distorted structure is -354.73088 eV, while for the centrosymmetric structure is -354.42281 eV.

Estimate of T_C. To study the structural phase transition quantitatively, then to calculate the Curie temperature, I have compared the energies, per unit volume, of the phases involves, PE-FE. The difference of energies per unit volume involved in LTO transition results 1.09 meV/Å^3, for $BaTiO_3$ (BTO), in analogous transition *Pm3m* (PE) and *P4mm* (FE) the difference is 0.11 meV/Å^3, that

corresponds to Curie temperatures 1770 K and 400 K, respectively [43]. Consequently, in first approximation, the difference of 0.92 meV/Å^3 corresponds a T_C =1500 K in LMO.

The investigation into the LMO multiferroicity follows with the exploration of different type of magnetic order that this structure can assume.

4.1 Magnetic properties

The particular magnetic order is a result of the magnetic interactions between atoms, expressed as interactions between spins. In the Heisenberg model of these interactions make a contribution to the Hamiltonian of the type:

$$\hat{H}_{spin} = -2\sum_{i\neq j} \mathtt{J}_{ij}\mathbf{S_i}\mathbf{S_j} \tag{4.1}$$

where $\mathtt{J}_{ij}$ is identified as **exchange constant** (exchange integral) between pair spins.

In the simplest case of the interaction between two electrons having the wave function $\psi_a(\mathbf{r}_1)$ and $\psi_b(\mathbf{r}_2)$, respectively, since the total wave function must be antisymmetric for the exchange of two electrons, so only two possible states are possible, one singlet, with χ_S if the spatial part is symmetrical, and one triplet state with χ_T if the spatial part is antisymmetric:

$$\mathbf{\Psi_S} = \frac{1}{\sqrt{2}}\left[\psi_a(\mathbf{r}_1)\psi_b(\mathbf{r}_2) + \psi_a(\mathbf{r}_2)\psi_b(\mathbf{r}_1)\right]\chi_S$$

$$\mathbf{\Psi_T} = \frac{1}{\sqrt{2}}\left[\psi_a(\mathbf{r}_1)\psi_b(\mathbf{r}_2) - \psi_a(\mathbf{r}_2)\psi_b(\mathbf{r}_1)\right]\chi_T$$

The energies of these states are:

$$E_S = \int \mathbf{\Psi}^*_{\mathbf{S}}\hat{H}\mathbf{\Psi_S}d\mathbf{r}_1 d\mathbf{r}_2$$

$$E_T = \int \mathbf{\Psi}^*_{\mathbf{T}}\hat{H}\mathbf{\Psi_T}d\mathbf{r}_1 d\mathbf{r}_2$$

The constant of exchange is expressed as the difference between the singlet state and the triplet:

$$\mathtt{J} = \frac{E_S - E_T}{2}$$

The triplet state is favoured for $\mathtt{J} > 0$, and the interaction is ferromagnetic,

viceversa, singlet state is favoured for the condition $\mathtt{J} < 0$, and the interaction will be antiferromagnetic.

The exchange interaction described above is also known as *direct exchange* short-range. In many compounds with rare earths such interaction can not be responsible for the magnetic behaviour, as there is a sufficient overlap of the orbitals of the two ions interacting [1].

In these compounds the interaction is a **superexchange** indirect long-range interaction between two magnetic ions, M, mediated by a non-magnetic ion which separates them. Figure 4.2 shown, as an example, the superexchange interaction in Cu_2O_2.

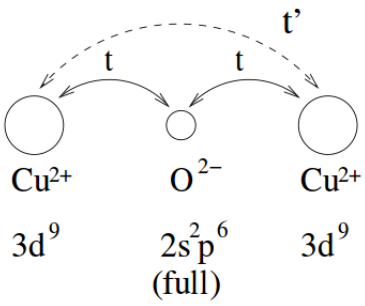

Figure 4.2: Strong antiferromagnetic exchange interaction in cuprates, two Cu^{2+} ions mediated by an oxygen ion O^{2-}. Ref. [47].

If the magnetic ions are the same, as in Cu_2O_2 or MnO, shown in Figure 4.3, the constant of exchange depends on both the interatomic distance that the angle formed by the $M-O-M$ binding. To define the type of interaction I resort to the superexchange semi-empirical rule of Goodenough-Kanamori, formulated by Goodenough [48] and later developed by Kanamori [49].

Goodenough-Kanamori rule: *if the orbitals of the metal ions are partially occupied and the* $M-O-M$ *bond angle is between (120÷180)° the exchange interaction is antiferromagnetic, if one of the two metal ions has an orbital partially occupied and the other an empty orbital, and the bond angle is* $\sim 90°$*, then the exchange is ferromagnetic.*

Figure 4.4 shows some examples of superexchange interation [47] to illustrate this rule.

[1] For example, f orbitals are located very close to the core, there is only a weak probability density that extends beyond the core and then there could be an overlap of the orbitals of the ions first neighbors.

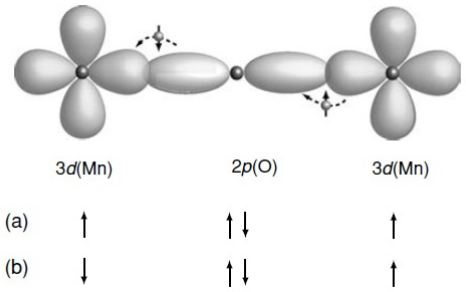

Figure 4.3: In the crystal of MnO, each ion of Mn^{2+} has a orbital $3d$ partially occupied, they are separated by the presence of an ion of O^{2-} and form a bond angle 180°, in agreement with the Goodenough-Kanamori rule, the exchange interaction is antiferromagnetic. In fact, the configuration (a) has a greater energy cost compared to the configuration (b) that, consequently, is favoured. Ref. [50].

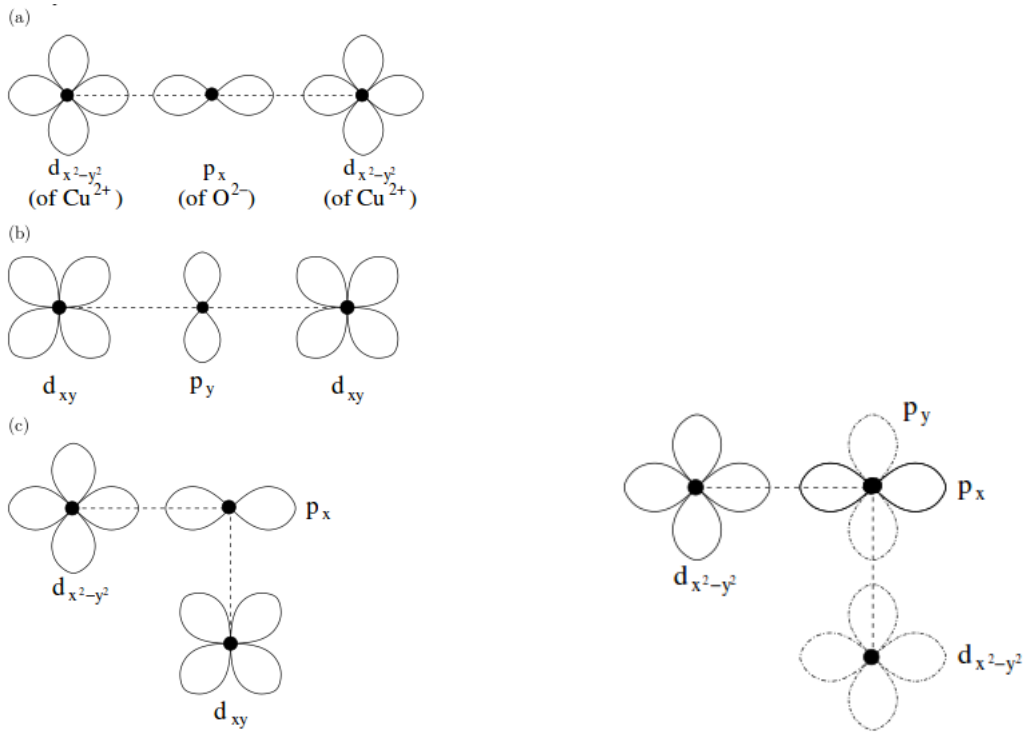

Figure 4.4: Left panel. Strong antiferromagnetic exchange interaction if the half-filled orbitals of two cations overlap with the same empty or filled orbital of the intervening anion. Right panel. Weaker ferromagnetic exchange interaction if the half-filled orbitals of two cations overlap with orthogonal orbitals of the same intervening anion. Ref. [47].

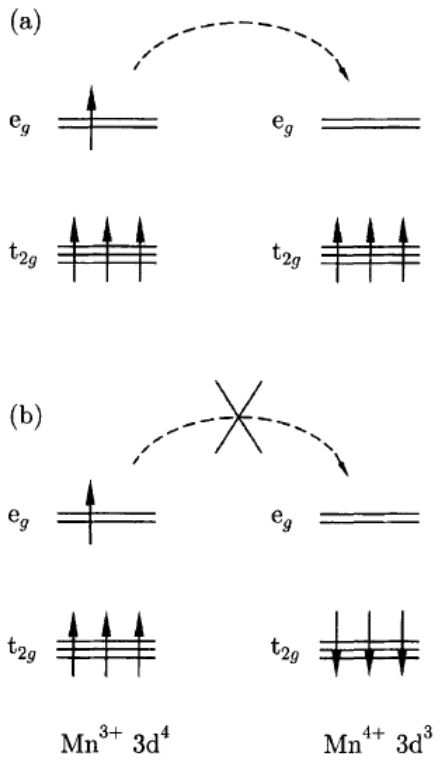

Figure 4.5: Energetically (a) favourite , (b) unfavourite alignment

Some oxides consisting of magnetic ions with different value, however, exhibit a ferromagnetic ordering due to the so-called **double exchange**. Figure 4.5 shows the mechanism of double exchange in a compound in which coexist manganese ions with valence 3+ and 4+. The electron occupying the orbital e_g ion $3d^4$ can make the transfer on the orbital e_g ion $3d^3$ only if the electrons occupying orbitals t_{2g} ion $3d^3$ are aligned ferromagnetically (a). The alignment of ferromagnetic favours charge transport through the crystal, which then becomes metallic [50].

Types of spin ordering in perovskite oxides. There are various combinations of antiferromagnetic alignment of the magnetic moments. In particular, for the perovskite-type transition-metal oxides, some possible configurations, represented in Figure 4.6, are:

A-type: The intra-plane coupling is ferromagnetic while inter-plane coupling is antiferromagnetic.

C-type: The intra-plane coupling is antiferromagnetic while inter-plane coupling is ferromagnetic.

G-type: Both intra-plane and inter-plane coupling are antiferromagnetic.

The G-type is the most frequent, in fact, in this pattern, the superexchange interaction tends to align antiparallel moments of all the first neighbours. But, depending on the overlap of the orbitals, in accord with the rule Goodenough-Kanamori, you can also be obtained coupling ferromagnetic between planes, as in the case of the order of A-type, common in cubic perovskites AMO_3 [51].

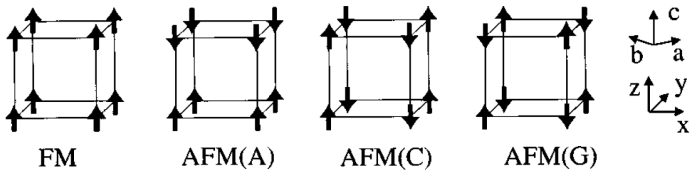

Figure 4.6: Typical magnetic structures for the perovskites. Ref. [51].

4.1.1 Results and discussions

Figure 4.7 shows the different magnetic configurations studied, for each optimized structures in both PE and FE phases.

- **FM** each Mn spins are aligned parallel to other,
- **AFM-a**, between the two blocks of four perovskite units (along the *b*-axis) the Mn spin alignment is antiparallel, while inside each block the spins are aligned in parallel,
- **AFM-b**, within each block, the spins related to two consecutive planes (perpendicular to the axis b) are aligned antiparallel to the axis b, while those regarding to the other two planes are aligned parallel,
- **AFM-c**, is the most stable, and it can be seen as an antiferromagnetic ordering of A-type (see Figure 4.6) given that the spins on a plane have opposite direction to those on the next plane. However, observing the structure rotated 45°, we understand that the interaction is that of local antiferromagnetic structure of G-type (all the neighbours of a given spin are opposite).

The same methods have been used to optimize every structure. In each configuration of the center-symmetrical structure, the $Mn - O - Mn$ bonds form an angle between 170° and 180°, while, in the distorted structure, the bonds varies from 147° to 165°. Then, according to Goodenaugh-Kanamori rule, antiferromagnetic order is energetically favourited, the coupling between two next-to-nearest

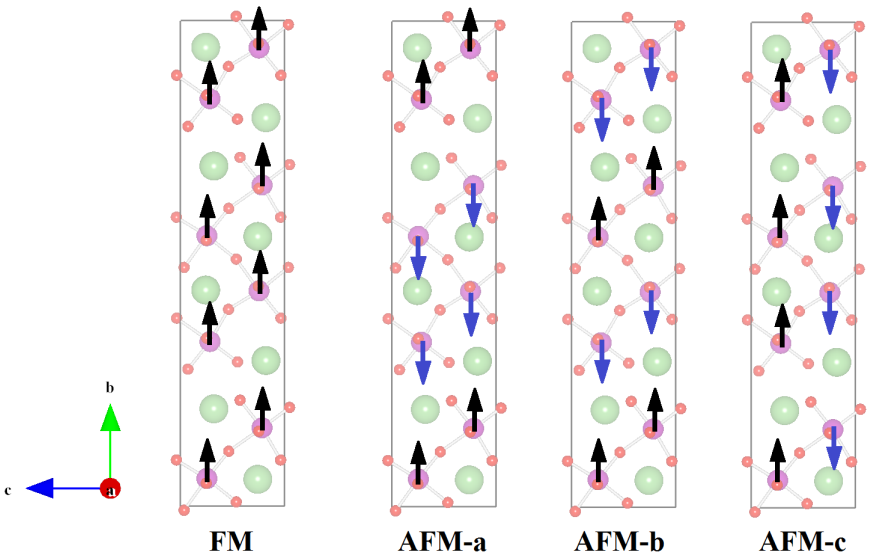

Figure 4.7: Types of magnetic ordering examined.

neighbour cations, Mn^{4+}, through the intermediary oxigen anion is superexchange with an angle $\sim$180°.

The following tables show the values obtained of the total energy, with an error of the order of 10^{-5}eV, the density of the magnetization and the difference in energy between the FM and AFM configurations.

	M(μ_B)	ΔE(eV)
FM	24	0.0
AFM-a	0	–0.0151
AFM-b	0	–0.0861
AFM-c	0	–0.4261

Cmcm

	M(μ_B)	ΔE(eV)
FM	24	0.0
AFM-a	0	–0.0208
AFM-b	0	–0.0564
AFM-c	0	–0.1610

$Cmc2_1$

For both structures, PE and FE, of LMO phases, the configuration AFM-c is that which corresponds to the minimum energy, then is the most favored. All nearest neighbours of a given Mn, that is, have opposite spin, as indeed expected from superexchange between Mn^{4+} ions with majority t_{2g} orbitals. By approximate I mean that the magnetic couplings depend on the respective location of Mn; for example, the coupling between neighbouring Mn in different blocks of the layered structure differs (by about 20%) from that between Mn within the block. The total magnetic moment is almost entirely provided by Mn, for which the magnetization integrated in a sphere of radius has a value of about $\pm$ 2.60 μ_B.

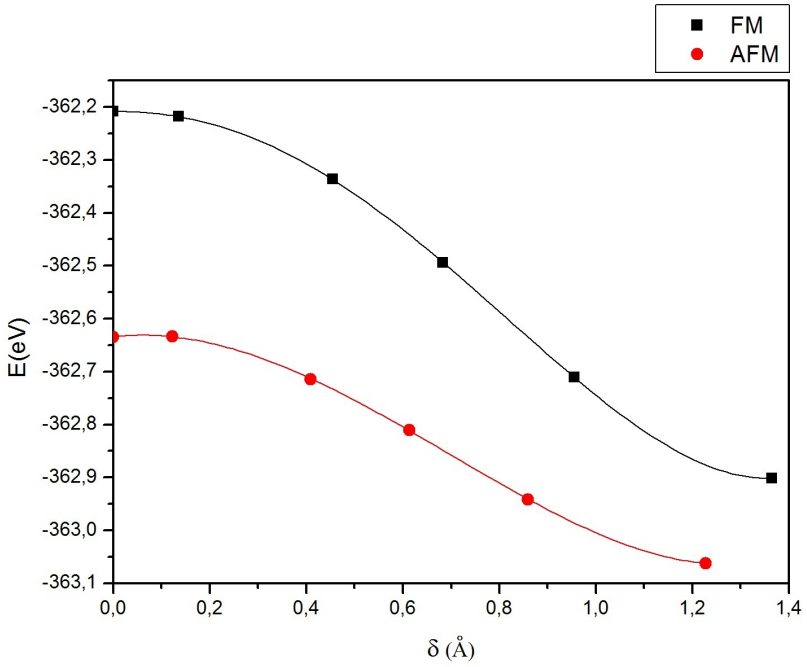

Figure 4.8: Total Energy as a function of the distortion in ferromagnetic, FM, and antiferromagnetic, AFM-C, configurations.

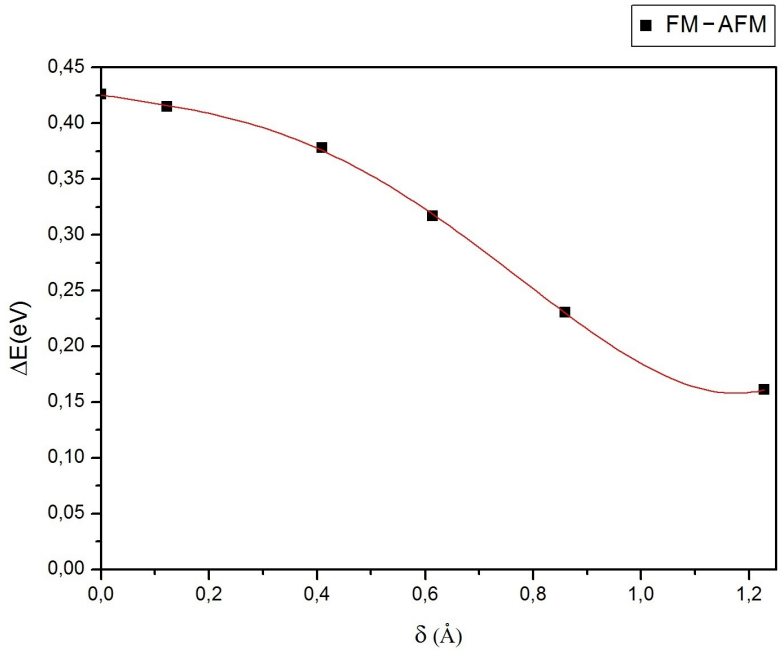

Figure 4.9: Differences in energy between the ferromagnetic state and the antiferromagnetic AFM-c, as a function of the distortion

Figure 4.8 shows the values of the total energies for the two configurations as a function of the distortion. Clearly phase AFM-there is always favoured, and structurally it is $Cmc2_1$.

Figure 4.9 shows the differences in energy between the ferromagnetic state and the antiferromagnetic AFM-c, as a function of the distortion. As a result, in the phase transition PE$\longrightarrow$FE the AF order is always favoured, but the FE distortion reduces the dominance of superexchange. In fact, during the transition the bonds angle $\mathrm{Mn}-\mathrm{O}-\mathrm{Mn}$ is reduced at least 20°.

In all the calculations only a collective mode displacement, δ, has been considered, in particular, for FE order δ =1.365 Å, whereas for AF order δ =1.228Å.

Estime of $\mathbf{T_N}$. The T_N has been estimated in accord with the Ising 3D AF model. The energy of a spin configuration is given by the Hamiltonian Function

$$\hat{H}_{spin} = -\sum_{<ij>} \mathtt{J}_{ij} S_i S_j$$

where $< ij >$ indicates that sites i and j are nearest neighbours. For any two adjacent sites i, j the interaction is J_{ij}, where the first sum is over pairs of adjacent spins (every pair is counted once). In the particular case of a cubic 3-dimensional isotropic lattice, that has a single coupling independent of direction, accurate simulations provide a temperature critical T_c in the coupling constant unit. The most precise value for the critical point of the 3D-Ising model has been obtained by Monte Carlo simulations [52]:

$$\lambda_c = \frac{\mathtt{J}}{T_c} \qquad \lambda_c = 4.51152 \tag{4.2}$$

with interaction energy J and critical temperature T_c. The temperature of Néel $T_N \equiv T_c$ can be determinated by knowledge of the J constant extracted from calculations of total energy. The J coupling has been determinated is J = 5 meV which corresponds to $T_N = 4.51\mathtt{J} \sim$270 K.

First-principle calculations have demonstrated that LMO presents an antiferromagnetic behaviour during the phase transition, then LMO is a multiferroic materials in that magnetic and ferrolectric orders coexist in the same phase. In the follow section I report the calculation of the spontaneous polarization to confirm the ferroelectrity.

4.2 Spontaneous Polarization

The macroscopic polarizability can be expressed as the sum of two contributions, one ionic and the other electronic

$$\Delta\mathbf{P} = \Delta\mathbf{P}_{\text{ion}} + \Delta\mathbf{P}_{\text{el}}$$

calculated using the theory of Berry phase, King-Smith and Vanderbilt, discussed in the Section 2.1 on page 28. The first contribution is obtained from:

$$\Delta\mathbf{P}_{\text{ion}} = \frac{|e|Z_\kappa u}{V}$$

while the second is to consider:

$$\Delta\mathbf{P}_e = \mathbf{P}_e^{\lambda_2} - \mathbf{P}_e^{\lambda_1}$$

where λ_1 identifies the high symmetry phase, paraelectric, while with λ_2 the ferroelectric phase.

4.2.1 Results and discussions

According to the Modern Theory of Polarization, discussed in the section 2.1, the calculation related to the electronic contribution to the polarization was carried out along each direction of the vector of the reciprocal lattice $\mathbf{G}_\parallel$, specifying the number J of k-points on the $\mathbf{k}_j = \mathbf{k}_\perp + j\mathbf{G}_\parallel/J$ mesh, with $j = 0, ..., J-1$. From calculation of spontaneous polarization for the most stable antiferromagnetic configuration, AFM-c, $\Delta\text{P}_{\text{Cmc2}_1-\text{Cmcm}} = 0.16688$ C/m^2 has been obtained. Figure 4.10 shows the trend of polarization as a function of the distortion.

The Berry-phase polarization, 17μC/cm^2, is somewhat but not significantly smaller than in LTO, 29μC/cm^2. This difference in polarization is related to the mode effective charge defined as:

$$\bar{Z}_{s\alpha} = \sum_{i\beta} Z^*_{i,\alpha\beta}\xi_{s,i\beta},$$

with $Z^*_{i,\alpha\beta}$ effective-charge tensor and $\xi_{s,i\beta}$ the vibrational mode, and the indices i, α and β, are relative to the atom considered and spatial directions, respectively. LTO collective distortion is decomposed in two main modes ξ_1, associated with the octahedra rotation (81 % of distortion), and ξ_2, associated with the deformation of octahedra (19 %). These modes are $\bar{Z}_{1,z}$=1.8 and $\bar{Z}_{2,z}$=12.0 respectively.

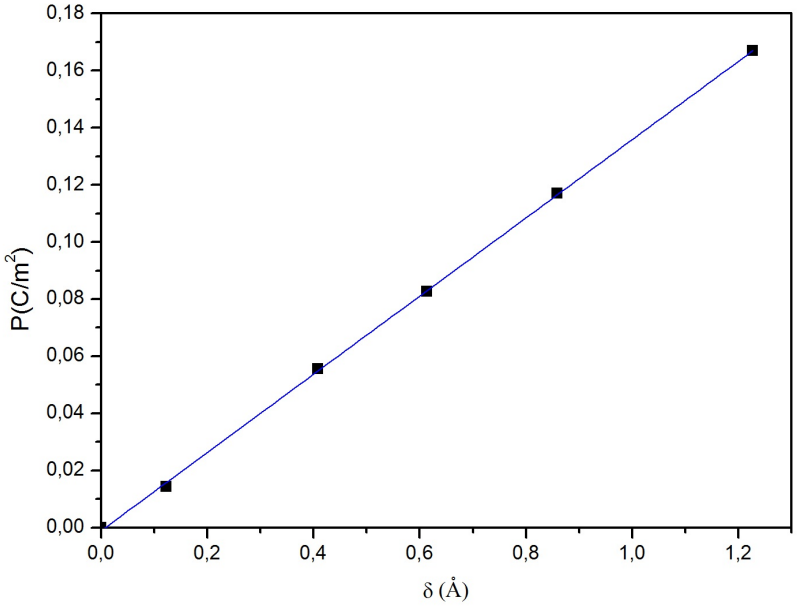

Figure 4.10: Computed distortion dependence of the polarization.

The sum of these contributions, appropriately weighing percentage, can be considered as a collective calculated tensor charge of totally $\bar{Z}^*$=3.73. The LMO has about the same polarization of LTO, less distortion, and then a charge of so composed largest, $\bar{Z}^*$=4.3, obtained considering the collectively mode ξ_1 and ξ_2. Consequently the value of 16.7 $\mu C/cm^2$ is comparable with the result obtained for LTO.

Figure 4.11, shows the energies of AF phase of LMO from *Cmcm* (PE) through $Cmc2_1$ (FE), and also depicts the polarization developing as the rotational displacements increase. Already at this level, there is evidence of magnetoelectricity: as the FE rotations are undone (as they would be, e.g., by an electric field), the FM-AF energy difference, hence the average magnetic coupling, doubles in intensity.

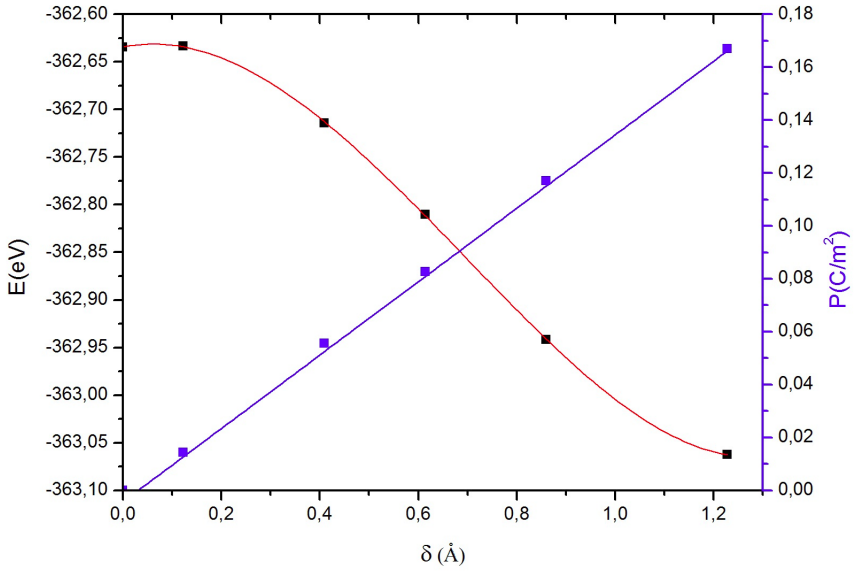

Figure 4.11: Computed distortion dependence of the polarization (blue) the total energy in the AF configuration (red) in $Cmcm \rightarrow Cmc2_1$ transition

CHAPTER 5

Magnetoelectric effect

The coupling between magnetic moment and ferroelectricity, or the ability of a magnetic moment to be produced by an externally applied electric field, or an electric moment to be produced by an externally applied magnetic field, is namely magnetoelectric effect. This magnetoelectric effect was predicted in 1894 by P. Curie [53], but it was first observed experimentally by Astrov [54] in a monocrystal of antiferromagnetic Cr_2O_2 in 1961. Firstly, it was formulated by L.D. Landau and E. Lifshitz [55] and later, in 1959, it was analytically described by I. Dzyaloshinskii [56], basing his theory on symmetry arguments and thermodynamics only. More recently, related studies on magnetic ferroelectrics have signalled a revival of interest in this phenomenon opening a new window of opportunities for application usage. Already, ideas of four-state memory, spintronics and magnetic field sensors are being under intense development [57–60]

5.1 Lattice-Mediated Magnetoelectric effect

The magnetoelectric effect, as electric and magnetic response of the system to a magnetic field and electric fields, respectively, is defined, in linear approximation, by the relations:

$$P_i = \alpha_{ij}\mathcal{H}_j$$
$$M_j = \alpha_{ij}\mathcal{E}_i$$

where P is the polarization, M is the magnetization, H, E are the magnetic and electric fields respectivly, the α is the *linear magnetoelectric tensor*. It is defined as $\alpha_{ij} \leqslant \sqrt{\chi^m_{ii}\chi^e_{jj}}$, where χ^m e χ^e are the magnetic and dielectric susceptibilities. It is related to simultaneous effect, spin-orbit magnetic component and the dielectric response, the last is due to changes in the structural and electronic state induced by the external electric field. I neglect the purely electronic response (fixed-ion) that would require calculations in finite electric field, but I focus on the terms products from the fields through the distortion of the structure, lattice-mediated response.

The energy of a linear magnetoelectric crystal is given by [61]

$$\begin{aligned} E(\{u_n\},\mathcal{E},\mathcal{H}) = E_0 &+ \frac{1}{2}\sum_{n=1}^{N_{IR}} C_n u_n^2 + \\ &- \Omega_0 \sum_i \mathcal{E}_i[\mathcal{P}_{latt,i(\{u_n\})} + \frac{1}{2}\sum_{i'} \chi^e_{ii'}\mathcal{E}_{i'}] \\ &- \Omega_0 \sum_j \mathcal{H}_j[\mathcal{M}_{latt,j(\{u_n\})} + \frac{1}{2}\sum_{j'} \chi^e_{jj'}\mathcal{H}_{j'}] \\ &- \Omega_0 \sum_{ij} \alpha_{ij}\mathcal{E}_i\mathcal{H}_j \end{aligned} \tag{5.1}$$

where u_n is the amplitude of a IR mode and C_n the corresponding eigenvalue. Then, the lattice contributions to polarization and magnetization are

$$\begin{aligned} \mathcal{P}_{\text{latt},i} &= \frac{1}{V}\sum_{n=1}^{N_{IR}} p^e_{ni} u_n \\ \mathcal{M}_{\text{latt},j} &= \frac{1}{V}\sum_{n=1}^{N_{IR}} p^m_{nj} u_n \\ u_n &= \frac{1}{C_n}\sum_i p^e_{ni}\mathcal{E}_i \end{aligned} \tag{5.2}$$

where p^e_{ni} is the polarization of the nth IR mode and p^m_{nj} is the magnetic analogue. Consequently

$$\alpha_{\text{latt},ij} = \sum_{n=1}^{N_{IR}} \frac{p^e_{ni}p^m_{nj}}{C_n} \tag{5.3}$$

5.1.1 Results and discussions

To quantify the linear magnetoelectric (ME) coupling, the lattice part of the ME tensor has been computed as the most likely dominant contribution defined

by eq. (5.3). To avoid a lengthy and expensive IR mode analysis, here only the collective displacement, connecting the FE and PE phases, has been considered. This is, of course, a superposition of several modes, so that we will obtain a global effect of the PE to FE transformation and not a mode-by-mode analysis.

To compute the magnetic response to lattice distorsions, non-collinear magnetic calculations including spin-orbit interaction, SOC, have been performed. In particular, I have used a different code for the treatment of non-collinear magnetic structures. This was written by David Hobbs, and spin-orbit coupling was implemented by Olivier Lebacq and Georg Kresse (for the formalism see 1.8).

Operationally, I have started performing a collinear calculations then, the fully non-collinear magnetic structure calculations have been performed replacing initial local magnetic moment for each ion in x, y and z direction respectively, finally I have included the spin-orbit coupling. The spin-orbit coupling works only for PAW potentials and is not supported for ultrasoft pseudopotentials. If spin-orbit coupling is not included, the energy does not depend on the direction of the magnetic moment, i.e. rotating all magnetic moments by the same angle results exactly in the same energy. Hence there is no need to define the spin quantization axis, as long as spin-orbit coupling is not included. Spin-orbit coupling, however, couples the spin to the crystal structure. In this framework, all magnetic moments are given with respect to the axis (s_x, s_y, s_z). To initialise calculations with the magnetic moment parallel to a chosen vector (x, y, z), it is therefore possible to either specify (assuming a single atom in the cell). By comparing the energies for different orientations the magnetic anisotropy can be determined.

	Total Energy(eV)	M (μ_B)
M. collinear	-363.06238	0
M. non-collinear	-363.05536	0
+ Spin-orbit	-365.39390	$m_x = 0.01 \div 0.12$
		$m_y = 0.53$
		$m_z = 0$

Table 5.1: Total energy and the density of the magnetization for the structure $Cmc2_1$ with the AFM-c configuration.

As shown in Table 5.1, the introduction of the spin-orbit lowers the total energy of about 2.34 eV. Interestingly, these calculations reveal that the collinear-AF Mn spins point along the c-axis, but with a slight canting towards the b-axis and an even smaller component along the a axis, with a resulting small net magnetic moment of 0.065 μ_B/Mn essentially parallel to b. In particular, the components along b-axis of magnetic moment for ion is about 0.12 μ_B refer to

Mn in proximity to layer, whereas is very little, about 0.01 μ_B for Mn inside the structure. Figure 5.1(a) highlights the inclination of the spins due to the spin-

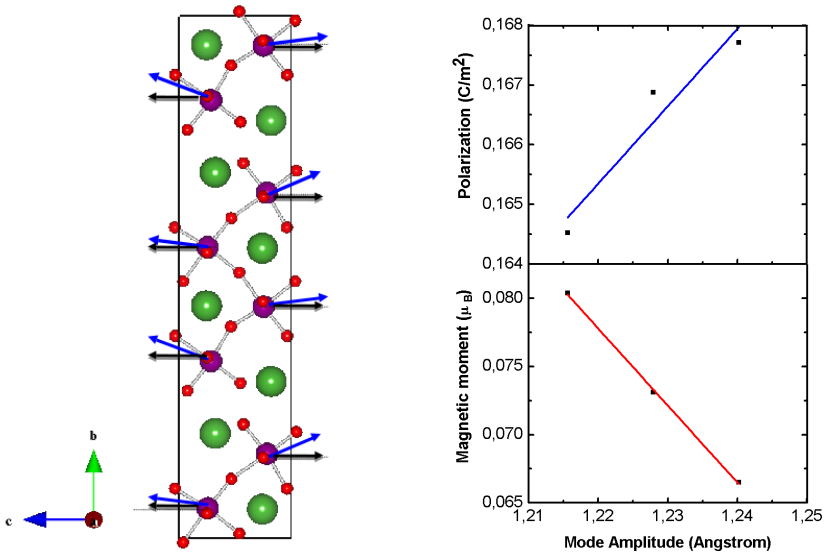

(a) (b)

Figure 5.1: (a) Spin canting due to the spin-orbit interaction. (b) Polarization and magnetization induced by the total distortion mode.

orbit interaction, while 5.1(b) shows polarization and magnetization calculated in function of the distortion, around the structure *Cmc2₁*.
Similarly, Benedek and Fennie obtained for $Ca_3Mn_2O_7$[1], CMO, a magnetization for Mn 0.04 μ_B(vs about 0.07 μ_B in LMO) [42]. This difference can be related to different distortion modes. Magnetoelectricity in CMO results by competition between rotation, tilt and polar distortion modes, even if, the canted moment is the results only by the rotation distortion.

Table 5.2 compares parameters entering the eq.(5.3) and the ME tensor for LMO and Cr_2O_3[2] (as computed in [61]). The final ME coefficient is much larger in LMO, and results from the larger magnetic response to lattice distortions and the much softer force constant of the predominantly rotational collective mode, and similar polarization responses. α is in Gaussian unit [62] [3].

[1]CMO structure belongs to Ruddlesden-Popper perovskite family with genetal formula $A_{n+1}B_nO_{3n+1}$. Any given member of the Ruddlesden-Popper series consists of ABO_3 perovskite blocks stacked along the [001] direction with an extra AO sheet inserted every n perovskite unit cells. In CMO n=2.

[2]Data related to Cr_2O_3 structure are listed in Appendix C

[3]α is calculate SI-Unit, which can be converted to the practical units by $\mu_0 = 4\pi \times 10^{-7}$Vs/(Am) and $c = 3 \times 10^8$m/s, in this way you get a dimensionless quantity in Gaussians units.

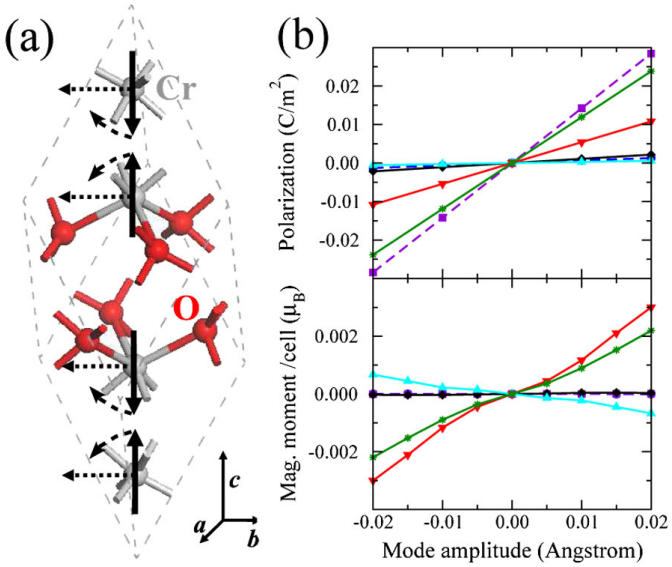

Figure 5.2: (a) Primitive cell of the Cr_2O_3. The arrows represent the antiferromagnetic spin alignment, while the dotted arrows show the effect of the spin-orbit. (b) Variation of polarization and magnetization induced by IR modes, A_{2u} (dotted line) and E_u (line) as a function of the amplitude of the modes. Ref. [61].

	$La_2Ti_2O_7$	Cr_2O_3
C_n (eV/ Å^2)	3.8	10.4 ÷ 32.5
p_n^d ($\|e\|$)	4.3	0.16 ÷ 8.52
$p_n^m(10^{-2})$ (μ_B/Å)	66.0	0.02 ÷ 11.32
$\alpha_n(10^{-4}$g.u.)	48.9	-0.01 ÷ 0.68

Table 5.2: Parameters of the eq.(5.3) and ME tensor coefficient for the non-zero component α_{zy} in LMO compared with the range of value obtained by Iniguez for Cr_2O_3 for the individual IR modes.

By symmetry, the ME tensor is off-diagonal in LMO.

$$\alpha = \begin{pmatrix} 0 & 0 & 0 \\ 0 & 0 & \alpha_{zy} \\ 0 & \alpha_{yz} & 0 \end{pmatrix}$$

Since $Cmc2_1$ belongs to magnetic group $F_c m' m2$, the magnetoelectric tensor is non-diagonal with two components α_{yz} and α_{zy} [63]. In this case only one independent component survives, α_{yz}, then result in a cross-field response M_y=αE_z. To be more precise, an electric field E_z could produce a magnetization variation $M_y = \alpha_{zy} E_z$. Similarly, a polarization change $P_z = \alpha_{zy} H_y$ could be produced by a magnetic field H_y.

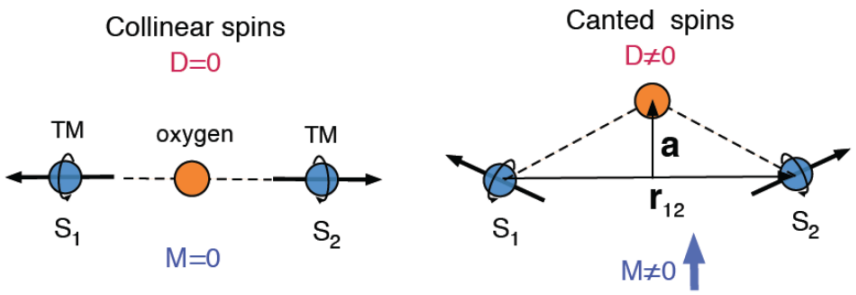

Figure 5.3: Canting of magnetic moments and a resulting net magnetization M$\neq$ 0 in an otherwise collinear antiferromagnet. The Dzyaloshinskii-Moriya (DM) interaction is an antisymmetric, anisotropic exchange coupling $H_{DM} = \mathbf{D}_{12} \cdot \mathbf{S}_1 \times \mathbf{S}_2$ between two spins $\mathbf{S}_1$ and $\mathbf{S}_2$ separated by a lattice bond $\mathbf{r}_{12}$ with no inversion center, i.e. $\mathbf{D}_{12} \sim \lambda \mathbf{a} \times \mathbf{r}_{12}$. The Dzyaloshinskii-Moriya vector $\mathbf{D}$ is proportional to a spin-orbit coupling constant λ, and depends on the position of the oxygen ion between two magnetic transition metal ions. Ref. [66]

5.2 Dzyaloshinskii-Moriya coupling

Dzyaloshinskii and Moriya have explained the weak ferromagnetism, that it is observed in several antiferromagnetic insulating compounds, on the basis of Landau's theory of phase transitions of the second kind. They have shown that "weak" ferromagnetism is due to relativistic spin-lattice interaction and magnetic dipole interaction [64,65]. The weak ferromagnetism in LMO can be interpretated by Dzyaloshinskii-Moriya (DM) interaction. This is an other term in the spin-spin interaction manly associated to the crystal symmetry. For this reason there is a relationship between the oxygen-octahedra rotations, the ferroelectricity and the week ferromagnetism, wFM, in other terms, the wFM is due to the DM interaction induced by the oxygen-octahedra rotations.

Formally, the Hamiltonian function for spin-spin interaction can be written as [67]

$$\mathbf{H}_{\text{spin}} = \frac{1}{2} \sum_{i,j} \mathbf{s}_i \mathcal{J}_{ij} \mathbf{s}_j$$

where $\mathcal{J}_{ij}$ is decomposed in

$$\mathcal{J}_{ij} = \mathrm{J}_{ij} I_3 + \mathcal{J}^S_{ij} + \mathcal{J}^A_{ij}$$

where I_3 is the unit matrix and:

$$\begin{aligned} \mathrm{J}_{ij} &= \frac{1}{3} Tr(\mathcal{J}_{ij}) \\ \mathcal{J}^S_{ij} &= \frac{1}{2}(\mathcal{J}_{ij} + \mathcal{J}^t_{ij}) - \mathrm{J}_{ij} I_3 \\ \mathcal{J}^A_{ij} &= \frac{1}{2}(\mathcal{J}_{ij} - \mathcal{J}^t_{ij}) \end{aligned} \tag{5.4}$$

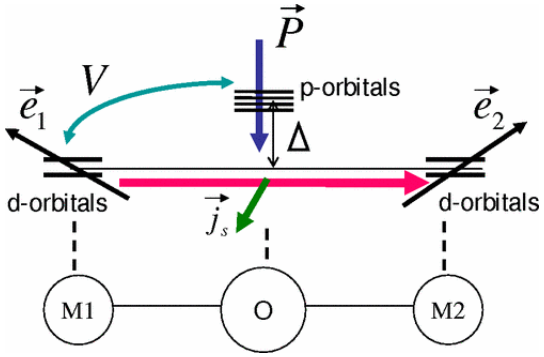

Figure 5.4: The cluster model with two transition metal ions M_1, M_2 with the oxygen atom, O, between them. With the noncollinear spin directions $\bar{e}_1$ and $\bar{e}_2$, there arise the spin current $\bar{j}_s \propto \bar{e}_1 \times \bar{e}_2$ between M_1 and M_2. Here the direction of the vector $\bar{j}_s$ (denoted by the short arrow near the middle of the diagram) is that of the spin polarization carried by the spin current. The direction of the electric polarization $\bar{P}$ is given by $\bar{P} \propto \bar{e}_{12} \times \bar{j}_s$ where $\bar{e}_{12}$ is the unit vector connecting M_1 and M_2. Ref. [68].

in which t denotes transposed matrices. Then, according to Moriya [65] a typical intersite interaction consists of the following terms:

$$\mathbf{s}_i \mathcal{J}_{ij} \mathbf{s}_j = \mathrm{J}_{ij} \mathbf{s}_i \cdot \mathbf{s}_j + \mathbf{s}_i \mathcal{J}^S_{ij} \mathbf{s}_j + \mathbf{D}_{ij}(\mathbf{s}_i \times \mathbf{s}_j)$$

where the first and second terms on the rights are the isotropic and the symmetric anisotropic exchange interactions, respectively, while the third term represents the DM interactions with the DM-vectors $\mathbf{D}_{ij}$ being defined as:

$$D^x_{ij} = \frac{1}{2}(\mathrm{J}^{yz}_{ij} - \mathrm{J}^{zy}_{ij}) \qquad D^y_{ij} = \frac{1}{2}(\mathrm{J}^{xz}_{ij} - \mathrm{J}^{zx}_{ij}) \qquad D^z_{ij} = \frac{1}{2}(\mathrm{J}^{xy}_{ij} - \mathrm{J}^{yx}_{ij})$$

Moreover, according to Katsura, Nagaosa and Balatsky, the direction of electric polarization is given by:

$$\mathbf{P} \simeq \mathbf{r}_{ij} \times [\mathbf{e}_i \times \mathbf{e}_j]$$

where $\mathbf{e_i}$, $\mathbf{e_j}$ are the noncollinear spin directions of the transition metal ions and $\mathbf{r}_{ij}$ is the bond direction [68].

5.2.1 Results and discussions

Spin-orbit coupling (SOC) has been included in non-collinear calculations. Comparing non-collinear results for canted and non-canted Mn spins, I obtain directly

$$\delta \mathrm{M_{DM}} = (0, 62.5, 0)\mathrm{m}\mu_\mathrm{B}/\mathrm{Mn} \qquad \delta \mathrm{E_{DM}} = 0.1\mathrm{meV} \qquad \delta \mathrm{P_{DM}} = (1, 1, -2)\mu\mathrm{C/m}^2$$

Clearly the FM moment, energy gain, and induced polarization are all very small (although computationally measurable); in fact, they result from small components acquired by Mn spins along the a and b axes (besides the c axis) due to SOC. The energy gain and induced polarization are indeed

$$\delta \mathrm{M}_{\mathrm{DM}} \simeq \sum \mathbf{D}_{ij} \cdot [\mathbf{e}_i \times \mathbf{e}_j] \qquad \delta \mathrm{P}_{\mathrm{DM}} \simeq \sum \mathbf{r}_{ij} \times [\mathbf{e}_i \times \mathbf{e}_j]$$

where the $\mathbf{e}_i$ are spin directions, $\mathbf{r}_{ij}$ vectors connecting spin locations, $\mathbf{D}$ the Dzyaloshinskii-Moriya coupling ($D \perp r_{ij}$), and the sums are over spin pairs.

In conclusion, the wFM tends to enhance the polarization, otherwise the spins of each pair were in the same plane, the induced polarization and energy gain would vanish.

Conclusions

In summary, I found that LMO is a topological multiferroic with large magnetoelectric response. LMO's ferroelectricity results from its layered structure, producing dipoles from rotations instead of off-centering displacements. The polarization is P=$(0, 0, P_s)$ with P_s =0.17 C/m^2, comparable to displacive FE's. I estimated the T_C about 1500 K.

LMO is in essence a high Neél temperature, T_N=270 K, approximately *G*-type antiferromagnet, as expected from superexchange between Mn^{4+} ions; however, Mn AF-ordered spins are canted due to spin-orbit coupling, giving rise to weak ferromagnetism and small off-polar axis polarization.

LMO's off-diagonal lattice magnetoelectric tensor couples M(P) to orthogonal electric (magnetic) fields, and notably, due to softer force constants and large magnetization sensitivity to ionic motion, it is about 50-fold that of the prototypical magnetoelectric Cr_2O_3.

Part II

Properties of $(Ga_{1-x}In_x)_2O_3$ solid solutions

This Part is devoted to the investigation of $(Ga_{1-x}In_x)_2O_3$ alloys. Alloying Ga_2O_3 with In_2O_3 offers an opportunity to tune the band gap and heterostructures enable electronic and optical confinement. The first part of the following discussion is published in the "Journal of Physics: Conference Series, 566(1):012016, 2014" that principally summarizes the electronic properties of Ga_2O_3 in the β phase and introduces alloys with In at low concentration. Progress in the alloying at low In concentration, for example, the determination of solubility limit, are summarized in the "Applied Physics Express, 8(2):021102, 2015". Furthermore, the characterization of $(Ga_{1-x}In_x)_2O_3$ alloys in the overall x-range and band offset at interfaces are described in the "Journal of Physics: Condensed Matter, in print (2015)" Finally, a new paper, that contains the revised phase diagram and the polarization of new stable and meta-stable phases of $(Ga_{1-x}In_x)_2O_3$, is submitted.

Introduction

Compound semiconductor systems based on the group III-oxides such as gallium oxide (Ga_2O_3), aluminium oxide, (Al_2O_3), and indium oxide, (In_2O_3), have been the pioneer for new semiconductor device technologies. In fact, these transparent conducting oxides, TCOs, are used in a variety of applications including flat panel displays and solar energy conversion devices. Among these, Ga_2O_3 is attracting interest recently as a material for high-power transport and ultraviolet optical absorbers, owing to its wider band gap and larger electric breakdown voltage compared to e.g. GaN. The bandgap of β-Ga_2O_3 is 4.6–4.9 eV, which corresponds to the second largest bandgap after that of diamond among semiconductors. Recently, Ga_2O_3 have had some attempts to develop optical devices such as deep ultraviolet photo detectors [69, 70] and GaN-based blue light emitting diodes, [71] using Ga_2O_3 epitaxial layers and substrates mainly by making the best use of its transparency [72, 73].

Combined with In_2O_3 (already widely used as Transparent Conducting Oxide, TCO), Ga_2O_3 originates a new materials system which is tunably insulating, easily n-doped (not so easily p-doped), and potentially magnetic (as In_2O_3 can be made ferromagnetic [74] through magnetic doping, the same may well apply to Ga_2O_3). A natural development that can be envisaged is the growth of a solid solution $(Ga_{1-x}In_x)_2O_3$, typically (though not necessarily) epitaxially on the parent compounds; this would enable one a) to combine and tune the functionalities of the two parent compounds, and b) to export the band-engineering and nanostruc-

turation concepts well known in other semiconductor systems (such as arsenides and nitrides) to much higher absorption energies and breakdown voltages.

Phase relationships in the Ga_2O_3-In_2O_3 system have been previously studied with somewhat conflicting results. Investigations of the phase diagram of the system Ga_2O_3–In_2O_3 have shown the existence of a solid solution over a wide composition range extending up to $x \approx 0.42$ [75]. Firstly, Goldschmidt *et al.* [76] proposed a phase diagram which included solid solution with β-gallia, cubic and corundum-like structures (α-alumina). Based on structural considerations and lattice parameter measurements Shannon and Prewitt [77] proposed that In replaces all of the octahedrally coordinated Ga cation to form β-Ga_2O_3, Schneider *et al.* [78] and MacDonald *et al.* [79] reported the formation of unknown product(s) in the intermediate composition Ga_2O_3–In_2O_3 and confirm those of Goldschmidt.

Further, the band-engineering and nanostructuration concepts from popular semiconductor systems such as, e.g., AlGaAs or InGaN may be exported to these materials, and thus to a whole new region of high absorption energies and breakdown voltages. This may enable the design of devices based on $Ga_2O_3/(Ga_{1-x}In_x)_2O_3$ such as high-power field effect transistors and far-UV photodetectors or emitters.

CHAPTER 6

Gallium and Indium Oxides. Structure and electronic properties

6.1 Gallium Oxide

Gallium oxide, Ga_2O_3, exists in various polymorphs. In Table 6.1 I have reported the polymorphs identified in 1952 by Roy *et al.* [80] from powder X-ray diffraction techniques. These different phases are analogous to other binary oxides such as Al_2O_3 and Fe_2O_3. Despite that the crystal structure of ε-Ga_2O_3 was not able to be determined.

name	type	space group	(No)
α	corundum	$R\bar{3}c$	(161)
β	monoclinic	$C2/m$	(12)
γ	cubic spinel	$Fd\bar{3}m$	(227)
δ	bixbyite	$Ia\bar{3}$	(206)
ε	orthorhombic	$Pna2_1$	(33)

Table 6.1: Different polymorphs of Ga_2O_3. The type and the space group of these structures are specified.

Among them, the most stable phase is the monoclinic β-Ga_2O_3 at ambient condition [81]. As shown in Figure 6.1, the unit cell contains 20 atoms, with two crystallographically nonequivalent Ga atoms in tetrahedral and octahedral like coordinations in the lattice.

$C2/m$ (No. 12)	a = 12.46241 Å	b = 3.08801Å $\alpha = \gamma = 90°$,	c = 5.87998Å $\beta = 103.66°$	
Atom	**x**	**y**	**z**	**Wyc**
Ga1	0.09003	0.00000	0.79490	4i
Ga2	0.34149	0.00000	0.68562	4i
O1	0.16395	0.00000	0.10930	4i
O2	0.49601	0.00000	0.25609	4i
O3	0.82657	0.00000	0.43649	4i

Table 6.2: Structure parameters of β-Ga_2O_3 in the monoclinic phase, it has Z=4 formula units per crystallographic cell.

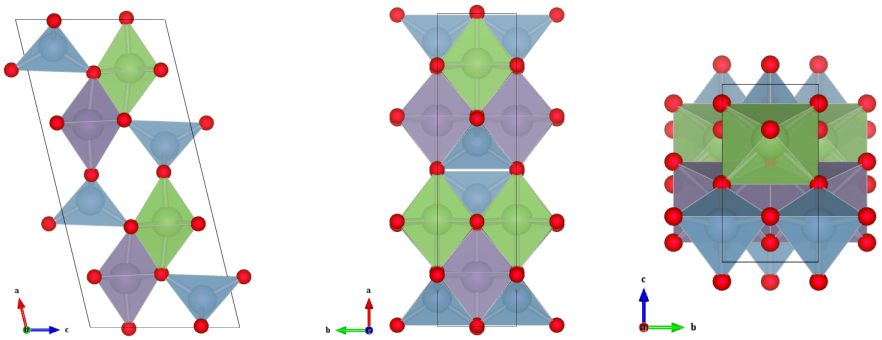

Figure 6.1: Different views of the monoclinic phase of Ga_2O_3. The structure of β-Ga_2O_3 can be seen as a collection of zigzag double chains of edge-sharing GaO_6 units (violet and green Ga-octahedra) linked by single chains of vertex-sharing GaO_4 (blue Ga-tetrahedra).

Structure optimization. Geometry and volume optimizations as well as electronic structure calculations have been performed using density functional theory (DFT) in the generalized gradient approximation (GGA), and the PAW method as implemented in the VASP code [5]. The **k**-point meshes of Brillouin zone sampling for the primitive cells, based on the Monkhorst–Pack scheme were set at 4×8×6. The cutoff energy has been set at 470.9 eV. The equilibrium structure are obtained after cell geometry and volume fully relaxation. The calculated lattice parameters compare well with experimental data [82], reported in parenthesis: a=12.46 (12.23)Å, b=3.08 (3.04)Å, c=5.88 (5.80)Å, θ=103.65 (103.7)°, fractional coordinates are listed in Table 6.2.

Electronic properties of β-Ga_2O_3. The energy band structure of β phase, shown in Figure 6.2(a), similarly to other binary Ga compounds, has mainly O $2p$ character in the upper valence band and Ga s content in the bottom conduction band, as dispayed in Figures 6.2(b) and 6.2(c). The Fermi energy is set at the zero point of the energy scale. The direct gap appears at the Γ point. The calculated band gap is smaller than the experimental results, in fact GGA underestimates it at about 2 eV, as expected of semilocal functionals. Adding an empirical self-

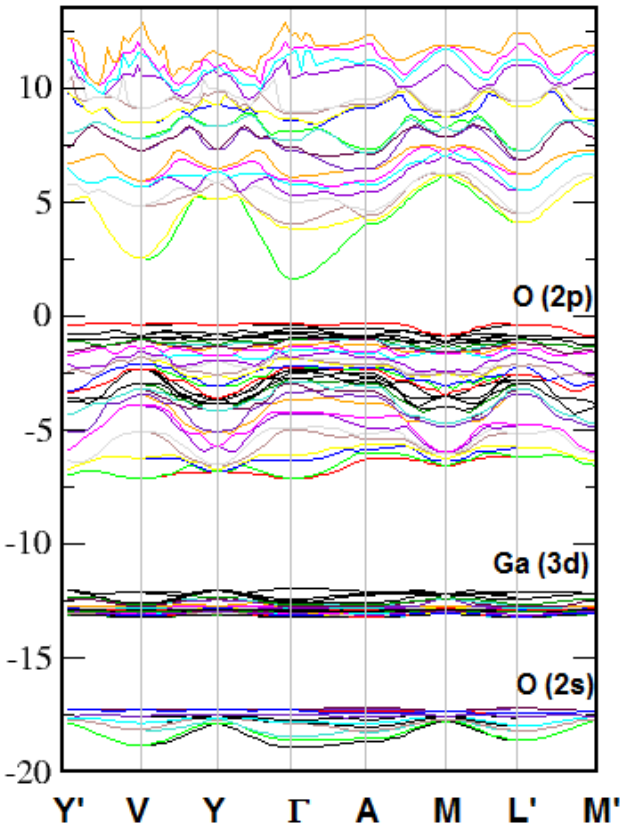

(a) Band structure of monoclinic Ga_2O_3. The **k** points are Y' = $(\frac{1}{2}\,\frac{1}{2}\,0)$, V= $(\frac{1}{2}\,0\,0)$, Y= $(0\,\frac{1}{2}\,0)$, Γ = $(0\,0\,0)$, A= $(00\frac{1}{2})$, M= $(0\frac{1}{2}\,\frac{1}{2}0)$, L'= $(\frac{1}{2}0\frac{1}{2}0)$, M'= $(0\frac{1}{2}\,\frac{1}{2}\,\frac{1}{2})$.

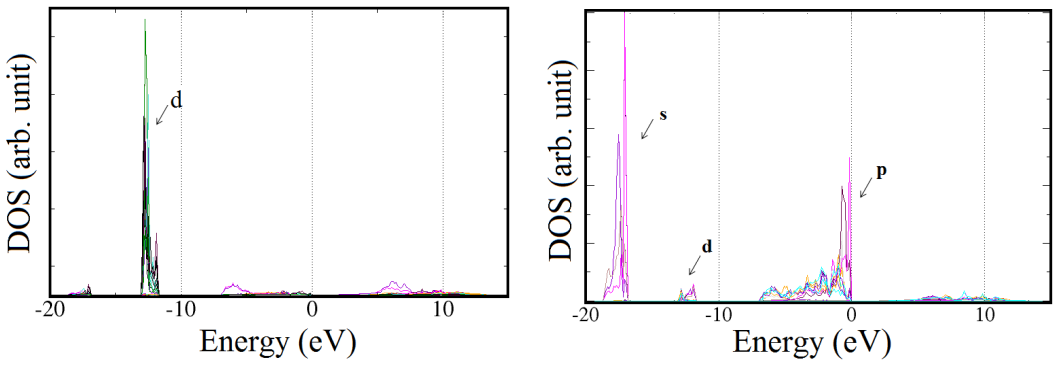

(b) Projected DOS of Ga

(c) Projected DOS of O

Figure 6.2: Band structure and projected density of states of β-Ga_2O_3

energy correction [83] involving the high-frequency dielectric constant[1], I have obtained a gap of 4.2 eV, not far from the experimental range of 4.5÷5 eV.

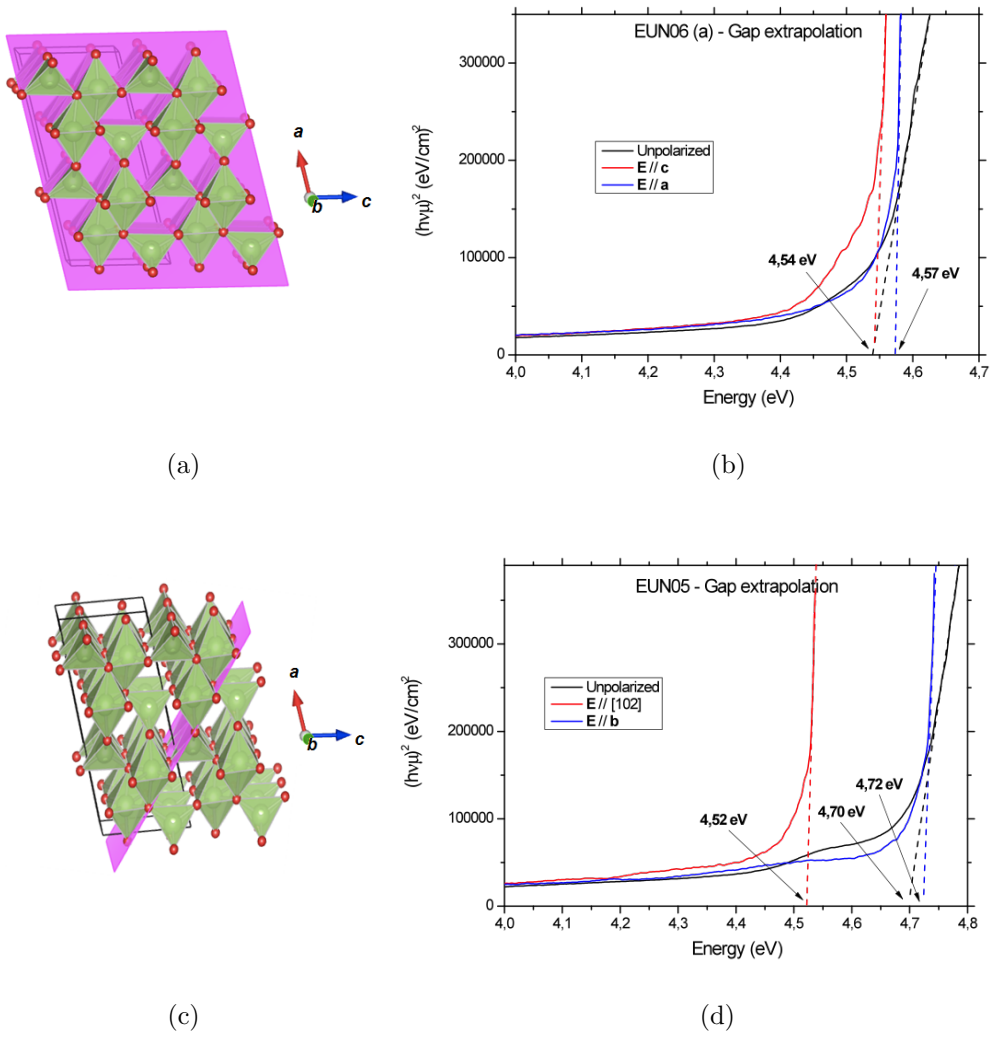

Figure 6.3: Absorption spectra of β-Ga_2O_3 at normal incidence on the (010) surface with polarizations $\mathbf{E}\|\mathbf{c}$ and $\mathbf{E}\|\mathbf{a}$. Absorption spectra of a (-201) wafer orientation.

Surprisingly, the precise value of the gap is still uncertain even in recent work [84]. The reason for this is probably the significant anisotropy of the absorption bandgap, which has been analysed with computational techniques and experimental methods [85]. Ab initio calculations are performed using hybrid functionals, HSE [86], and variational pseudo self-interaction corrections, VPSIC [87, 88] (known to be free of the typical LDA/GGA gap errors). Polarized absorption experimentally measured are reported in Figure 6.3.

[1]This correction shifts the value of the gap by an amount equal to $\Delta = \alpha/\varepsilon$ where α is a constant, ~ 9 eV, and ε is the high-frequency dielectric constant.

The bandgap edge is seen to be a function of light polarization and crystal orientation, with the lowest onset occurring at polarization in the *ac* crystal plane around 4.5-4.6 eV; polarization along *b*-axes unambiguously shifts the onset up by 0.2 eV, it is the direct evidence for anisotropy. Figure 6.4 shows the three

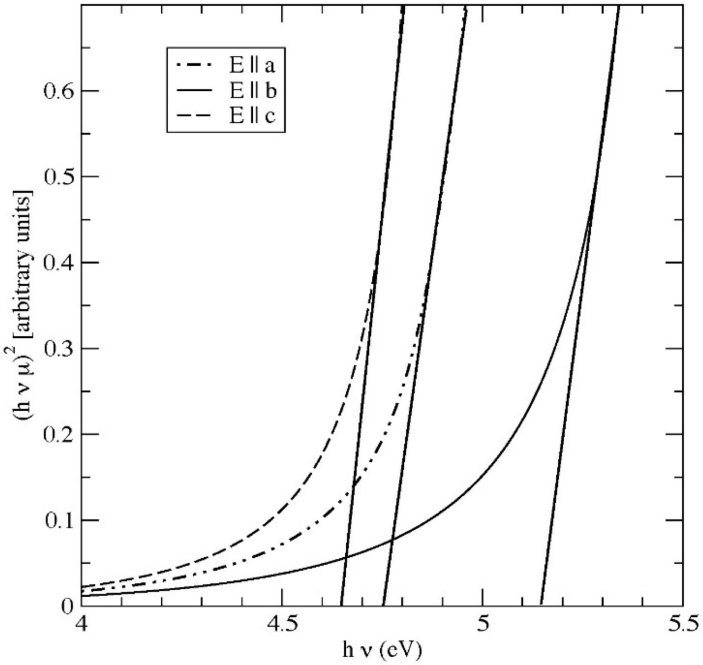

Figure 6.4: Tauc plot of the absorption coefficient, showing the polarization dependent onsets. Ref. [85].

theoretical distinct absorption edges as a function of polarization, the band gap obtained with electric field vector **E** polarized along the crystallographic *b*-axes, **E**∥**b**, is higher than other orientations, **E**∥**c** and **E**∥**a**. Theoretical results reproduce well the sequence of the bandgap edges of experimental one although the theoretical gap value is systematically higher than experimental results. This error is justified from choice of theoretical method, in fact, gaps can be overstimates in PSIC calculations. Figure 6.5 provides an example in support of this explanation.

In this figure, the direct gap, obtained by different computational methods as a function of the crystal cell volume, is reported [85]. Predicted crystal cell volume is clearly different in every set of data, and the difference of the calculated gap using PSIC method or hybrid functional are also evident. On the other hand, these advanced methods confirm a direct minimum gap at zone center between 4.2 eV (hybrids) and 4.7 eV (self-interaction-correction). Furthermore, the pressure derivative of the gap results to be 3 meV/kbar essentially as in GGA (see later) and in agreement with experimental results [84].

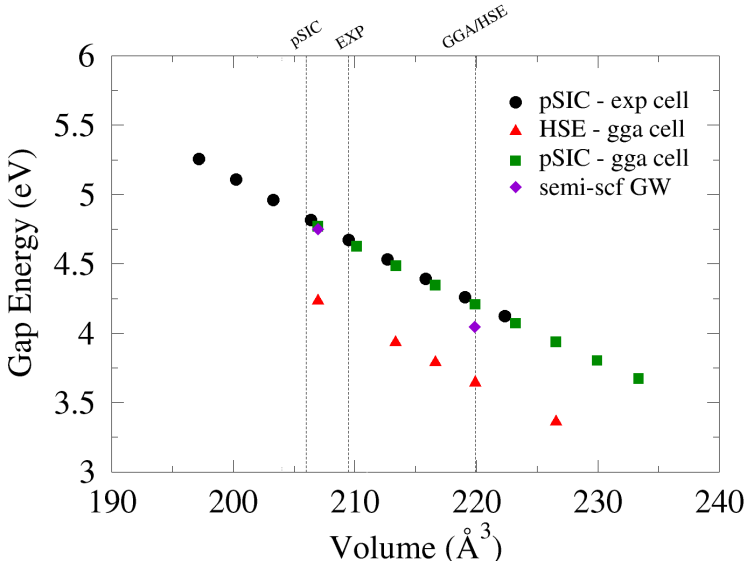

Figure 6.5: Gap vs volume as obtained from hybrid and self-interaction corrected functionals, as well as from GW_0 many-body perturbation theory. The line EXP marks the cell volume obtained from experimental lattice parameters. Ref. [85].

6.2 Indium Oxide

Indium oxide is used in batteries, transparent thin film infra-red reflectors. It is also commonly doped with tin oxide (SnO_2) to make indium tin oxide (ITO), which is used in transparent conductive thin films, that are used in various different types of displays, energy efficient windows and photovoltaics [89–92]. In this material, the nature of the band gap is remained contentious [93] for decades, only recently it is resolved from a joint experimental and theoretical effort [94]. The direct electronic band gap of the bulk material is of the order of 2.9 eV, and the large disparity between the electronic and optical band gaps ($E_g$opt $\sim$ 3.6 eV) arises from a combination of dipole forbidden optical transitions and conduction band occupation.

In_2O_3 is a candidate to realize the bandgap engineering of Ga_2O_3, since both indium and gallium belonging to the same elements group, have similar electron structures. In_2O_3 exists in three different phases characterized by space group symmetries: two body-centered cubic $I2_13$ and bixbyite-type $Ia\bar{3}$, and a rhombohedral corundum-type $R\bar{3}c$ [95]. In addition, two new high-pressure metastable phases were discovered: the orthorhombic *Pbcn* and *Pnma* [96].

Among these phases the most studied is the $Ia\bar{3}$ one [97]. This phase crystallizes in a body-centered cubic, bixbyite. The structure contains Z=8 formula units per crystallographic cell, where each In atom occupy two nonequivalent sites

and is coordinated by six oxygen atoms in a distorted octahedron, as shown in Figure 6.6.

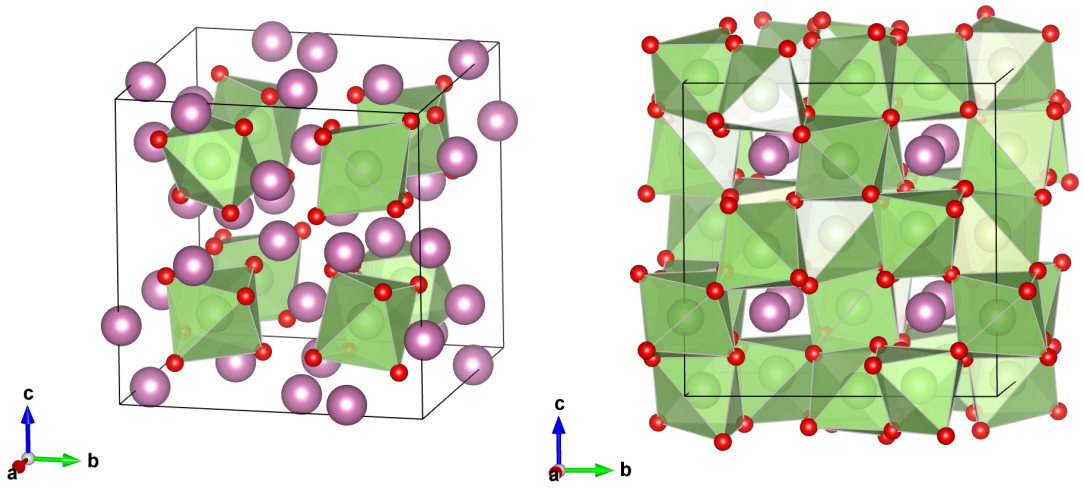

Figure 6.6: The bixbyite structure (group T_h) has six-fold coordinated cations occupying 8*b* high-symmetry and 24*d* Wyckoff sites. The 8*b* sites are highlighted by the local oxygen octahedra in the left panel, the 24*d* in the right one.

Structural optimization. The structural optimization are obtained using the same method of Ga_2O_3, in this case the bulk Brillouin zone is sampled on a 2×2×2 Monkhorst-Pack grid and the cutoff energy is set at 450 eV. The equilibrium lattice parameters and internal coordinates are listed in Table 6.3.

	$Ia\bar{3}$ (No. 206)	a = b = c 10.29108Å	$\alpha = \beta = \gamma$ 90°	
Atom	**x**	**y**	**z**	**Wyc**
In1	0.25000	0.25000	0.25000	8b
In2	0.46622	0.00000	0.25000	24d
O	0.38974	0.15453	0.38234	48e

Table 6.3: Computed structure parameters of In_2O_3 in the $Ia\bar{3}$ phase.

Electronic properties of In_2O_3. The calculated band gap is smaller than the experimental results also in the case of In_2O_3. I have obtained a gap of 0.933 eV, but, including the empirical self-energy correction ($\Delta = 9\text{eV}/\varepsilon$)[2] the value increses to 2.808eV, in decent agreement with 2.9 eV.

[2] I have considered the electronic dielectric constant of In_2O_3 calculated by Varley and Schleife, $\varepsilon = 4.80$ [98].

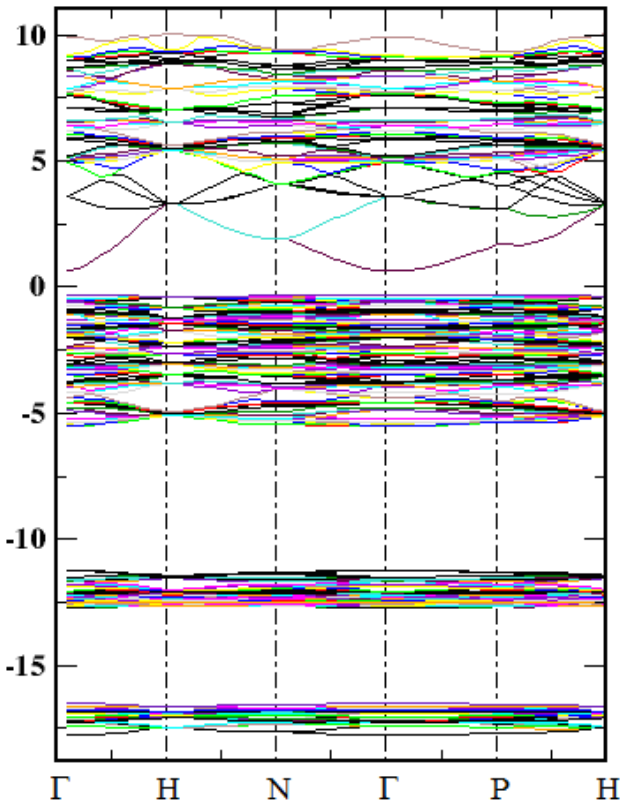

Figure 6.7: Band structure ob bixbyite In_2O_3. The **k**-points are: $\Gamma = (0\,0\,0)$; H= $(\frac{1}{2}\ -\frac{1}{2}\ \frac{1}{2})$; N= $(0\,0\,\frac{1}{2})$; $\Gamma = (0\,0\,0)$; P= $(\frac{1}{4}\ \frac{1}{4}\ \frac{1}{4})$; H= $(\frac{1}{2}\ -\frac{1}{2}\ \frac{1}{2})$.

6.3 $(Ga_{1-x}In_x)_2O_3$ alloys

Since unalloyed In and Ga oxides have different structures (bixbyite and monoclinic β, respectively) the high-In and low-In-content alloying limits will behave quite differently, and at intermediate concentrations the two phases are likely to mix in an complicated way. The experimental alloying of Ga_2O_3 with In_2O_3 exhibits significant limitations, with β-Ga_2O_3-like and bixbyite-like X-ray spectra at low x and high x respectively, and a mixed-phase region at midrange x. In particular, the β-Ga_2O_3-like phase persists only up to about 15% or so [84]. Thus, keeping in mind that the large-x end of the alloying spectrum will have to be treated differently, here I consider the low-x end substituting In for Ga in β-Ga_2O_3 at nominal concentrations of 3, 6, 9, and 12 % (one to four In atoms per 80-atom or 32-cation supercell).

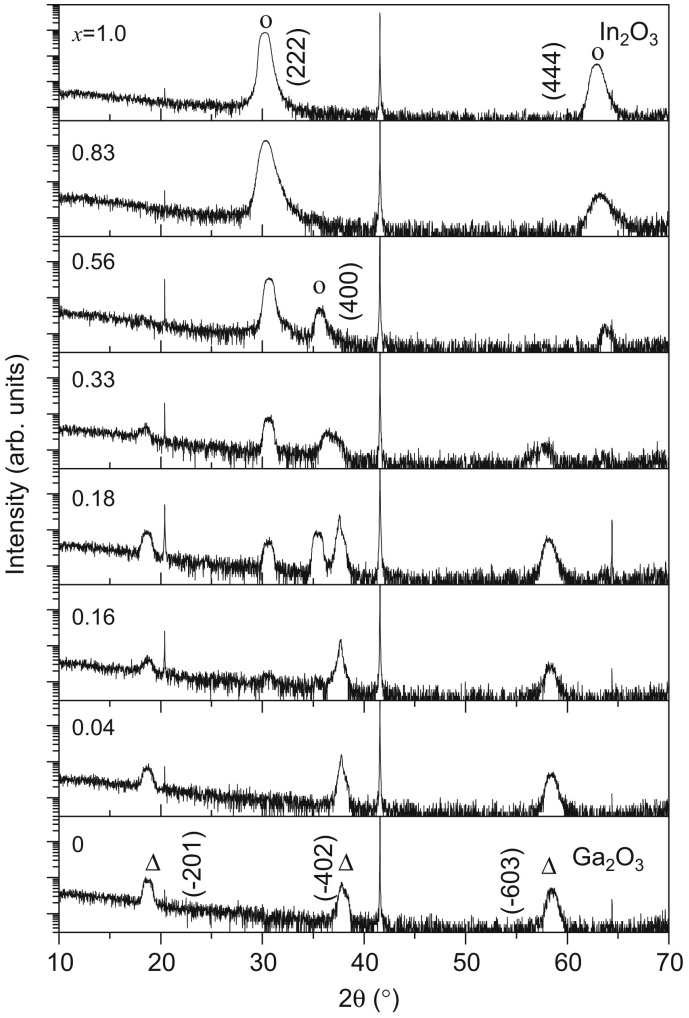

Figure 6.8: XRD patterns of $(Ga_xIn_{1-x})_2O_3$ films with different indium contents (x) deposited on (0001) sapphire substrates at substrate temperature of 500°C. Peaks marked by triangle belong to monoclinic structure while that marked by circle belong to cubic structure. Peaks not assigned belong to the sapphire substrate. Ref. [84].

6.3.1 Low-x $(Ga_{1-x}In_x)_2O_3$ alloys

Different atomic arrangements, in 80-atom supercells by 1×2×2 expansion of the primitive cell of the normal monoclinic structure, have been construited. In particular, supercells of Ga_2O_3 with In→Ga substitutions was sampled some of the various possible octahedral and tetrahedral sites and combinations thereof as function of composition (i.e. In concentration). I have optimized (in volume, shape, and internal coordinates) supercells with a 2×4×2 **k**-point grid. The calculations at 3% In (one "isolated" In atom per 80-atom cell) show that In only substitutes octahedral Ga: tetrahedral sites are ruled out by a huge excess energy cost of 1.1 eV. Therefore, half the cation sites are essentially inaccessible to In, and hence the amount of In that can actually be incorporated into Ga oxide is

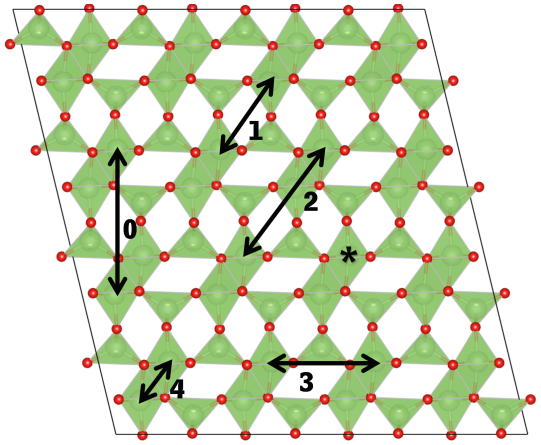

Figure 6.9: Different pairings patterns of 6% In-content in β-Ga_2O_3.

6% In-content						
Patern	0	1	2	3	4	*
ΔE(meV)	0	16	50	100	125	250

Table 6.4: The energy of structure with 6% In-content in different configurations, in β-Ga_2O_3 phase. Every In occupies octahedral site

automatically halved – to put it differently, all available sites would be occupied already at 50% nominal In content.

Even reaching this limit, though, is quite unlikely. Indeed, In incorporation is not arbitrary in terms of configuration. At 6% In-content, i.e two In atoms per supercell, it is possible estimate the energetics of pairing (or, rather, non-pairing) of In in Ga_2O_3. Figure 6.9 displays the preferential couplings. The energy of configuration '0' is chosen as zero; the structures numbered '1' to '4' are in progressively unfavourable energetic order, with '1' at 16 meV, '2' at 50 meV, '3' at 100 meV, '4' at 125 meV. In the configuration labeled '*', In atoms occupy adjacent octahedra; this structure is 250 meV higher than the reference.

Clearly, In atoms tend to avoid one another, and it is likely that at the common growth temperatures of 850 K the typical configurations will be such as our '0' and '1', described above. Analysing the structure, this suggests that well below a half, and probably closer to a quarter, of the octahedral sites can be occupied by In with a reasonable energy cost; when these are filled, the formation of some mixed β/bixbyite phase may be preferable to substitution in the β phase. This brings the effective solubility in the original β-Ga_2O_3 structure down to between 12% and 25% as found in experiment [84].

Consistently with the above configurational restrictions on pairing, the admissible arrangements at 9% and especially 12% In content are few. The resulting structures are probably a fairly decent model of the alloy, given the very limited configurational freedom of In already at these concentrations. (Cluster-expansion work is ongoing on miscibility at finite temperature and will be reported in the next section.)

I have chosen as dilute limit the concentration of 3% In, i.e. one "isolated" In atom per 80-atom cell. Besides being computational feasible, 3% is actually a quantitatively accurate dilute limit: the formation energy calculated in the standard way [99] is $E_f(1)$=0.24 eV/In, which yields a concentration of 2.7% at the typical growth temperature T_g=775÷800 K [84, 100]. The chemical-potential reservoir for In is the bixbyite phase of In_2O_3, which might occur in nanograins embedded in Ga_2O_3. Indium substitution at tetrahedral sites costs δE_t=1.1 eV

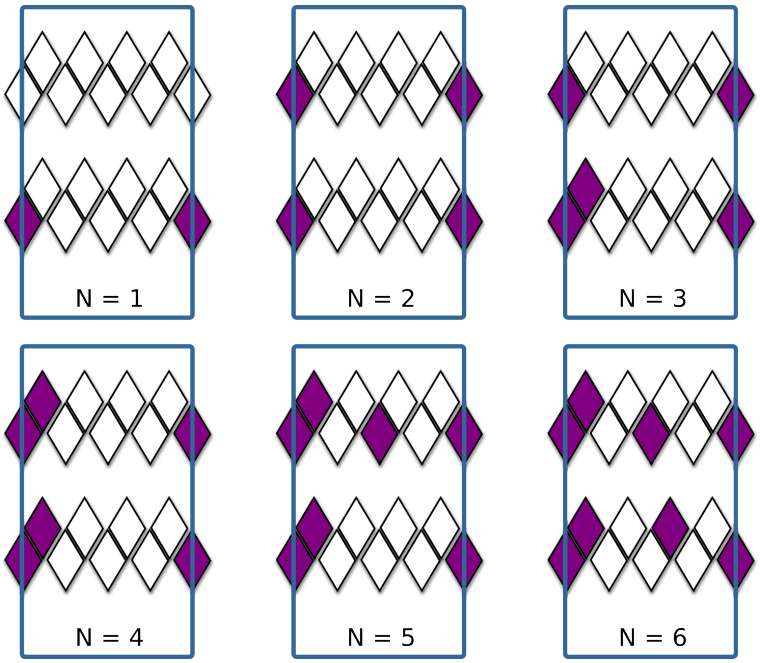

Figure 6.10: Sketch of different configurations of In on the Ga_2O_3 simulation supercell. Occupied octahedra in the β structure double-rows are darkened.

more than at octahedral sites; thus the tetrahedral-site occupation probability is lower than that of octahedral sites by a factor $\exp(-\delta E_t/k_B T_g) \sim 0.5\text{-}1\times10^{-7}$. Therefore, the In concentration in Ga_2O_3 cannot exceed the value whereby the octahedral sites are all occupied, i.e. 50%. Because the Ga_2O_3 structure is made up of double rows of octahedra sharing sides and connected by tetrahedra, there is limited configurational leeway for In placement in the system (see Figure 6.10). The energetics of In substitution in various configurations (a sample is

depicted in Figure 6.10) have been evaluated at concentrations between 6% and 25%, i.e. for 2 to 8 In atoms in the 80-atom, 32-cation 1×4×1 cell, and it have been extrapolated numerically to 50% (tetrahedral sites are neglected). The results have shown that two In's prefer to sit on different double-rows or, failing that, on first-neighbour octahedra in adjacent subrows, which locally resemble the native In_2O_3 bixbyite structure. The formation energy E per In decreases slightly for two and three In per cell, then increases steeply. For the configurations in Figure 6.10 I have found that the excess formation energies over that of a single In are $\delta E_f(2)$=–0.044, $\delta E_f(3)$=–0.019, $\delta E_f(4)$=+0.021, $\delta E_f(5)$=+0.074, $\delta E_f(6)$=+0.144, $\delta E_f(7)$=+0.171, $\delta E_f(8)$=+0.180, in eV/In (the last two are not shown in Figure 6.10). The cell is kept at the volume of the undoped material, which is strictly correct in the dilute limit [101]; at higher concentration I account for an enthalpic energy cost. The concentration is evaluated as the thermal average of the In population in the supercell (M=32 cation sites)

$$x = \frac{\langle N \rangle}{M} = \frac{1}{M} \frac{\sum_{N=1}^{M} N \exp\left[-\beta_g F(N)\right]}{\sum_{N=1}^{M} \exp\left[-\beta_g F(N)\right]}, \tag{6.1}$$

where β_g=$1/k_B T_g$ and $F(N)$=$E_f(1)$+$\delta E_f(N)$–$T_g S$+δH is the free energy per In in the N-In substituted cell. E is the formation energy, S the formation vibrational entropy (S has been estimated from the Debye temperature of the two bulk oxides, and find $T_g S \simeq 0.015$ eV), and $\delta H \simeq 0.09$ eV is the energy cost related to the internal pressure building up in the constrained cell. δH is estimated as the energy difference (per In) between the constrained and volume-relaxed cell; if cell-length changes are allowed along a given direction, as would occur in epitaxy, δH decreases by about one third. In any event, entropy and enthalpy provide only small corrections over the structural energy E_f discussed previously. The thermal population average, Eq.(6.1), gives a concentration of 9%, with an error bar of +2% and –1% estimated varying the δE's between 0.5 and 1.5 times those calculated. Again, this low solubility follows from tetrahedral sites being ruled out and from In occupying only about 3 out of 16 octahedral sites in the cell on (thermal) average.

The gap and the volume change with concentration of $(Ga_{1-x}In_x)_2O_3$ have been calculated in the 80-atom supercell for the structures mentioned. The gap as function of In-content is shown in Figure 6.11, left, and the volume is in the same figure, right. Although the gap is underestimated (a token of using GGA), its concentration change of 17 meV/% is quite similar to 20 meV/%

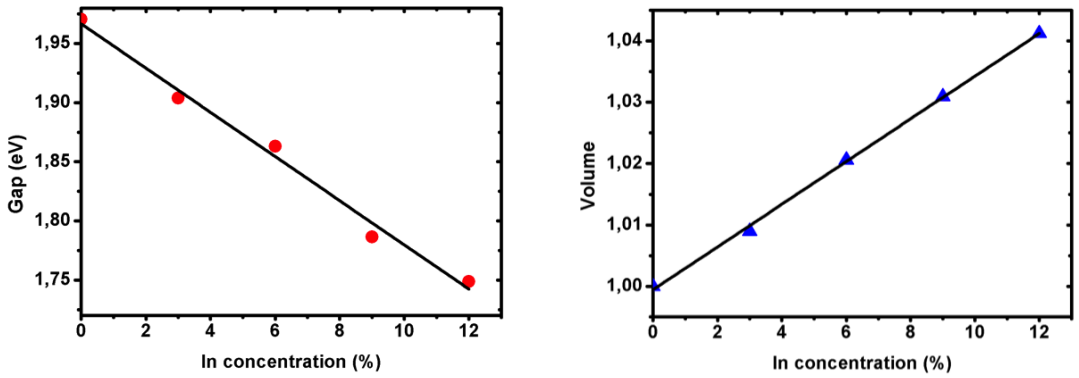

Figure 6.11: Left: direct gap at zone center as function of In concentration. Right: normalized volume of In-doped Ga_2O_3 as function of concentration.

experimentally [84]. Using the the volume change with x and the bulk modulus, the concentration derivative can be evaluated as a pressure derivative, obtaining 2.5 meV/kbar. This is similar to the Ga_2O_3 value of 3 meV/kbar [85, 102], which suggests that the gap is mainly affected by volume change, and marginally by other factors. In this light, the agreement with experiment therefore falls in line with expectations from previous work [103].

6.3.2 Structure and gap over the whole x range of $(Ga_{1-x}In_x)_2O_3$ alloys

In this section, I will report the modelling of $(Ga_{1-x}In_x)_2O_3$ over the entire range of x. Previous results for the low-x end of the composition range are integrated in a comprehensive picture of the miscibility and attendant properties. The main result is that the alloy will phase-separate between approximately 15 and 35% In content for the free-standing alloy (15 and 45% for the epitaxial case). On the low x side, the favoured phase is isostructural with β-Ga_2O_3; above the phase separation region, it is isostructural with bixbyite In_2O_3. We also find that as function of x the gap, volume, and band offsets to the parent compound exhibit discontinuities typical of a first-order phase transition as function of x.

Methods and technical issues. Geometry and volume optimizations as well as electronic structure calculations are performed by the previous method, using the VASP code [5]. The compositional variation has been simulated explicitly mixing In and Ga cations, as dictated by the mole fraction x of In, into two distinct structures. For low x, monoclinic β-Ga_2O_3 phase, doped with In, has been considered; this alloy is free-standing, i.e. energy is calculated at zero stress.

In agreement with previous predictions, reported in the section 6.3, this phase is only relevant up to about $x = 0.2$ (I will also refer to x as a percentage, e.g. 20% in the latter instance). Whereas bixbyite phase has considered over the whole range of x; this is obtained naturally substituting Ga for In in In_2O_3, which is indeed a bixbyite as many other sesquioxides [104, 105]. Specifically, bixbyite alloy has been analysed in two settings: free-standing and In_2O_3-epitaxial. In the latter, the in-plane lattice parameters are fixed to that of In_2O_3 and the vertical lattice parameter and all internal coordinates are optimized.

Both the β and bixbyite supercells contains 80 atoms, i.e. 32 cations. The choice of configurations in the β phase has been discussed previous. For the bixbyite phase, I have found that Ga substitution is slightly favoured at the high-symmetry cation site (see Figure 6.6). Then, I have substituted more and more Ga for In on those sites, and then on the lower symmetry ones. For each x, a few (in fact, mostly symmetry-dictated) configurations have been sampled. All the following discussions are based on the lowest energy configurations found at each x. It should be emphasized that, our sampling being quite coarse, these need not be the absolute minimum energy states for each x; in addition, the possible occurrence of higher-energy configurations in small proportions at finite temperature is neglected.

Phase separation. To address the occurrence of phase separation, the Helmholtz free energy of the mixture are calculated as a function of x. The enthalpic term, PV, vanishes because the pressure P is zero in all cases. The entropy is the sum of mixing and vibrational entropy. The mixing entropy has the standard form:

$$S_m(x) = -x \log x - (1-x) \log (1-x). \tag{6.2}$$

Since growth happens at temperatures comparable to or higher than the Debye temperatures[3], the vibrational entropy can modelled as that of a single-frequency oscillator at the Debye frequency.

Thus, this term can be written as:

$$S_v(x) = 3 \left[(1+n) \log (1+n) - n \log n\right], \tag{6.3}$$

where n is the Planck-Bose distribution

$$n(T,x) = (e^{\Theta_m(x)/T} - 1)^{-1} \tag{6.4}$$

[3]Debye temperature is 420K for In_2O_3 and 870K for Ga_2O_3.

and the mixture's Debye temperature $\Theta_m(x)$ is assumed to be an interpolation of that of the parent compounds:

$$\Theta_m(x) = (1-x)\,\Theta_{Ga_2O_3} + x\,\Theta_{In_2O_3}. \tag{6.5}$$

The phase separation in a mixture occurs when the chemical potential (i.e., in the present case, the free energy per cation site) is a negative-curvature function of an extensive parameter such as x. The values, x_1 and x_2 at which the chemical potential curvature becomes negative and then positive again delimit the phase separation region; in general these bounds depend on temperature T, and the x range they identify is the miscibility gap. When –and if– the negative curvature region vanishes as T changes, i.e. x_1 and x_2 coincide, there is complete miscibility. Although the chemical potential should be used in phase separation, it is also acceptable to use the mixing free energy, i.e. the chemical potential after subtraction of the bulk free energy. For the latter I have used this relation:

$$F_{\rm bulk}(x) = x\,F_{In_2O_3} + (1-x)\,F_{Ga_2O_3}, \tag{6.6}$$

which interpolates the values for two equilibrium bulk phases (bixbyite and β, respectively). The conclusions are essentially the same in both cases.

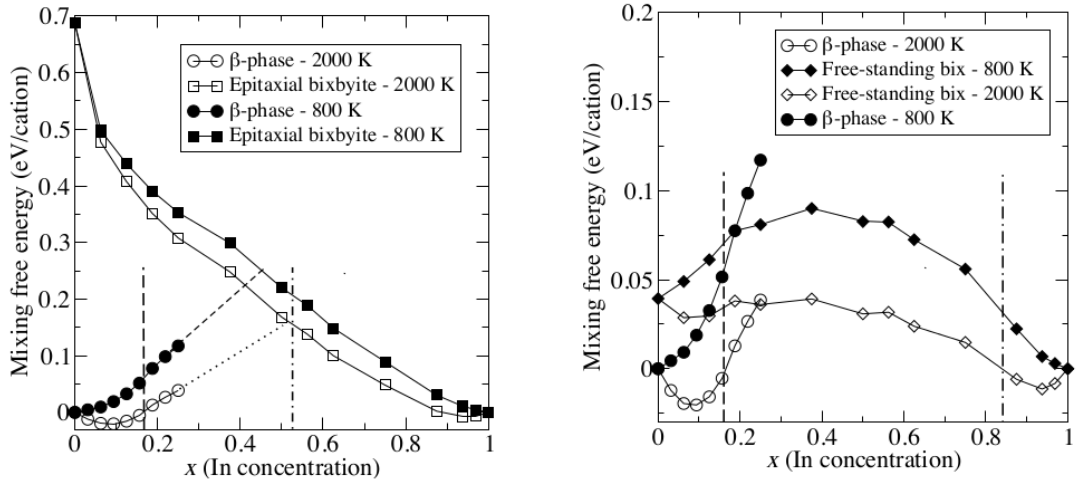

Figure 6.12: Mixing free energy as a function of In concentration at 810 K and 2000 K for β-phase vs epitaxial bixbyite (left panel), and β-phase vs free-standing bixbyite (right panel). The phase separation region extends between the vertical dashed and dash-dotted lines.

The results, reported in the Figure 6.12, suggest a miscibility gap between about 15 and 40% In content at typical growth temperatures. Being related to a change of structure, the miscibility gap does in fact survive up to (and

above) the melting temperatures of the parent compounds. The panel on the right, compares the mixing free energies of the free-standing β phase (circles) with that of the epitaxial bixbyite phase (squares). Whereas the panel on the left, compares the same quantities for the same β phase with that of the free-standing bixbyite phase (diamonds). The considered temperatures are 800 K, a typical growth temperature, and 2000 K, near the melting temperature of the parent compounds. The free energy is evidently upward-convex in a wide region of intermediate x, indicating that a phase separation occurs. The borders of that region, x_1 and x_2, define the miscibility gap.

On the low-x end, the β phase prevails in all cases, and the change in curvature occurs (hence the phase separation region starts) at about $x_1 \simeq 0.15$. This confirms largely our previous estimate (section 6.3) of 10% maximum In solubility, and experiments [100] giving similar results. At high x, the end of the miscibility gap region is estimated at $x_2 \simeq 0.45 \div 0.55$ for the epitaxial case (left panel), subject to large uncertainties in locating the free-energy downturn from the epitaxial phase. Therefore, the miscibility gap is approximately $x \in (0.15, 0.55)$ for the epitaxial bixbyite and β phase.

Comparison with the growth and X-ray diffraction study by Zhang *et al* [84] suggest that all this is quite plausible, even accounting for their epitaxial conditions being different from those simulated. Most importantly, at 2000 K the borders of the phase separation region are about the same as at 800 K, i.e. the miscibility gap hardly changes (it actually may widen slightly). Since the melting temperatures of the parent compounds are around 2200 K, we conclude that in the practical range of T the miscibility gap between the epitaxial and β phases is $x \in (0.15, 0.55)$ independent of T.

The competition between β phase and free-standing bixbyite are shown in Figure 6.12, right panel. A phase separation region exists here too, involving the structure change to the β phase at low x: the lower limit is again $x_1 \simeq 0.15$. The free-standing bixbyite phase is favoured over the β phase (as well as over the epitaxial) over the rest of the x range, from $x_1 \simeq 0.2$ or so onward. However, its own free energy is upward-convex for most of the range; this indicates a phase separation between Ga_2O_3 and In_2O_3 within the bixbyite phase; the change in curvature on the high x side is approximately at $x_2 \simeq 0.8 \div 0.85$. Therefore the overall miscibility gap is $x \in (0.15, 0.85)$ in the free-standing case. This is quite clearly the case at both 800 K and 2000 K. Thus, as in the epitaxial case, we conclude that in the practical range of T the miscibility gap for free-standing bixbyite is $x \in (0.15, 0.85)$ independently of T. An experimental determination

of the Ga_2O_3-In_2O_3 phase diagram [75] suggests that indeed at the In end of the range the single-crystal stability region is quite marginal, being limited to x>0.9 or so.

Discontinuity of gap and volume across the transition. Interestingly, there are other properties of the materials that exhibit discontinuities as function of concentration due to the change in phase and structure. In Figure 6.13, left panel, the calculated optimized volume are shown in the two free-standing bixbyite and β phases, showing a clear volume discontinuity at any given x. At x_1<x, both phases start to form and coexist; the volume first drops, then recovers as x increases.

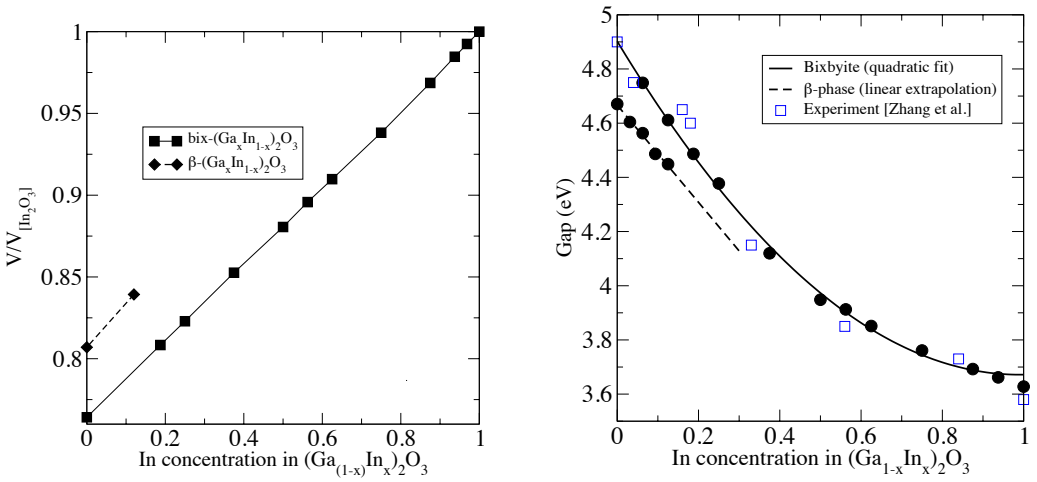

Figure 6.13: Left panel: volume vs mole fraction for the free-standing β and bixbyite phases. Right panel: fundamental gap in the same phases and interpolations vs x (quadratic for bixbyite; linear at low x for β). A correction for the gap error has been introduced. The gap show a sizeable bowing in bixbyite at large x.

The energy gap shows analogous interesting features. The β phase has a linear decrease in good agreement with pressure experiments [2,84]. The bixbyite gap is also linear at low x, but picks up a significant bowing near $x = 1$. To correct for the semilocal density-functional error, the GGA calculated gap has been supplemented with an ad hoc 'scissor'-like correction

$$\delta E_g(x) = 2.5x + 2.7(1 - x)eV \tag{6.7}$$

which brings the GGA gap to the experimental value in Ga_2O_3 and In_2O_3 [85,106] (incidentally, the correction reduces the bowing as obtained from GGA eigenvalues). Since the lowest gap is dipole-forbidden, to compare with the experimental optical onsets [84] I have estimated the position of the optical onset at all x as the

GGA gap value (corrected by equation 6.7) plus the difference of optical onset and minimum gap in In_2O_3 (0.55 eV). The agreement is decent, on the experiment side, the data are for films grown on sapphire, the In content is generally lower than the nominal one especially at intermediate x, and the gap in the x = 0 and x = 1 limits is larger than in most reports; on the theory side, I have applied a simple correction that offers no guarantee of being equally appropriate for all transitions and all x. As I now discuss, an interesting crossover behaviour is more easily observable in the band offsets at the interface with the parent compounds.

6.4 $(Ga_{1-x}In_x)_2O_3$ alloys at $x \sim 0.5$: $InGaO_3$

In the previous sections I have shown that $(Ga_{1-x}In_x)_2O_3$ has a monoclinic crystal structure for low In content and a cubic bixbyite phase for highest In contents. In addition, in accord with experimental results [77], intermediate alloying shows an additional crystallographic phase. In particular, around 50% of In content, a new centrosymmetric phase, belonging to hexagonal $P6_3/mmc$ space group, is in competition with the monoclinic and bixbyite phases. Theoretical studies on $(Ga_{1-x}In_x)_2O_3$ phase stability and optical properties have been published recently also by Peelaers *et al.* [107], but the picture is apparently still far from complete. In recent growth experiments [108,109] on the $(Ga_{1-x}In_x)_2O_3$ alloy in the vicinity of $x = 0$ and $x = 0.5$ have suggested that stable (or metastable) phases other than those so far assumed as ground state may in fact be stabilized. In particular, in Schewski *et al.* work [108] three competing phases are reported to appear near $x \sim 0.5$: that derived from the bixbyite structure of In_2O_3; a hexagonal phase previously observed at exactly $x = 0.5$; and finally a monoclinic close relative of the β-Ga_2O_3 structure. In this section, I will report a revised phase diagram of $(Ga_{1-x}In_x)_2O_3$ accounting for new findings around $x \simeq 0.5$. In brief, the results are that the hexagonal and β structures do indeed compete energetically with the bixbyite phase that was expected based on previous results, and this competition occurs only in the vicinity of $x \sim 0.5$.

6.4.1 Structure optimization

The same method previously used is considered to geometry and volume optimizations. In particular, a 470.7eV cutoff energy and a 2×2×2 Gamma centered grid are used[4]. Atom parameters are in perfect accord with the experimental

[4]For hexagonal lattices, the energy converges significantly faster with Γ centered grids than with standard Monkhorst Pack grids.

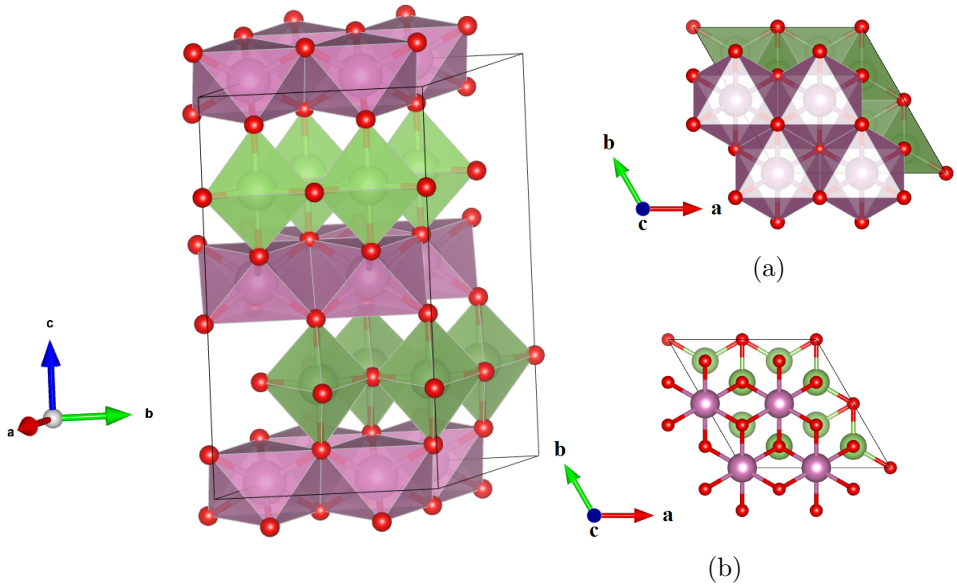

Figure 6.14: Supercell of $Ga_{1-x}In_x)_2O_3$ with 50% In-concentration. In this structure In is six-fold coordinated occupying 2a Wyckoff sites while Ga is five-fold coordinated occupying 2c Wyckoff sites.

data, although the lattice parameters are slightly lower than the calculated one. In Table 6.5, structure parameters of $InGaO_3$ in the unit cell, are reported, in parentheses data are referred to that Shannon's work.

$P6_3/mmc$ (No. 194)	a = b = (a = b = $\alpha = \beta = 90°$,	3.36878Å 3.310Å) $\gamma = 120°$	c = 12.20095Å (c = 12.039Å)	
Atoms	**x**	**y**	**z**	**Wyc**
In	0.00000	0.00000	0.00000	2a
Ga	0.33333	0.66667	0.25000	2c
O	0.00000	0.00000	0.25000	2b
O	0.33333	0.66667	0.08716	4f

Table 6.5: Calculated structure parameters of $InGaO_3$. The unit cell contains ten atoms, i.e. Z=2 formula units per unit cell.

In this structure In is coordinated by six oxygens, the polyhedral share edge and form a layer normal to c-axes. These layers alternate with layers of GaO_5 trigonal bipyramids, each of which shares its two vertices with three InO_6 polyhedral (see Figure 6.14).

Both out of interest for the possible energetic stability, and for the possibility that the structure might turn out to be polar, I have investigated this phase in a range of x from 0.45 to 0.55.

The main result is that in this whole region this phase is lower in energy than,

therefore favoured over the bixbyite, and also degenerate at $x = 0.5$ with the β phase. The difference is a sizeable 0.1 eV/cation. As to the alloy energetics, calculations reveal that the lowest energy structures of the sample of configurations for the hexagonal symmetry in the vicinity of $x = 0.5$ are lower in energy by about 0.1 eV than the free-standing bixbyite configurational sample, and therefore more stable than bixbyite, or at least (given the model uncertainties) competing with it for stability. In the Schewski *et al.* paper reporting the occurrence of hexagonal phase crystallites, β-phase inclusions were also reported, in a region that I had previously neglected given its seemingly skyrocketing energy at large x. Therefore, a few concentration points around $x = 0.5$ for the β phase have been calculated, the results are that indeed it competes with the hexagonal phase and the bixbyite. As in previous section the sampling of configurations is very limited and therefore the error bars on the energies determining relative stability should be assumed to be large.

In addition, structural analysis have shown a reduction of the symmetry in two type of polar phases, hexagonal and orthorhombic one. The little variation of In-concentration could lead to an occurrence of a little electric dipol in structures with orthorhombic symmetry. Unfortunately, it never occurs, even at a generic concentration, for generic atomic arrangements, and enabling all kinds of symmetry lowering starting from $P6_3mmc$. In conclusion, this phase, is robustly non polar.

6.4.2 Revised phase diagram

Previous calculations have revealed that the β structure of Ga_2O_3 is disfavored over bixbyite for x above 0.2 or so. The internal energy of that phase increased drastically and monotonically as a function of x, so I refrained from pursuing it further. However, growth experiments indicate that when $x = 0.5$ the β phase is indeed present [108]. I have thus revisited the previous assessment and studied the β phase in that region of concentration. It turns out that at exactly $x = 0.5$ the β phase is more stable than bixbyite and as stable as the hexagonal phase discussed above. At this concentration, In atoms all occupy octahedra, and Ga atoms all occupy tetrahedra. If we move away from exact 50-50 concentration, however, the energy shoots up immediately, accompanied by a volume collapse by about 10% at $x = 0.47$ and $x = 0.53$, and increasing on both sides of the energy minimum.

Based on the calculations discussed above it is possible to revise the phase diagram in Figure 6.12 to account for the new phases. The diagram is reported

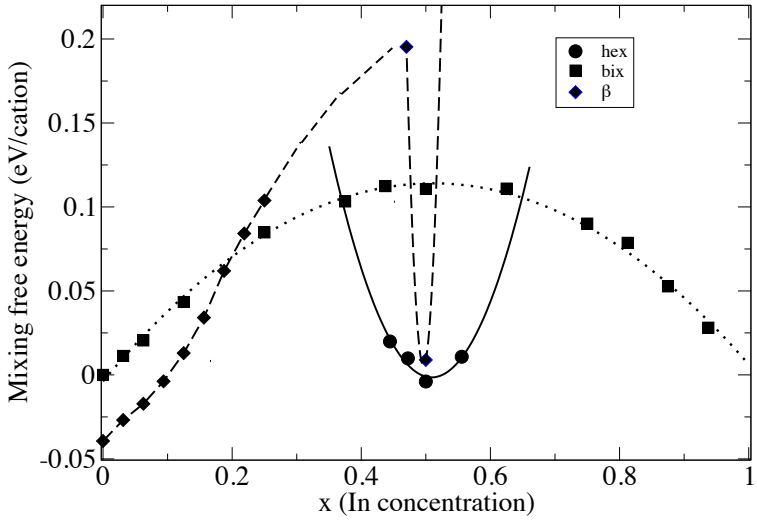

Figure 6.15: Revised phase diagram for $(Ga_{1-x}In_x)_2O_3$ for T=800 K.

in Figure 6.15 in the form of a mixing free energy, constructed as discussed previously. The temperature is 800 K, a typical growth temperature. The stability of the β phase up to about $x = 0.2$ is confirmed, and so is the phase separation into components of the bixbyite phase (signalled by the convexity of the free energy). The hexagonal phase is, now, the stable one in a range that, conservatively, extends from $x \sim 0.4$ to $x \sim 0.6$. Given the upward-concave free energy, the hexagonal phase does not phase-separate into binary components in this range. In addition, as mentioned, the β phase has a very narrow stability slot at $x = 0.5$. Moreover, the phase boundaries are quite insensitive to temperature, at least within the bounds of our model (there is no guarantee, of course, that the vibrational entropies of all phases will be the same). Thus, as dictated by the curvature of the mixing free energy, there is full miscibility of the two binary oxides at all temperatures in the ranges $x \in (0, 0.17)$ and $x \in (0.35, 0.65)$, where, respectively, the β and the hexagonal structures are adopted. In the bixbyite-dominated ranges $x \in (0.17, 0.35)$ and $x \in (0.65, 0.85)$, phase separation into binaries is expected, from the negative curvature of the mixing free energy.

6.5 Conclusion

Using density-functional ab initio theoretical techniques, I have established that $(Ga_{1-x}In_x)_2O_3$ could exist in the β phase at low in concentration (below 15% or so) and in the bixbyite phase at high In concentration (above 35 to 50% depending on the epitaxial conditions). The compound could phase-separate at intermediate mole fractions, and the two phases will coexist. This amounts to a first-order disproportionation phase transition as function of the mole fraction x. Discontinuities in the calculated volume, gap, and other electronic properties also confirm this conclusion. In addition, I have found that the gap and the volume as function of x exhibit discontinuities typical of a first-order phase transition as function of x.

Finally, from further calculations, the phase diagram of $(Ga_{1-x}In_x)_2O_3$ have been revised, showing that the β phase is stable (without phase separation into binary components) at low x and exactly at 50-50 concentration; a new hexagonal phase is stable (again without phase separation into binary components) for x from about 0.4 to 0.6, where it is robustly non-polar; and bixbyite will be stable for x between 0.2 and 0.4, and upward of 0.6, but should phase-separate into binary components.

CHAPTER 7

Band offset at interfaces

Band offsets at interfaces are key quantities in the design and engineering of heterostructures. The discontinuity in the local band structure at semiconductor-semiconductor and semiconductor-oxide interfaces is a crucial physical property for the operation of most electronic and optoelectronic devices [110]. For example, high-speed transistors and semiconductor lasers, which have significant impacts on information and communication technology. Ab initio theory has been predicting reliable offsets all along. The correct way of calculating band offsets [111] is as the sum $\Delta E_b + \Delta V$ of the interface jump ΔV in electrostatic potential between the two regions being interfaced, and the difference $\Delta \mathrm{E}_b$ of the band edge of interest in each of the two materials, taken separately each in their own internal potential. In particular, since the ab initio pseudopotentials used here are nonlocal, the band energies in each bulk material are referenced to the *macroscopically averaged* electrostatic potential, $\bar{V}(z)$. The variation of the space coordinate $\mathbf{r}$ is limited to the component perpendicular to the interface, and values of the potentials are averaged over the remaining two coordinates, i.e. averaged in the plane parallel to the interface:

$$\bar{V}(z) = \frac{1}{Na^2} \int V(\mathbf{r}) dxdy \tag{7.1}$$

where a is a cell parameter [112,113]. Figure 7.1 provides an example of planar averages of the electron density (full line) response at a GaAs/AlAs heterojunction.

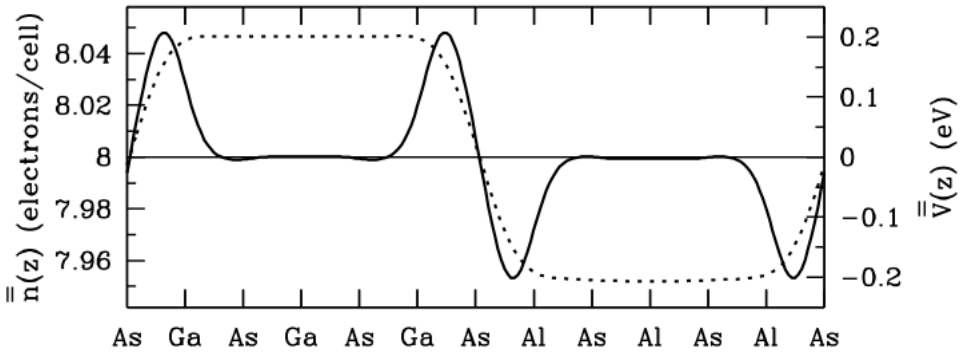

Figure 7.1: Macroscopic averages of the electron density (full line) and the corresponding electrostatic potential (broken line) at a GaAs/AlAs heterojunction. Ref. [111].

7.1 Ga_2O_3 / $(Ga_{1-x}In_x)_2O_3$

For these calculations a 2×2×2 160-atom cell have been used, as depicted in Figure 7.2, upper panel. The (100) interface has been construited as half of the supercell along the (100) axis with pure β-Ga_2O_3, and the other half with a Ga-In alloy. Firstly, the concentration picked was 12% as it is near the maximum achievable (as discussed previously), and because, given the energetics constraints, the configurational freedom of In is very limited, and there is no serious need for a detailed In configurations sampling, which would be computationally unfeasible. The (100) interface has been chosen for computational convenience; it remains to be assessed how much the offsets change with orientation.

This super-unit cell repeats periodically the two layers, effectively producing a superlattice; it is found that the thickness of the layers is sufficient to reproduce identifiable bulk regions on either side of interface, with flat, bulk-like average potential, as shown in Figure 7.2, lower panel. This superlattice are considered in two strain states, epitaxial and free-standing; in the former case, the lattice constants have fixed in the *bc* crystal plane and the monoclinic angle to those of Ga_2O_3, and only the a lattice parameter has been relaxed; in the second case, all lattice parameters have been optimized. The internal coordinates have been optimized in all cases.

The local potential has been determined including only the ionic and Hartree potential. VASP calculates the average electrostatic potential at each ion by placing a test charge with the norm 1, at each ion and calculating

$$\bar{V}_n = \int V(\mathbf{r})\rho_{\text{test}}(|\mathbf{r} - \mathbf{R_n}|)d^3\mathbf{r} \tag{7.2}$$

In this supercell the average electrostatic potential are displayed in Figure

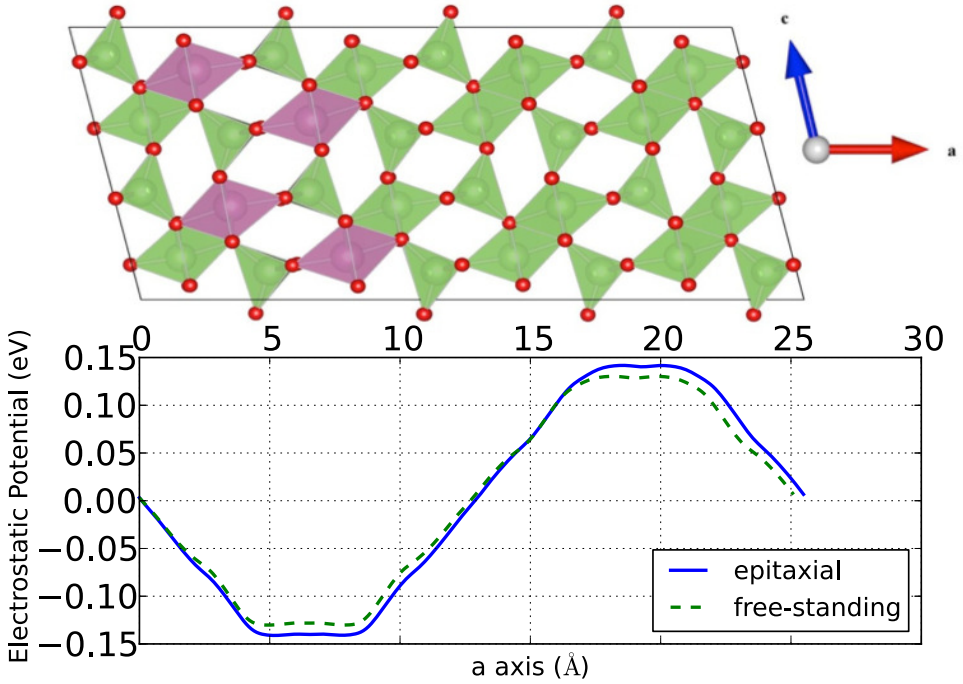

Figure 7.2: Upper panel: simulation cell for the (100) superlattice (for definiteness I display the epitaxial geometry). Lower panel: the electrostatic potential of the superlattice, showing small but definite bulk regions on either side of the interface. The potential is aligned with the lower side of the cell.

7.2, lower panel. As schematized in Figure 7.3, at the (100) interface between Ga oxide and the alloy at 12% In, an alignment of type-B staggered results when the alloy is epitaxial on Ga_2O_3, and type-A straddling in a free-standing superlattice; the valence offsets from Ga_2O_3 to $(Ga_{1-x}In_x)_2O_3$ are –0.14 eV (Ga_2O_3-epitaxial) and 0.15 eV (free-standing), and the conduction offsets are –0.41 eV (epitaxial) and –0.05 eV (free-standing). This considerable difference is due almost entirely to strain-induced shifts of the valence band maximum (VBM) and conduction band minimum (CBM), whereas the electrostatic interface alignment is hardly insensitive to strain. This indicates that a marked dependence on the strain state, and hence on the growth quality, is to be expected. Importantly, given the limited In solubility, this is about as much of an offset as can be expected between Ga_2O_3 and $(Ga_{1-x}In_x)_2O_3$.

I expect the above estimate to be rather accurate. This interface is between materials differing only very slightly due to compositional changes, so that beyond-DFT corrections to the band edges will essentially cancel out; on the other hand, strain-induced band-edge shifts are known to be well described by standard functionals [83]. In this case, the gap error essentially cancels out, so the absolute value of the gap is insensitive to the offsets.

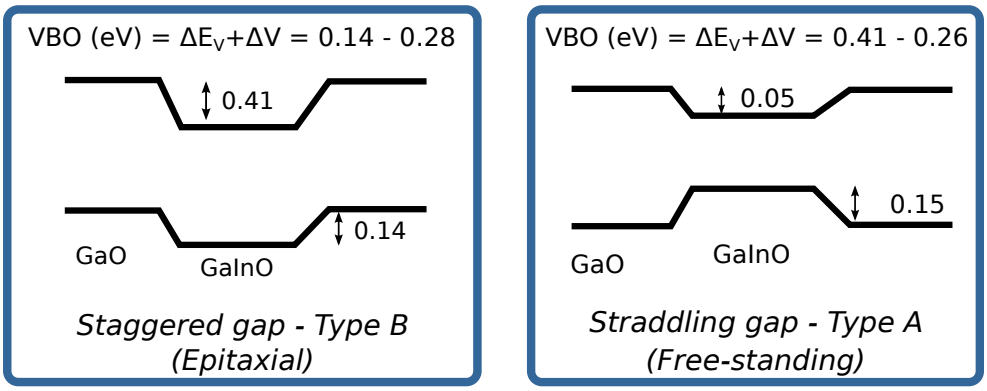

Figure 7.3: Schematic of the staggered and straddling offset for, respectively, the epitaxial and free-standing superlattice configurations.

7.2 In_2O_3 / $(Ga_{1-x}In_x)_2O_3$

In this section, I have extended the work to a much larger range in the bixbyite structure. I have simulated the (001)-like interface with $In_2O_3/(Ga_{1-x}In_x)_2O_3$ superlattices epitaxially constrained to In_2O_3, containing 160 atoms in the primitive cell, and with explicit atomic substitutions.

On the bixbyite side of the phase separation region, the offsets are again type-B (a relatively uncommon occurrence in itself), but most interestingly they are staggered in the opposite direction, i.e. both the conduction and valence offsets encountered in going from the parent compound into the alloy are generally positive, whereas they were negative in the low-x limit (see the sketches in Figure 7.4. This suggests interesting perspectives for interface offset tuning in this alloy system. The offset values are also rather interesting in terms of potential charge confinement. We purposely refer to offsets only, starting from zero at x=0 and x=1, as any gap corrections will largely cancel out of the offsets themselves. Of course, in the case of free-standing bixbyite, all the calculated values refer to the mixed phase and not the possibly compositionally segregated one.

7.3 Conclusion

In summary, I performed first-principles calculations of the interface properties of the $Ga_2O_3/(Ga_{1-x}In_x)_2O_3$ and $In_2O_3/(Ga_{1-x}In_x)_2O_3$ systems. This calculations proves that the band offset between Ga oxide and the alloy at 12% In is type-B staggered when the alloy is epitaxial on Ga_2O_3 and type-A straddling in a free-standing superlattice. The valence offsets from Ga_2O_3 to $(Ga_{1-x}In_x)_2O_3$ are -0.14 eV (Ga_2O_3 epitaxial) and 0.15 eV (free-standing), and the conduction

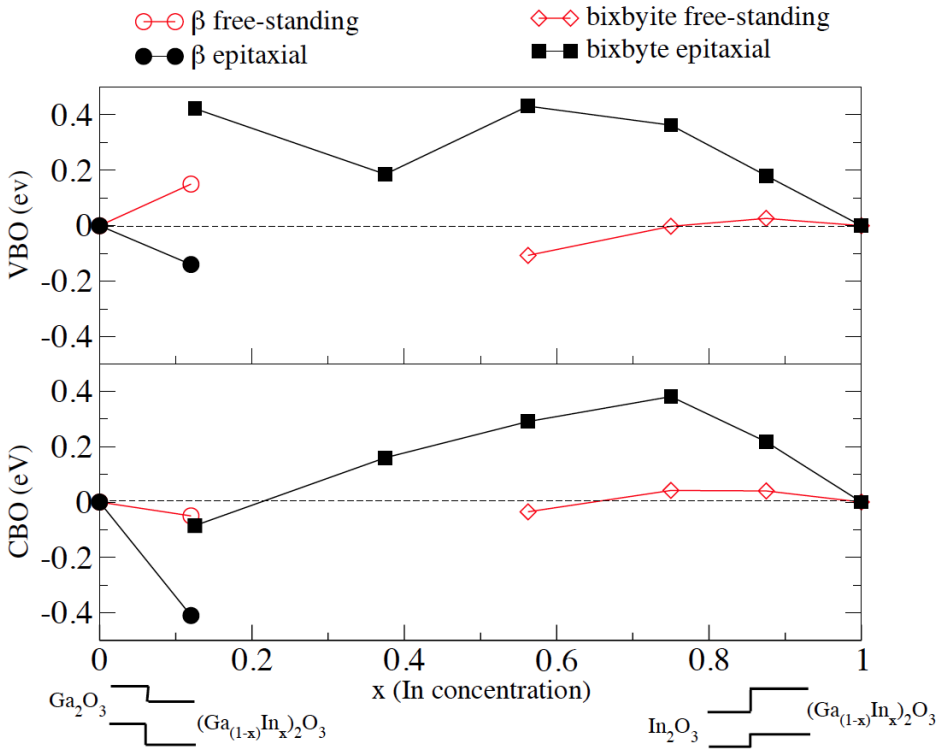

Figure 7.4: Valence (VBO, top) and conduction (CBO, bottom) interface band offsets between In_2O_3 and $(Ga_{1-x}In_x)_2O_3$ in the bixbyite phase, both epitaxially constrained on In_2O_3, or with compliant substrate. The offset between Ga_2O_3 and low x $(Ga_{1-x}In_x)_2O_3$ at x $\simeq$ 0.1 in the β phase for the same conditions are also reported.

offsets are -0.41 eV (epitaxial) and -0.05 eV (free-standing). In the latter case, from calculation of $In_2O_3/(Ga_{1-x}In_x)_2O_3$ systems, the interface band offsets results to be largely type-B staggered and positive at large x, whereas staggered and negative in the low-x limit.

CHAPTER 8

Epsilon-Ga_2O_3

In this chapter, I report recent calculations on the energetics and polarization properties of the ε-Ga_2O_3 phase. Firstly, this phase was synthesized by Roy *et al.* [80] from powder X-ray diffraction techniques, but identified in 2013 by Playford *et al.* [114]. Very recently, from growth experiments, Oshima *et al.* [109] reported that the ε phase of Ga_2O_3 can be obtained at 820 K via epitaxial constraints, whereas a bulk phase transition is not expected below 1500 K [115]. The ε phase of Ga_2O_3 is only slightly energy-disfavored over the stable β, and as dictated by symmetry it has a large spontaneous, or permanent, polarization of about 0.25 C/m^2. Most importantly, once it is stabilized, this phase cannot be transformed into (is not symmetry-related to) the stable β phase. These results do indeed open up some interesting perspectives, such as exploiting the polarization properties of ε-Ga_2O_3.

8.1 Structure optimization

The ε-Ga_2O_3 phase is structurally similar to the same phase of ε-Fe_2O_3 or κ-Al_2O_3 [116] and its space group is $Pna2_1$, which does not contain inversion. ε-Ga_2O_3 structure derives from a ABAC pseudo-close-packed stacking of four oxygen layers, with Ga occupying octahedral and tetrahedral sites. This structure, as displayed in Figure 8.1, consists of triple chains of octahedra sharing edges and simple chains of tetrahedra sharing corners which run parallel to the a direction. In Table 8.1 I report the structural parameters of the equilibrium

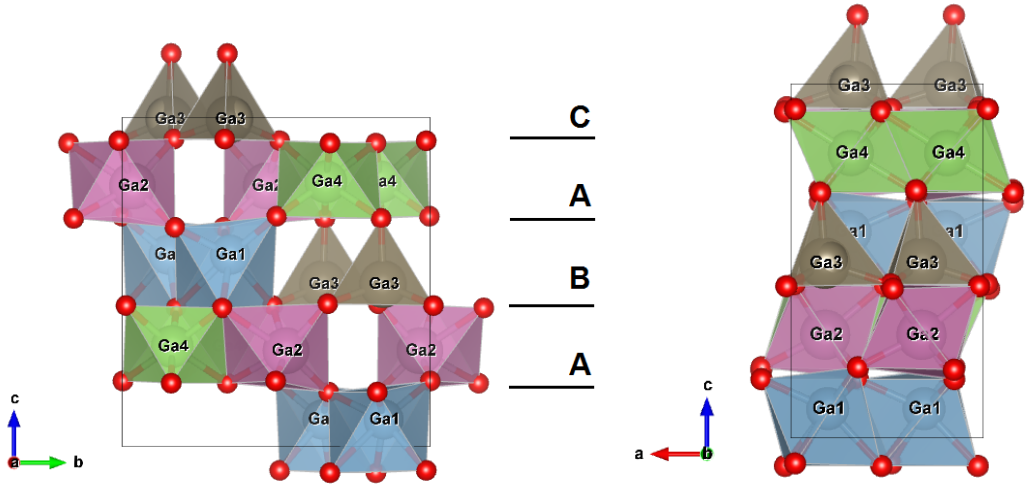

Figure 8.1: Different views of the orthorhombic phase of Ga_2O_3. Ga occupies octahedral (Ga1, Ga2, Ga4) and tetrahedral (Ga3) sites which form zigzag ribbons of edge-sharing octahedra and corner-sharing tetrahedra.

structure obtained after cell geometry and volume fully relaxation. I have used a 4×2×2 **k**-point grid for Brillouin zone integrations and a 490.7 eV plane wave energy cutoff. The calculated structural parameters are in essential agreement

Pna2₁ (No. 33)	a = 5.12604 Å (a = 5.120 Å)	b = 8.80567Å (b = 8.792Å)	c = 9.42423Å (c = 9.410Å)	
		$\alpha = \beta = \gamma = 90°$		
Atom	**x**	**y**	**z**	**Wyc**
O1	0.97031	0.32468	0.42135	4a
O2	0.52269	0.48831	0.42852	4a
O3	0.65081	0.00160	0.19973	4a
O4	0.15307	0.15863	0.19308	4a
O5	0.84866	0.17085	0.66597	4a
O6	0.51974	0.16764	0.93392	4a
Ga1	0.19176	0.15034	0.58280	4a
Ga2	0.67863	0.03213	0.79146	4a
Ga3	0.17784	0.15200	0.99363	4a
Ga4	0.81228	0.16176	0.30414	4a

Table 8.1: Structure parameters of ε-Ga_2O_3 in the orthorhombic phase, *Pna2₁*, with Z=8 formula units per crystallographic cell.

with a previous study [115], parenthetical parameters to compare. The total energy results to be -29.6958 eV/per formula unit and the energy difference with the β phase at zero temperature is just 90 meV per formula unit as found previously; indeed, Ref. [80] predicted that the ε phase could become favoured over the β at temperatures above 1500 K, still well below the melting temperature of Ga_2O_3.

Indeed, this phase has most recently been grown epitaxially by Oshima *et al.*

[109]. Epitaxial stabilization of the ε phase is not endangered by a possible decay in the β ground state. This is due to the simple reason that there is no possible ε-to-β symmetry path, since the space group *Pna2₁* is not a supergroup of *C2/m*. This is quite analogous to the situation of III-V nitrides, which are wurtzites (group *P6₃mc*) and cannot transform, again for symmetry reasons, into its close relative zincblende (group $F\overline{4}3m$), despite the volume being almost the same and the energy difference being about only 10 meV/atom (the two ε and β phases also have the same volume and an energy difference of about 15 meV/atom). However, just as ε-Ga_2O_3, zincblende nitrides can be grown under appropriate epitaxial constraints.

8.2 Pyroelectricity and piezoelectricity

Since the space group *Pna2₁* is polar, observable polar vector quantities are allowed in ε-Ga_2O_3. The polarization is an obvious example. To calculate it properly as difference between polar and non-polar state, as prescribed by polarization theory, I have investigated a virtual phase transitions of a hypothetical non-polar parent phase into the polar ε phase. ("Non-polar parent" here means a structure having a higher symmetry than the polar one.) I have used the PSEUDO [117] program of the Bilbao Crystallographic Server[1], which is designed to detect pseudosymmetry in a given structure and derive a virtual parent high-symmetry structure. In particular, PSEUDO checks the approximate coincidence of the transformed structures with the original one through an identification of the atomic displacements relating the two configurations. If these displacements are smaller than a fixed tolerance, the structure is flagged as pseudosymmetric.

Among the supergroups of *Pna2₁*, the centrosymmetric phase is chosen to have symmetry group *Pnma* (No. 62). The structural parameters obtained from cell geometry and volume fully relaxation, using the same **k**-point grid for Brillouin zone integrations of the ε phase, are report in Table 8.2. The spontaneous polarization has been calculated, as dictated by the modern theory of polarization [31–35], as difference of the values calculated in this phase and in a centrosymmetric parent phase. In this case, the polarization results $\Delta P = P_{\mathrm{Pna2_1}} - P_{\mathrm{Pnma}} = 0.233$ C/m^2 along the polar c axis. The predicted phase have zero polarization in the chosen crystallographic setting; the evolution of P with a path connecting the two structures is displayed in Figure 8.2. This result guarantees that the polarization is, as desired, the minimum value modulo the

[1] `www.cryst.ehu.es`

Pnma (No. 62)	a = 5.07204 Å	b = 6.75903 Å $\alpha = \beta = \gamma = 90°$,	c = 14.38827 Å	
Atom	**x**	**y**	**z**	**Wyc**
O1	0.97866	0.96892	0.69076	8d
O2	0.50000	0.00000	0.50000	4a
O3	0.48654	0.75000	0.00082	4c
O4	0.97372	0.75000	0.85656	4c
O5	0.97649	0.25000	0.84670	4c
Ga1	0.11224	0.00193	0.81658	8d
Ga2	0.86799	0.25000	0.97905	4c
Ga3	0.60602	0.75000	0.88510	4c

Table 8.2: Structure parameters of Ga_2O_3 in the orthorhombic phase, *Pnma*. The structure has been predicted by PSEUDO.

polarization quantum.

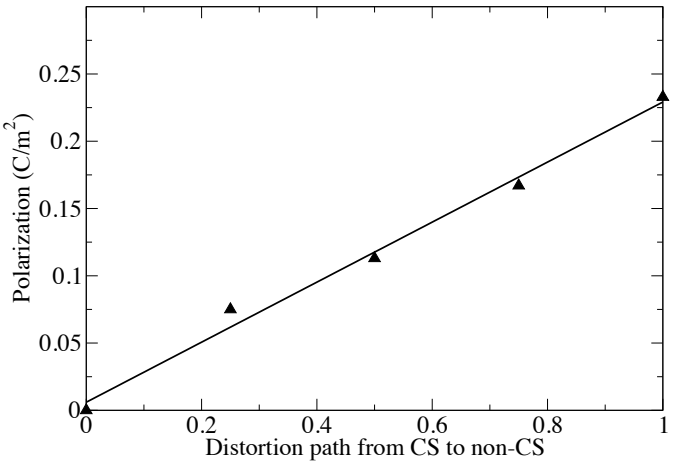

Figure 8.2: Polarization calculated along a path connecting the centrosymmetric parent phase (0) to non-centrosymmetric ε-Ga_2O_3 (1).

This value is similar to that of $BaTiO_3$, a factor of 3 larger than in AlN, and nearly a factor 10 larger than in GaN. The structure of the ε phase is not structurally switchable (in the same sense that wurtzite is not: of course the polar axis can be inverted by inverting the growth direction); therefore P is expected to maintain its orientation along the polar axis within any given crystalline domain. ε-Ga_2O_3 can thus be classified as a pyroelectric material.

The symmetry of the ε-Ga_2O_3 structure allows for five distinct piezoelectric coefficients, as it is reported in Appendix E on page 112. Here, the only diagonal coefficient, e_{33}, has been calculated, by finite differences differentiation of the polarization with respect to the axial strain $\varepsilon_3=(c\text{-}c_0)/c_0$. The result is e_{33}=0.77 C/m^2, which is in line with typical coefficients of strongly polar semiconductors (oxides and nitrides), although much smaller than the values of up to 20 C/m^2

of strong ferroelectrics (e.g. PZT [118, 119]).

These results do indeed open up some interesting perspectives. For example, one may exploit the polarization properties of ε-Ga_2O_3 growing it epitaxially on GaN, to build a high-mobility transistor. Since the polarization difference is very large, electron gases at huge concentrations could be obtained at a GaN/ε-Ga_2O_3 interface; and since the gap of ε-Ga_2O_3 is much larger than that of GaN, the confinement should be quite efficient. It would then be possible to set up a "writ-large" version of the GaN/AlGaN HEMTs currently in use.

8.3 Conclusion

The study on the ε-phase of Ga_2O_3 have confirmed that this is the second most stable structure beside β-Ga_2O_3. This phase has a large spontaneous polarization (0.25 C/m^2) and a sizeable diagonal piezoelectric coefficient (e_{33}=0.77 C/m^2). Symmetry dictates that this phase, once epitaxially stabilized, will not transform back into the ground-state β, despite having the same volume and a small energy difference; in this sense, the ε-β relation is similar to the one between zincblende and wurtzite III-V nitrides.

CONCLUSIONS

First principles calculation allows to make quantitative predictions of materials properties and to provide an explanation of some properties that have already been proved experimentally.

In this Ph. D. thesis, I report the results about theoretical prediction of a new "multiferroic structure" and a "new optical structure".

The first part of my research has been focused on a new class of multifunctional magnets called multiferroics, where magnetism and ferroelectricity are strongly coupled together. For example, electric polarization may be switched by applied magnetic fields, and vice-versa. Because of that these materials can be considered as suitable candidates for several applications, in particular, in the field of information storage such as random access memory devices. Among the class $A_nB_nO_{3n+2}$ of layered-perovskite oxides, I have considered the Lanthanum-titanate, and in order to achieve multiferroicity in this topological ferroelectric I have suggested an isovalent substitution of the Ti-cation, non magnetic, by a magnetic cation, Mn.

In a nutshell, this study is focus on structural, electronic, ferroelectric and magnetoelectric properties of $La_2Mn_2O_7$, through first-principles based on density functional theory calculations. The polarization has been calculated, according to the Modern Theory of Polarization, as a difference of the values calculated in the ferroelectric phase ($Cmc2_1$) and in a centrosymmetric parent phase ($Cmcm$). The polarization results along the z axis with a value P_s=0.17 C/m^2 that is comparable to displacive ferroelectrics, and the estimated T_C is about 1500 K. The stable magnetic structure is an approximate G-type AF, as expected from

superexchange between Mn^{4+} with majority t_{2g} orbitals. The estimated Neél temperature is $T_N = 270$ K in the Ising 3D AF model.

In addition, magnetic noncollinear spin-orbit calculations reveal that spins point along the *c* direction, and that LMO is a weak ferromagnet to spin canting in the *bc* plane, interpreted by Dzyaloshinsky-Moriya (DM) interaction. Interestingly, LMO has a lattice-mediated magnetoelectric tensor, α, larger than of the paradigmatic magnetoelectric Cr_2O_3 and with only non-diagonal elements, which results in a cross-field response. In summary, I have found that $La_2Mn_2O_7$ is a topological multiferroic with large magnetoelectric response.

The second part of my research is based on the investigation about Gallium, Ga_2O_3, Indium oxides, In_2O_3, and their solid solutions. This study is motivated by the recently attracting interest on novel materials systems for highpower transport devices as well as for optical ultraviolet absorbers and emitters. Resorting to an appropriated optimization of physical properties and nanostructuration of Gallium- and Indium-based semiconductor layers of chosen composition, it is possible to tune their key properties (such as band gaps, interface band offsets, vibrational absorptions, as well as, potentially, the magnetic behaviour) leading overall to novel multi-functional nanomaterials, nanostructures and devices. This may enable the design of devices based on interfaces $Ga_2O_3/(Ga_{1-x}In_x)_2O_3$ or $In_2O_3/(Ga_{1-x}In_x)_2O_3$ such as high-power field effect transistors and far-UV photodetectors or emitters.

Firstly, I have performed first-principles calculations on the electronic and local structural properties of both bulk oxides in the β and bixbyite phases of Ga_2O_3 and In_2O_3, respectively. Thereafter, I have analysed the miscibility between this compound, showing that the β phase is stable (without phase separation into binary components) at low x and exactly at 50-50 concentration; a hexagonal phase is stable (again without phase separation into binary components) for x from about 0.4 to 0.6, where it is robustly non-polar; and bixbyite will be stable for x between 0.2 and 0.4, and upward of 0.6, but should phase-separate into binary components.

Later calculations have performed on interface properties of the Ga_2O_3 / $(Ga_{1-x}In_x)$ system. The band offset between Ga oxide and the alloy at 12% In results of type-B staggered when the alloy is epitaxial on Ga_2O_3, and type-A straddling in a free-standing superlattice. Whereas in $In_2O_3/(Ga_{1-x}In_x)$ interface the band offsets results to be largely type-B staggered and positive at large x, on the contrary, staggered and negative in the low-x limit.

Finally, I have found that another phase, ε, of Ga_2O_3 is in competition with the that β. Interestingly, ε phase have a large spontaneous polarization (0.25 C/m^2) and a sizeable diagonal piezoelectric coefficient (e_{33}=0.77 C/m^2). Moreover, for reasons of symmetry, this phase, once epitaxially stabilized, will not transform back into the ground-state β, contrasting with previous works. In summary, I found that stable Ga_2O_3 and In_2O_3 alloys could exist in particular concentration, it is also possible to engineer devices based on interfaces between pure oxides and alloys for optical devices.

APPENDIX A

$La_2Mn_2O_7$ cell parameters

Cmcm		a = 3.9365Å b = 25.0350Å c = 5.3131Å $\alpha = \beta = \gamma = 90°$		
Atoms	**x**	**y**	**z**	**Wyc**
La(1)	0.0000	0.2956	0.2500	4c
La(2)	0.0000	0.4466	0.7500	4c
Mn(1)	0.5000	0.3433	0.7500	4c
Mn(2)	0.5000	0.4422	0.2500	4c
O(1)	0.5000	0.2895	0.9868	8f
O(3)	0.5000	0.3958	0.9971	8f
O(5)	0.5000	0.5000	0.5000	4a
O(6)	0.0000	0.3471	0.7500	4c
O(7)	0.0000	0.4533	0.2500	4c

Table A.1: Computed equilibrium structure of the paraelectric *Cmcm* phase of $La_2Mn_2O_7$.

Cmc2₁		a = 3.9031Å b = 25.1709Å c = 5.3335Å $\alpha = \beta = \gamma = 90°$		
Atoms	**x**	**y**	**z**	**Wyc**
La(1)	0.0000	0.2966	0.2139	4a
La(2)	0.0000	0.4468	0.7188	4a
Mn(1)	0.5000	0.3425	0.7483	4a
Mn(2)	0.5000	0.4422	0.2234	4a
O(1)	0.5000	0.2834	0.9602	4a
O(2)	0.5000	0.2970	0.4854	4a
O(3)	0.5000	0.3893	0.0108	4a
O(4)	0.5000	0.4045	0.5216	4a
O(5)	0.5000	0.4929	0.9372	4a
O(6)	0.0000	0.3465	0.7537	4a
O(7)	0.0000	0.4510	0.2310	4a

Table A.2: Computed equilibrium structure of the ferroelectric *Cmc2₁* phase of $La_2Mn_2O_7$.

APPENDIX B

Brillouin Zone

B1 Brillouin Zone of space group $Cmcm$ (63)

B2 Brillouin Zone of space group $Cmc2_1$ (36)

B3 Brillouin Zone of space group $C2/m$ (12)

B4 The k-vector types of space group $C2/m$ (12)

B5 Brillouin Zone of space group $Ia\bar{3}$ (206)

B6 The k-vector types of space group $Ia\bar{3}$ (206)

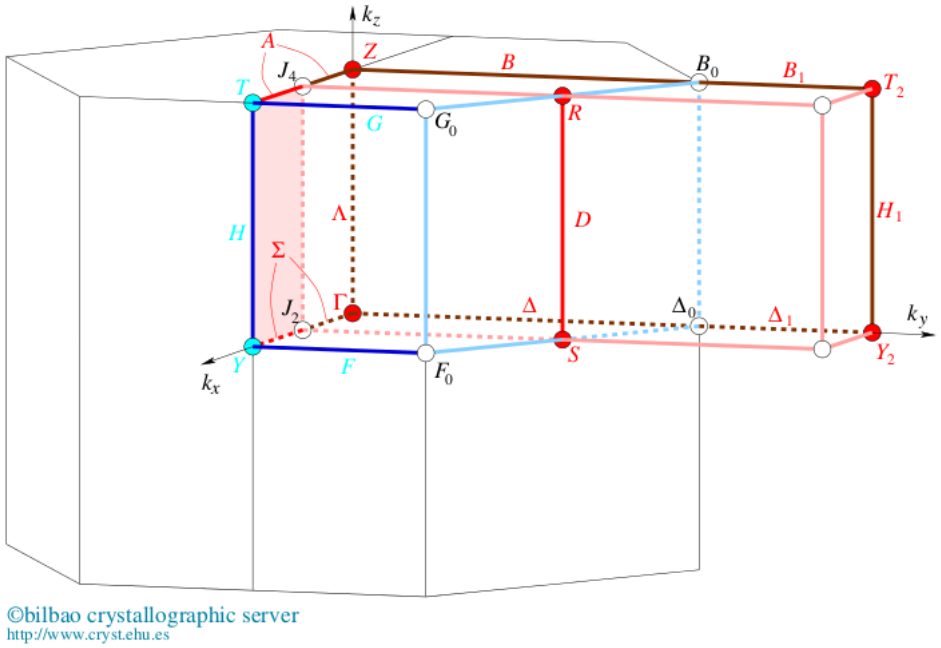

Figure B.1: Brillouin Zone of space group *Cmcm* (63)

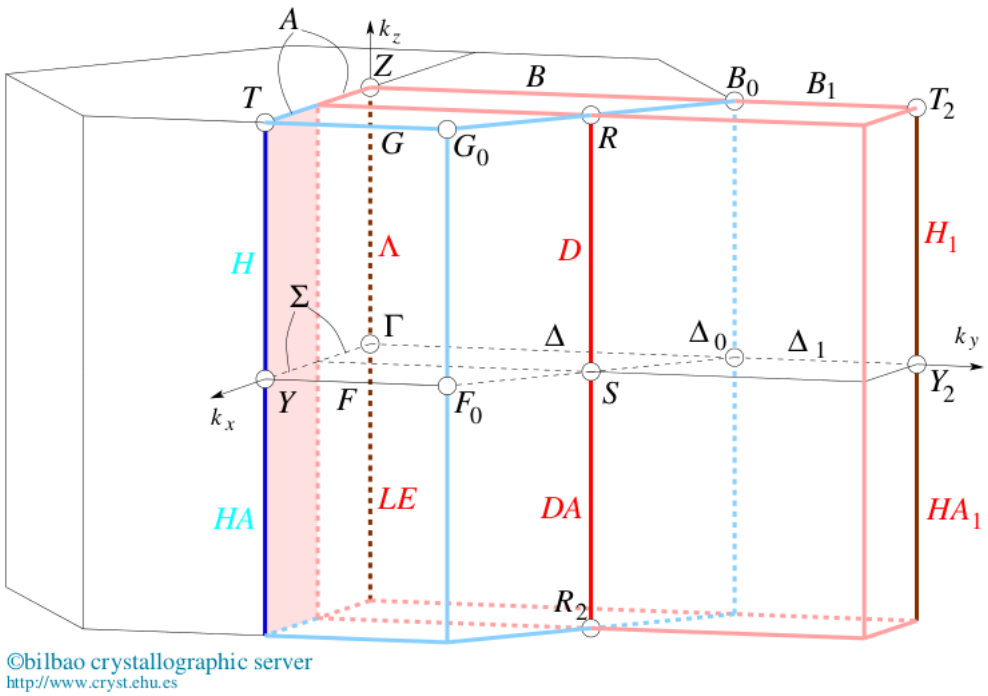

Figure B.2: Brillouin Zone of space group $Cmc2_1$ (36)

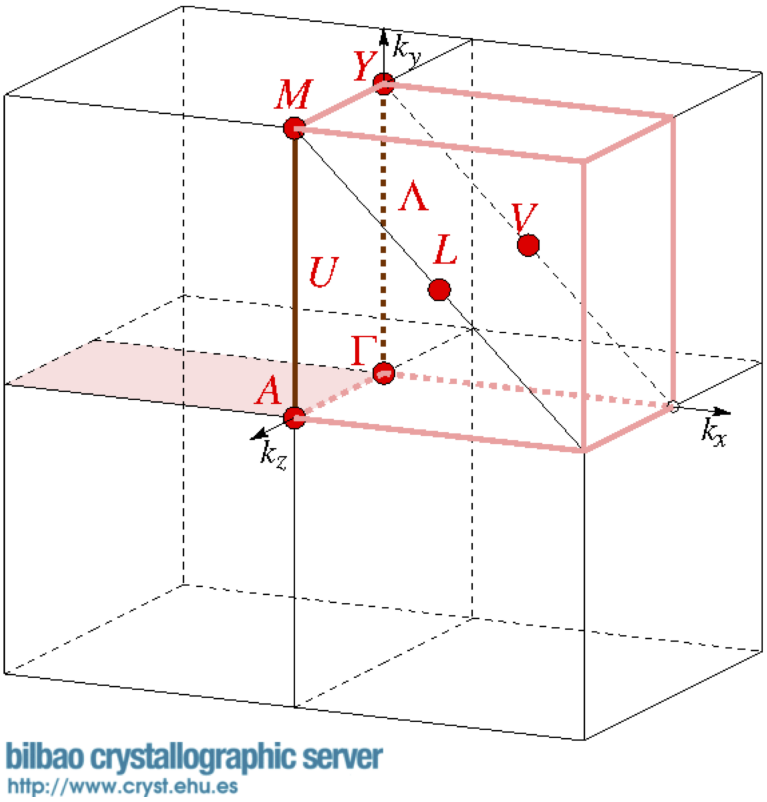

Figure B.3: Brillouin Zone of space group $C2/m$ (12)

k-vector description			ITA description			
Label	Primitive basis	Conventional basis	Wyckoff Position			Coordinates
GM	0,0,0	0,0,0	2	a	2/m	0,0,0
Y	1/2,1/2,0	0,1,0	2	b	2/m	0,1/2,0
A	0,0,1/2	0,0,1/2	2	c	2/m	0,0,1/2
M	1/2,1/2,1/2	0,1,1/2	2	d	2/m	0,1/2,1/2
V	1/2,0,0	1/2,1/2,0	4	e	-1	1/4,1/4,0
L	1/2,0,1/2	1/2,1/2,1/2	4	f	-1	1/4,1/4,1/2
LD	u,u,0	0,2u,0	4	g	2	0,y,0 : 0 < y < 1/2
U	u,u,1/2	0,2u,1/2	4	h	2	0,y,1/2 : 0 < y < 1/2
B	v,-v,u	2v,0,u	4	i	m	x,0,z : 0 < z < 1/2; -1/2 < x <= 1/2 U U x,0,0 : 0 < x < 1/2 U U x,0,1/2 : 0 < x < 1/2
GP	u,v,w	u-v,u+v,w	8	j	1	x,y,z : 0 < z < 1/2; 0 <= x <= 1/2; 0 < y < 1/2 U U x,y,0 : 0 < x < 1/4; 0 < y < 1/2 U U 1/4,y,0 : 0 < y < 1/4 U U x,y,1/2 : 0 < x < 1/4; 0 < y < 1/2 U U 1/4,y,1/2 : 0 < y < 1/4

Figure B.4: The k-vector types of space group $C2/m$ (12) [unique axis b]

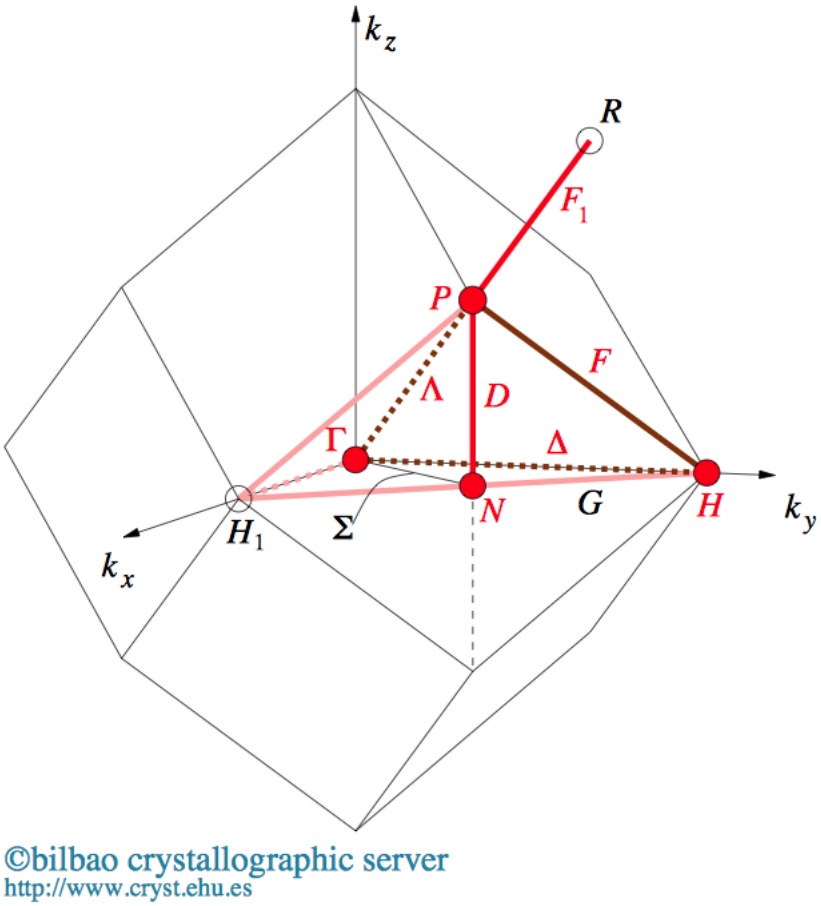

Figure B.5: Brillouin Zone of space group $Ia\bar{3}$ (206)

k-vector description			ITA description			
CDML[1]		Conventional basis	Wyckoff Position			Coordinates
Label	Primitive basis					
GM	0,0,0	0,0,0	4	a	m-3.	0,0,0
H	1/2,-1/2,1/2	0,1,0	4	b	m-3.	0,1/2,0
H~R			4	b	m-3.	1/2,1/2,1/2
P	1/4,1/4,1/4	1/2,1/2,1/2	8	c	23.	1/4,1/4,1/4
N	0,0,1/2	1/2,1/2,0	24	d	2/m..	1/4,1/4,0
DT	u,-u,u	0,2u,0	24	e	mm2..	0,y,0 : 0 < y < 1/2
LD	u,u,u ex	2u,2u,2u	32	f	.3.	x,x,x : 0 < x < 1/4
F	1/2-u,-1/2+3u,1/2-u ex	2u,1-2u,2u	32	f	.3.	x,1/2-x,x : 0 < x < 1/4
F~F_1=[PR]			32	f	.3.	x,x,x : 1/4 < x < 1/2
LD+F_1~[GMR] \ [P]			32	f	.3.	x,x,x : 0 < x < 1/2, x!=1/4
D	u,u,1/2-u	1/2,1/2,2u	48	g	2..	1/4,1/4,z : 0 < z < 1/4
SM	0,0,u ex	u,u,0	48	h	m..	x,x,0 : 0 < x < 1/4
G	1/2-u,-1/2+u,1/2 ex	u,1-u,0	48	h	m..	x,1/2-x,0 : 0 < x < 1/4
A	u,-u,v ex	v-u,v+u,0	48	h	m..	x,y,0 : 0 < x < y < 1/2-x
AA	-u,u,v ex	u+v,-u+v,0	48	h	m..	x,y,0 : 0 < y < x < 1/2-y
SM+G+A+AA			48	h	m..	x,y,0 : 0 < y < 1/2-x < 1/2 U U x,1/2-x,0 : 0 < x < 1/4
GP	u,v,w	w+v,w+u,v+u	96	i	1	x,y,z : 0 < z <= x < y < 1/2-x U U x,y,z : 0 < z < y < x <= 1/2-y U U x,x,z : 0 < z < x < 1/4

Figure B.6: The k-vector types of space group $Ia\bar{3}$ (206)

APPENDIX C

Cr_2O_3

Magnetic space group	Rhombohedral $R\bar{3}c$ num. 161
Unit cell	10 atoms
Cell parameters	a=5.37Å
	α=54.66°
Cr positions	x, x, x with x=0.1536
O positions	0.9424, 0.5575, 0.25
Gap	$\sim$ 2.1 eV
Magnetic moment Cr	$\sim$ 2.8 μ_B
IR modes (cm^{-1})	A_{2u}=408, 596
	E_u=316, 455, 578, 653

Table C.1: Cr_2O_3: Technical parameters.

APPENDIX D

Types of heterostructures

The potential profile near the heterojunction has step-discontinuities. Tree types of heterojunction are identified, according to the alignment of the bands producing the discontinuity. Figure D.1 shows a sketch of this band alignements.

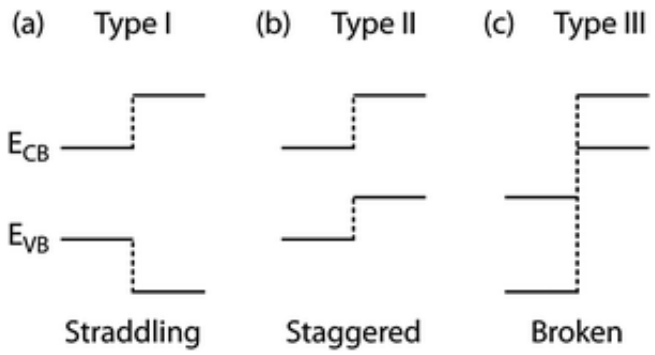

Figure D.1: Various heterostructure band alignments. Conduction-band-edge and valence-band-edge position for each alignements have been labeled E_{cb} and E_{vb}, respectively.
Source: `http://pubs.rsc.org/en/content/articlehtml/2013/cs/c2cs35374a`.

- **Type I (or A)** -*straddling*, the band gap of one material entirely overlaps that of the other and the potential discontinuities for the conduction band, E_{cb}, and for the valence band, E_{vb}. Both the hole and electron accumulate in one of the two components. This does not promote the flow of charge carriers instead, this band alignment promotes recombination.
- **Type II (or B)** -*staggered*, both the conduction-band edge and the valence-band edge of one material being lower than the corresponding band edges

of the other material, electrons are confined in one material, while holes are confined in the other material.

- **Type III** -*broken* or *misaligned*, electrons and holes are confined separately in the two materials. But, as the valence band of the material, in which the holes are confined, overlaps the conduction band of the other material.

APPENDIX E

Piezoelectric tensor

Bilbao Crystallographic Server → TENSOR - Symmetry-adapted tensors

Symmetry-adapted form of the Isothermal piezoelectric tensor e_{ijk} (direct effect) for the space group *Pna2₁*

Information about the selected tensor

- 3 rd rank Isothermal piezoelectric tensor e_{ijk} (direct effect)
- Polar tensor invariant under time-reversal symmetry operation
- Defining equation: $\mathbf{D_i = e_{ijk} \varepsilon_{jk}}$
- Relates Strain tensor ε_{ij} with Electric displacement field **D**
- Intrinsic symmetry symbol: $\mathbf{V[V^2]}$
- Symmetrized indexes due to intrinsic symmetry:
  - $e_{ijk} = e_{ikj}$
- Abbreviated notation: $e_{ijk} \rightarrow e_{ij}$
  - jk → j if j=k, jk → 9-(j+k) if j≠k

Table of tensor components

e_{ij}		j					
		1	*2*	*3*	*4*	*5*	*6*
i	*1*	0	0	0	0	$\mathbf{e_{15}}$	0
	2	0	0	0	$\mathbf{e_{24}}$	0	0
	3	$\mathbf{e_{31}}$	$\mathbf{e_{32}}$	$\mathbf{e_{33}}$	0	0	0

Number of independent coefficients: 5

Note: semitransparent tensor components are identical or opposite to bold symbols due to the intrinsic symmetry of the tensor

Bibliography

[1] Marco Scarrozza, Maria Barbara Maccioni, Giorgia M. Lopez, and Vincenzo Fiorentini. Topological multiferroics. *Phase Transitions*, 88(10):953–961, 2015.

[2] Maria Barbara Maccioni, Francesco Ricci, and Vincenzo Fiorentini. Structure and gap of low- x $(Ga_{1-x}In_x)_2O_3$ alloys. *Journal of Physics: Conference Series*, 566(1):012016, 2014.

[3] Maria Barbara Maccioni, Francesco Ricci, and Vincenzo Fiorentini. Low In solubility and band offsets in the small- x β-Ga_2O_3/$(Ga_{1-x}In_x)_2O_3$ system. *Applied Physics Express*, 8(2):021102, 2015.

[4] Maria Barbara Maccioni, Francesco Ricci, and Vincenzo Fiorentini. Properties of $(Ga_{1-x}In_x)_2O_3$ over the whole x range. *ArXiv e-prints*, nov 2015.

[5] G. Kresse and J. Furthmüller. Efficient iterative schemes for *ab initio* total-energy calculations using a plane-wave basis set. *Phys. Rev. B*, 54:11169–11186, Oct 1996.

[6] P. Hohenberg and W. Kohn. Inhomogeneous electron gas. *Phys. Rev.*, 136:B864–B871, Nov 1964.

[7] W. Kohn and L. J. Sham. Self-Consistent Equations Including Exchange and Correlation Effects. *Phys. Rev.*, 140:A1133–A1138, Nov 1965.

[8] L. H. Thomas. The calculation of atomic fields. *Mathematical Proceedings of the Cambridge Philosophical Society*, 23:542–548, 1 1927.

[9] E. Fermi. Un Metodo Statistico per la Determinazione di alcune Prioprietà dell'Atomo. *Rend. Accad. Naz. Lincei*, 6:602–607, 1927.

[10] M. Born and R. Oppenheimer. Zur Quantentheorie der Molekeln. *Annalen der Physik*, 389(20):457–484, 1927.

[11] D. M. Ceperley and B. J. Alder. Ground state of the electron gas by a stochastic method. *Phys. Rev. Lett.*, 45:566–569, Aug 1980.

[12] John P. Perdew and Yue Wang. Accurate and simple analytic representation of the electron-gas correlation energy. *Phys. Rev. B*, 45:13244–13249, Jun 1992.

[13] John P. Perdew, Kieron Burke, and Matthias Ernzerhof. Generalized Gradient Approximation Made Simple. *Phys. Rev. Lett.*, 77:3865–3868, Oct 1996.

[14] Hendrik J. Monkhorst and James D. Pack. Special points for brillouin-zone integrations. *Phys. Rev. B*, 13:5188–5192, Jun 1976.

[15] N. David Mermin. Thermal properties of the inhomogeneous electron gas. *Phys. Rev.*, 137:A1441–A1443, Mar 1965.

[16] A. De Vita. PhD thesis, Keele University, 1992.

[17] Peter E. Blöchl, O. Jepsen, and O. K. Andersen. Improved tetrahedron method for brillouin-zone integrations. *Phys. Rev. B*, 49:16223–16233, Jun 1994.

[18] M. Methfessel and A. T. Paxton. High-precision sampling for Brillouin-zone integration in metals. *Phys. Rev. B*, 40:3616–3621, Aug 1989.

[19] James C. Phillips and Leonard Kleinman. New Method for Calculating Wave Functions in Crystals and Molecules. *Phys. Rev.*, 116:287–294, Oct 1959.

[20] Morrel H. Cohen and V. Heine. Cancellation of kinetic and potential energy in atoms, molecules, and solids. *Phys. Rev.*, 122:1821–1826, Jun 1961.

[21] Conyers Herring. A new method for calculating wave functions in crystals. *Phys. Rev.*, 57:1169–1177, Jun 1940.

[22] M. C. Payne, M. P. Teter, D. C. Allan, T. A. Arias, and J. D. Joannopoulos. Iterative minimization techniques for *ab initio* total-energy calculations: molecular dynamics and conjugate gradients. *Rev. Mod. Phys.*, 64:1045–1097, Oct 1992.

[23] P. E. Blöchl. Projector augmented-wave method. *Phys. Rev. B*, 50:17953–17979, Dec 1994.

[24] Jürgen Hafner. Ab-initio simulations of materials using VASP: Density-functional theory and beyond. *Journal of Computational Chemistry*, 29(13):2044–2078, 2008.

[25] U von Barth and L Hedin. A local exchange-correlation potential for the spin polarized case. i. *Journal of Physics C: Solid State Physics*, 5(13):1629, 1972.

[26] J. Kübler, K. H. Höck, J. Sticht, and A. R. Williams. Local spin density functional theory of noncollinear magnetism (invited). *Journal of Applied Physics*, 63(8):3482–3486, 1988.

[27] E. G. Moroni, G. Kresse, J. Hafner, and J. Furthmüller. Ultrasoft pseudopotentials applied to magnetic fe, co, and ni: From atoms to solids. *Phys. Rev. B*, 56:15629–15646, Dec 1997.

[28] B. Ujfalussy, Xindong Wang, Xiaoguang Zhang, D. M. C. Nicholson, W. A. Shelton, G. M. Stocks, A. Canning, Yang Wang, B. L. Gyorffy, and H. H. Wills. High Performance First Principles Method for Complex Magnetic Properties.

[29] D. Hobbs, G. Kresse, and J. Hafner. Fully unconstrained noncollinear magnetism within the projector augmented-wave method. *Phys. Rev. B*, 62:11556–11570, Nov 2000.

[30] G. Pastori-Parravicini G. Grosso. *Solid State Physics*. Accademic Press, 2003.

[31] R. D. King-Smith and David Vanderbilt. Theory of polarization of crystalline solids. *Phys. Rev. B*, 47:1651–1654, Jan 1993.

[32] David Vanderbilt and R. D. King-Smith. Electric polarization as a bulk quantity and its relation to surface charge. *Phys. Rev. B*, 48:4442–4455, Aug 1993.

[33] Raffaele Resta. Theory of the electric polarization in crystals. *Ferroelectrics*, 136(1):51–55, 1992.

[34] Raffaele Resta. Macroscopic polarization in crystalline dielectrics: the geometric phase approach. *Rev. Mod. Phys.*, 66:899–915, Jul 1994.

[35] Raffaele Resta. Berry phase in electronic wavefunctions. *Troisième cycle de la physique en Suisse romande.*, 1996.

[36] Silvia Picozzi and Claude Ederer. First principles studies of multiferroic materials. *Journal of Physics: Condensed Matter*, 21(30):303201, 2009.

[37] J. B. Neaton, C. Ederer, U. V. Waghmare, N. A. Spaldin, and K. M. Rabe. First-principles study of spontaneous polarization in multiferroic $BiFeo_3$. *Phys. Rev. B*, 71:014113, Jan 2005.

[38] W. Eerenstein, N. D. Mathur, and J. F. Scott. Multiferroic and magnetoelectric materials. *Nature*, 442(7104):759–765, 08 2006.

[39] NA Hill. Why are there so few magnetic ferroelectrics? *Journal of Physical Chemistry B*, 104(29):6694–6709, JUL 27 2000.

[40] H. A. Jahn and E. Teller. Stability of Polyatomic Molecules in Degenerate Electronic States. I. Orbital Degeneracy. *Proceedings of the Royal Society of London A: Mathematical, Physical and Engineering Sciences*, 161(905):220–235, 1937.

[41] Ralph G. Pearson. Concerning Jahn-Teller Effects. *Proceedings of the National Academy of Sciences*, 72(6):2104–2106, 1975.

[42] Nicole A. Benedek and Craig J. Fennie. Hybrid improper ferroelectricity: A mechanism for controllable polarization-magnetization coupling. *Phys. Rev. Lett.*, 106:107204, Mar 2011.

[43] Jorge López-Pérez and Jorge Íñiguez. *Ab initio* study of proper topological ferroelectricity in layered perovskite $La_2Ti_2O_7$. *Phys. Rev. B*, 84:075121, Aug 2011.

[44] F. Lichtenberg, A. Herrnberger, K. Wiedenmann, and J. Mannhart. Synthesis of perovskite-related layered $A_nB_nO_{3n+2}$ = ABOX type niobates and titanates and study of their structural, electric and magnetic properties. *Progress in Solid State Chemistry*, 29(1–2):1 – 70, 2001.

[45] H. Kohlstedt, Y. Mustafa, A. Gerber, A. Petraru, M. Fitsilis, R. Meyer, U. Böttger, and R Waser. Current status and challenges of ferroelectric memory devices. *Microelectronic Engineering*, 80:296 – 304, 2005. 14th biennial Conference on Insulating Films on SemiconductorsINFOS2005.

[46] G. Kresse and D. Joubert. From ultrasoft pseudopotentials to the projector augmented-wave method. *Phys. Rev. B*, 59:1758–1775, Jan 1999.

[47] Timm Carsten. *Theory of Magnetism.* International Max Plank Research Shool for Dinamics Process in Atoms, Molecules and Solids., 2010. Winter Semester lecture.

[48] John B. Goodenough. Theory of the Role of Covalence in the Perovskite-Type Manganites [La, M(II)]MnO_3. *Phys. Rev.*, 100:564–573, Oct 1955.

[49] Junjiro Kanamori. Superexchange interaction and symmetry properties of electron orbitals. *Journal of Physics and Chemistry of Solids*, 10(2):87 – 98, 1959.

[50] Stephen Blundell. *Magnetism in Condensed Matter.* Oxford Master Series in Physics, Oct 2001.

[51] T. Mizokawa and A. Fujimori. Electronic structure and orbital ordering in perovskite-type 3d transition-metal oxides studied by Hartree-Fock band-structure calculations. *Phys. Rev. B*, 54:5368–5380, Aug 1996.

[52] M. A. Yurishchev. Anisotropic simple-cubic ising lattice: extended phenomenological renormalization-group treatment. *eprint arXiv:cond-mat/0312555*, dec 2003.

[53] Curie P. Sur la symétrie dans les phénomènes physiques. symétrie d'un champ électrique d'un champ magnétique. *J Phys.*, 3:393–416, 1894.

[54] D. N. Astrov. Magnetoelectric effect in chromium oxide. *Zh. Exp. Teor. Fiz.*, 38:984, 1960. Soviet Physics - J. Exptl. Theoret. Phys. volume 13 (4), 729-733 (1961).

[55] E.M. Lifshitz L.D. Landau. *Electrodynamics of Continuous Media, of Course of Theoretical Physics*, volume 8. Pergamon Oxford, 2nd edition, 1984. transl. from the Russian.

[56] I.E. Dzyaloshinskii. K voprosu o magnitno-elektricheskom effekte v antiferromagnetikakh. *Zh. Exp. Teor. Fiz.*, 37(3):881–882, 1959. I.E. Dzyaloshinskii, On the magneto-electrical effect in antiferromagnets, Sov. Phys. JETP 10(3), 628-629 (1960).

[57] Helmut Kronmuller and Stuart Parkin, editors. *Handbook of Magnetism and Advanced Magnetic Materials*. John Wiley & Sons, 2007.

[58] James F. Scott. *Ferroelectric Memories*, volume 3 of *Springer Series in Advanced Microelectronics Series*. Springer-Verlag Berlin Heidelberg, 2000.

[59] Karin M. Rabe, Charles H. Ahn, and Jean-Marc Triscone, editors. *Physics of Ferroelectrics. A Modern Perspective*. Topics in Applied Physics Series. Springer-Verlag Berlin Heidelberg, 2007.

[60] R. Ramesh and Nicola A. Spaldin. Multiferroics: progress and prospects in thin films. *Nat Mater*, 6(1):21–29, 01 2007.

[61] Jorge Íñiguez. First-Principles Approach to Lattice-Mediated Magnetoelectric Effects. *Phys. Rev. Lett.*, 101:117201, Sep 2008.

[62] J. P. Rivera. On definitions, units, measurements, tensor forms of the linear magnetoelectric effect and on a new dynamic method applied to Cr-Cl boracite. *Ferroelectrics*, 161(1):165–180, 1994.

[63] A.S. Borovik-Romanov and H. Grimmer. Magnetic properties. In A. Authier, editor, *International Tables for Crystallography Volume D: Physical properties of crystals*, volume D of *International Tables for Crystallography*, pages 105–149. Springer Netherlands, 2003.

[64] I. Dzyaloshinsky. A thermodynamic theory of "weak" ferromagnetism of antiferromagnetics. *Journal of Physics and Chemistry of Solids*, 4(4):241 – 255, 1958.

[65] Tôru Moriya. Theory of Magnetism of NiF_2. *Phys. Rev.*, 117:635–647, Feb 1960.

[66] Luigi Paolasini. Lectures on Magnetism. Lecture 4: Magnetic interactions.

[67] Peter Weinberger. *Exchange & Dzyaloshinskii-Moriya interactions*, chapter 7, pages 65–75. Condensed Matter Physics Series. Chapman and Hall/CRC Taylor & Francis Group, 2008.

[68] Hosho Katsura, Naoto Nagaosa, and Alexander V. Balatsky. Spin Current and Magnetoelectric Effect in Noncollinear Magnets. *Phys. Rev. Lett.*, 95:057205, 2005.

[69] Yoshihiro Kokubun, Kasumi Miura, Fumie Endo, and Shinji Nakagomi. Sol-gel prepared β-Ga_2O_3 thin films for ultraviolet photodetectors. *Applied Physics Letters*, 90(3), 2007.

[70] Takayoshi Oshima, Takeya Okuno, Naoki Arai, Norihito Suzuki, Shigeo Ohira, and Shizuo Fujita. Vertical Solar-Blind Deep-Ultraviolet Schottky Photodetectors Based on β-Ga_2O_3 Substrates. *Applied Physics Express*, 1(1):011202, 2008.

[71] Kiyoshi Shimamura, Encarnación G. Víllora, Kay Domen, Keiichi Yui, Kazuo Aoki, and Noboru Ichinose. Epitaxial Growth of GaN on (100) β-Ga_2O_3 Substrates by Metalorganic Vapor Phase Epitaxy. *Japanese Journal of Applied Physics*, 44(1L):7, 2005.

[72] Masataka Higashiwaki, Kohei Sasaki, Akito Kuramata, Takekazu Masui, and Shigenobu Yamakoshi. Gallium oxide (Ga_2O_3) metal-semiconductor field-effect transistors on single-crystal β -Ga_2O_3 (010) substrates. *Applied Physics Letters*, 100(1):–, 2012.

[73] Pai-Chun Chang, Zhiyong Fan, Wei-Yu Tseng, A. Rajagopal, and Jia G. Lu. β-Ga_2O_3 nanowires: Synthesis, characterization, and p-channel field-effect transistor. *Applied Physics Letters*, 87(22), 2005.

[74] Paola Alippi, Maura Cesaria, and Vincenzo Fiorentini. Impurity-vacancy complexes and ferromagnetism in doped sesquioxides. *Phys. Rev. B*, 89:134423, Apr 2014.

[75] D.D. Edwards, P.E. Folkins, and T.O. Mason. Phase equilibria in the Ga_2O_3-In_2O_3 system. *Journal of the American Ceramic Society*, 80(1):253–257, 1997.

[76] V. M. Goldschmidt, T . Barth, and G. Lunde. Geochemische Verteilungsgesetze der Elemente V Isomorphie und polymorphie der sesquioxide. *Skrifter Norske Videnskaps-Akad.*, No.5(Mat. Naturv. Klasse):1–59, 1925.

[77] R.D. Shannon and C.T. Prewitt. Synthesis and structure of phases in the In_2O_3-Ga_2O_3 system . *Journal of Inorganic and Nuclear Chemistry*, 30(6):1389 – 1398, 1968.

[78] Waring J. Schneider S., Roth R. Solid state reactions involving oxides of trivalent cations. *J. Res. Natl. Bur. Stand.*, 65A:345–374, 1961.

[79] J. Macdonald, J.A. Gard, and F.P. Glasser. Preparation and crystal chemistry of some mixed metal sesquioxides containing Fe, Al, Ga, Cr, Sc and In. *Journal of Inorganic and Nuclear Chemistry*, 29(3):661 – 671, 1967.

[80] Rustum Roy, V. G. Hill, and E. F. Osborn. Polymorphism of Ga_2O_3 and the System Ga_2O_3—H_2O. *Journal of the American Chemical Society*, 74(3):719–722, 1952.

[81] David F. Edwards. Beta-Gallium Oxide (β-Ga_2O_3). In Edward D. Palik, editor, *Handbook of Optical Constants of Solids*, pages 753 – 760. Academic Press, Burlington, 1997.

[82] S. Geller. Crystal Structure of β-Ga_2O_3. *The Journal of Chemical Physics*, 33(3):676–684, 1960.

[83] V Fiorentini and A Baldereschi. Semiempirical self-energy corrections to LDA bands of semiconductors, and a scaling law for the scissor operator. *Journal of Physics: Condensed Matter*, 4(27):5967, 1992.

[84] Fabi Zhang, Katsuhiko Saito, Tooru Tanaka, Mitsuhiro Nishio, and Qixin Guo. Wide bandgap engineering of $(GaIn)_2O_3$ films. *Solid State Communications*, 186:28 – 31, 2014.

[85] F Ricci, F Boschi, A Baraldi, A Filippetti, M Higashiwaki, A Kuramata, V Fiorentini, and R Fornari. Theoretical and experimental investigation of optical absorption anisotropy in β-Ga_2O_3. 2015.

[86] Jochen Heyd, Gustavo E. Scuseria, and Matthias Ernzerhof. Erratum:Hybrid functionals based on a screened Coulomb potential,[J. Chem. Phys.118, 8207 (2003)]. *The Journal of Chemical Physics*, 124(21), 2006.

[87] A. Filippetti, C. D. Pemmaraju, S. Sanvito, P. Delugas, D. Puggioni, and Vincenzo Fiorentini. Variational pseudo-self-interaction-corrected density functional approach to the *ab initio* description of correlated solids and molecules. *Phys. Rev. B*, 84:195127, Nov 2011.

[88] Filippetti, A. and Fiorentini, V. A practical first-principles band-theory approach to the study of correlated materials. *Eur. Phys. J. B*, 71(2):139–183, 2009.

[89] C. W. Tang and S. A. VanSlyke. Organic electroluminescent diodes. *Applied Physics Letters*, 51(12):913–915, 1987.

[90] I. Hamberg and C. G. Granqvist. Evaporated Sn doped In_2O_3 films. Basic optical properties and applications to energy efficient windows. *Journal of Applied Physics*, 60(11):R123–R160, 1986.

[91] C.G. Granqvist and A. Hultåker. Transparent and conducting ITO films: new developments and applications. *Thin Solid Films*, 411(1):1 – 5, 2002. Proceedings of the 2nd International Symposium on Transparent Oxide Thin Films for Electronics and Optics.

[92] H. Kim, A. Piqué, J. S. Horwitz, H. Mattoussi, H. Murata, Z. H. Kafafi, and D. B. Chrisey. Indium tin oxide thin films for organic light-emitting devices. *Applied Physics Letters*, 74(23):3444–3446, 1999.

[93] Paul Erhart, Andreas Klein, Russell G. Egdell, and Karsten Albe. Band structure of indium oxide: Indirect versus direct band gap. *Phys. Rev. B*, 75:153205, Apr 2007.

[94] Aron Walsh, Juarez L. F. Da Silva, Su-Huai Wei, C. Körber, A. Klein, L. F. J. Piper, Alex DeMasi, Kevin E. Smith, G. Panaccione, P. Torelli, D. J. Payne, A. Bourlange, and R. G. Egdell. Nature of the Band Gap of In_2O_3 Revealed by First-Principles Calculations and X-Ray Spectroscopy. *Phys. Rev. Lett.*, 100:167402, Apr 2008.

[95] F. Fuchs and F. Bechstedt. Indium-oxide polymorphs from first principles: Quasiparticle electronic states. *Phys. Rev. B*, 77:155107, Apr 2008.

[96] B. García-Domene, J. A. Sans, O. Gomis, F. J. Manjón, H. M. Ortiz, D. Errandonea, D. Santamaría-Pérez, D. Martínez-García, R. Vilaplana, A. L. J. Pereira, A. Morales-García, P. Rodríguez-Hernández, A. Muñoz, C. Popescu, and A. Segura. Pbca-Type In_2O_3: The High-Pressure Post-Corundum phase at Room Temperature. *The Journal of Physical Chemistry C*, 118(35):20545–20552, 2014.

[97] S. Zh. Karazhanov, P. Ravindran, P. Vajeeston, A. Ulyashin, T. G. Finstad, and H. Fjellvåg. Phase stability, electronic structure, and optical properties of indium oxide polytypes. *Phys. Rev. B*, 76:075129, Aug 2007.

[98] Joel B Varley and André Schleife. Bethe–Salpeter calculation of optical-absorption spectra of In_2O_3 and Ga_2O_3. *Semiconductor Science and Technology*, 30(2):024010, 2015.

[99] D. B. Laks, C. G. Van de Walle, G. F. Neumark, P. E. Blöchl, and S. T. Pantelides. Native defects and self-compensation in ZnSe. *Phys. Rev. B*, 45:10965–10978, May 1992.

[100] M. Baldini, D. Gogova, K. Irmscher, M. Schmidbauer, G. Wagner, and R. Fornari. Heteroepitaxy of $Ga_{2(1-x)}In_{2x}O_3$ layers by MOVPE with two different oxygen sources. *Crystal Research and Technology*, 49(8):552–557, 2014.

[101] Mike Finnis. *Interatomic Forces in Condensed Matter*. Oxford University Press, Oct 2003.

[102] Haiying He, Roberto Orlando, Miguel A. Blanco, Ravindra Pandey, Emilie Amzallag, Isabelle Baraille, and Michel Rérat. First-principles study of the structural, electronic, and optical properties of Ga_2O_3 in its monoclinic and hexagonal phases. *Phys. Rev. B*, 74:195123, Nov 2006.

[103] Vincenzo Fiorentini. Semiconductor band structures at zero pressure. *Phys. Rev. B*, 46:2086–2091, Jul 1992.

[104] Luca Marsella and Vincenzo Fiorentini. Structure and stability of rare-earth and transition-metal oxides. *Phys. Rev. B*, 69:172103, May 2004.

[105] Pietro Delugas, Vincenzo Fiorentini, and Alessio Filippetti. Publisher's Note: Dielectric and vibrational properties of bixbyite sesquioxides. *Phys. Rev. B*, 80:139903, Oct 2009.

[106] P. D. C. King, T. D. Veal, F. Fuchs, Ch. Y. Wang, D. J. Payne, A. Bourlange, H. Zhang, G. R. Bell, V. Cimalla, O. Ambacher, R. G. Egdell, F. Bechstedt, and C. F. McConville. Band gap, electronic structure, and surface electron accumulation of cubic and rhombohedral In_2O_3. *Phys. Rev. B*, 79:205211, May 2009.

[107] Hartwin Peelaers, Daniel Steiauf, Joel B. Varley, Anderson Janotti, and Chris G. Van de Walle. $(In_xGa_{1-x})_2O_3$ alloys for transparent electronics. *Phys. Rev. B*, 92:085206, Aug 2015.

[108] R. Schewski, T. Markurt, T. Schulz, T. Remmele, G. Wagner, M. Baldini, H. von Wenckstern, M. Grundmann, , and M. Albrecht. Miscibility and phase separation in the $(In_xGa_{1-x})_2O_3$ system.

[109] Oshima Yuichi, Víllora Encarnación G., Matsushita Yoshitaka, Yamamoto Satoshi, and Shimamura Kiyoshi. Epitaxial growth of phase-pure ε-Ga_2O_3 by halide vapor phase epitaxy. *Journal of Applied Physics*, 118(8), 2015.

[110] Simon M. Sze and Kwok K. Ng. *Physics of Semiconductor Devices*. John Wiley and Sons, 3rd edition edition, Nov 2006.

[111] M Peressi, N Binggeli, and A Baldereschi. Band engineering at interfaces: theory and numerical experiments. *Journal of Physics D: Applied Physics*, 31(11):1273, 1998.

[112] Chris G. Van de Walle and Richard M. Martin. Theoretical calculations of heterojunction discontinuities in the si/ge system. *Phys. Rev. B*, 34:5621–5634, Oct 1986.

[113] Ragesh Puthenkovilakam and Jane P. Chang. Valence band structure and band alignment at the ZrO_2/Si interface. *Applied Physics Letters*, 84(8), 2004.

[114] Helen Y. Playford, Alex C. Hannon, Emma R. Barney, and Richard I. Walton. Structures of uncharacterised polymorphs of gallium oxide from total neutron diffraction. *Chemistry – A European Journal*, 19(8):2803–2813, 2013.

[115] S Yoshioka, H Hayashi, A Kuwabara, F Oba, K Matsunaga, and I Tanaka. Structures and energetics of Ga_2O_3 polymorphs. *Journal of Physics: Condensed Matter*, 19(34):346211, 2007.

[116] E. Tronc, C. Chanéac, and J.P. Jolivet. Structural and Magnetic Characterization of ε-Fe_2O_3. *Journal of Solid State Chemistry*, 139(1):93 – 104, 1998.

[117] Capillas Cesar, Emre Sururi Tasci, Gemma de la Flor, Danel Orobengoa, Juan Manuel Perez-Mato, and Mois Ilia Aroyo. A new computer tool at the Bilbao Crystallographic Server to detect and characterize pseudosymmetry. *Zeitschrift für Kristallographie Crystalline Materials*, 226.2:186–196, 2011. doi:10.1524/zkri.2011.1321.

[118] K. Lefki and G. J. M. Dormans. Measurement of piezoelectric coefficients of ferroelectric thin films. *Journal of Applied Physics*, 76(3):1764–1767, 1994.

[119] Hang Guo, Daqun Bao, and Yi Zhang. Characterization of PZT ferroelectric thin films prepared by a modified sol-gel method. In *Ultrasonics Symposium, 2008. IUS 2008. IEEE*, pages 2130–2133, Nov 2008.

Acknowledgments

First and foremost, I would like to sincerely thank my supervisor, Prof. Vincenzo Fiorentini, for his unwavering support and encouragement during throughout this work and for giving me the opportunity to work on particularly interesting research topics. Then, I would like to thank Francesco Ricci because our collaboration has been a great opportunity to develop my skills.

Heartfelt thanks to Prof. Roberto Fornari for having refereed my thesis.

Special thanks to Francesco for his love and understanding, without his encouragement I would never have completed my Ph.D.

In the end, I am very grateful to my all colleagues for the moral supports and in particular to Laura since during the whole path we have always supported each other.

Maria Barbara Maccioni acknowledges the financial support of her PhD scholarship by Sardinia Regional Government under P.O.R. Sardegna F.S.E. Operational Programme of the Autonomous Region of Sardinia, European Social Fund 2007-2013 - Axis IV Human Resources, Objective l.3, Line of Activity l.3.1.